OAK RIDGE NATIONAL LABORATORY LIBRARIES
3 4456 0549113 4

CENTRAL RESEARCH LIBRARY
DOCUMENT COLLECTION
1

OAK R[illegible]ABORATORY

operated by

UNION CARBIDE CORPORATION
NUCLEAR DIVISION

for the

U.S. ATOMIC ENERGY COMMISSION

ORNL-TM-1500

Cy 1

DECLASSIFIED
CLASSIFICATION CHANGED TO:
BY AUTHORITY OF: AECM-2104 a2 BL 8/21/74
BL RU DD

FUELS AND MATERIALS DEVELOPMENT PROGRAM QUARTERLY PROGRESS REPORT FOR PERIOD ENDING MARCH 31, 1966

Compiled by

P. Patriarca

CENTRAL RESEARCH LIBRARY
DOCUMENT COLLECTION
LIBRARY LOAN COPY
DO NOT TRANSFER TO ANOTHER PERSON
If you wish someone else to see this document, send in name with document and the library will arrange a loan.

NOTICE This document contains information of a preliminary nature and was prepared primarily for internal use at the Oak Ridge National Laboratory. It is subject to revision or correction and therefore does not represent a final report.

[redacted]

LEGAL NOTICE

This report was prepared as an account of Government sponsored work. Neither the United States, nor the Commission, nor any person acting on behalf of the Commission:

A. Makes any warranty or representation, expressed or implied, with respect to the accuracy, completeness, or usefulness of the information contained in this report, or that the use of any information, apparatus, method, or process disclosed in this report may not infringe privately owned rights; or

B. Assumes any liabilities with respect to the use of, or for damages resulting from the use of any information, apparatus, method, or process disclosed in this report.

As used in the above, "person acting on behalf of the Commission" includes any employee or contractor of the Commission, or employee of such contractor, to the extent that such employee or contractor of the Commission, or employee of such contractor prepares, disseminates, or provides access to, any information pursuant to his employment or contract with the Commission, or his employment with such contractor.

[redacted]

ORNL-TM-1500

Contract No. W-7405-eng-26

FUELS AND MATERIALS DEVELOPMENT PROGRAM QUARTERLY PROGRESS REPORT FOR PERIOD ENDING MARCH 31, 1966

Compiled by

P. Patriarca

JUNE 1966

OAK RIDGE NATIONAL LABORATORY
Oak Ridge, Tennessee
operated by
UNION CARBIDE CORPORATION
for the
U.S. ATOMIC ENERGY COMMISSION

[redacted]

OAK RIDGE NATIONAL LABORATORY LIBRARIES

3 4456 0549113 4

[redacted]

FOREWORD

This is the eighth quarterly progress report describing work performed at the Oak Ridge National Laboratory for the Fuels and Materials Branch, Division of Reactor Development and Technology, U.S. Atomic Energy Commission. The specific programs covered are as follows:

Part I. Metals and Ceramics Division

Program Title	Person in Charge	Principal Investigator(s)
Controlled Precipitation in Nuclear Materials	W. O. Harms	J. L. Scott J. P. Hammond
Fuel Element Development	G. M. Adamson, Jr.	C. F. Leitten, Jr.
Nondestructive Test Development	D. A. Douglas, Jr.	R. W. McClung
Zirconium Metallurgy	C. J. McHargue	M. L. Picklesimer

Part II. Reactor Chemistry Division

Fission-Gas Release and Physical Properties of Fuel Materials During Irradiation	O. Sisman	R. M. Carroll M. F. Osborne

Part III. Solid State Division

Irradiation Effects on Alloys and Structural Materials	D. S. Billington	M. S. Wechsler

[redacted]

[redacted]

TABLE OF CONTENTS

Page

Summary ix

Part I. Metals and Ceramics Division

1. Controlled Precipitation in Nuclear Materials 3

Effect of Dispersed Precipitates on the Properties of Ceramic Materials 3

Precipitation Studies in Alumina and Magnesia 3

Dispersion Strengthening of Metals by Controlled Precipitation 4

Aluminum Alloys 4

Thorium Alloys 5

2. Fuel Element Development 9

Deposition of Uranium Dioxide by Hydroreduction of Uranium Hexafluoride 9

Deposition of Uranium Compounds by Lithium Vapor Reduction of Uranium Hexafluoride 11

Preparation of Uranium Dioxide by Hydroreduction of Uranium Chlorides 12

Deposition of Tungsten Alloys 14

Deposition of Molybdenum 18

Fabrication of Enriched UAl_3 Dispersion Fuel Plates . . 18

3. Nondestructive Test Development 23

Electromagnetic Test Methods 23

Phase-Sensitive Eddy-Current Instrument 23

Beat-Frequency Eddy-Current Instrument 24

Ultrasonic Test Methods 24

Tubing Inspection 24

4. Zirconium Metallurgy 26

Anisotropy in Zircaloy-2 and Zircaloy-4 26

Zircaloy Tubing 26

Determination of Yield Surfaces 28

[redacted]

[redacted]

Correction of Knoop Microhardness Measurements for Anisotropic Recovery 36

Yield and Flow in Uniaxial Tension and Compression . . 38

Studies of Zirconium Alloys in Shear 43

Basal Pole Figures by Quantitative Polarized Light Microscopy 48

Oxide Film Studies 50

Preparation of Single Crystals of Zirconium and Its Alloys 53

Properties of High-Purity Zirconium 55

Oxidation 55

Part II. Reactor Chemistry

5. Fission-Gas Release and Physical Properties of Fuel Materials During Irradiation 61

Uranium Dioxide Single-Crystal Specimens, C1-13, C1-18 . . 62

Uranium Dioxide Single-Crystal Specimen C1-19 64

Methods of Thermal Conductivity Measurements 65

Data Processing 67

Part III. Solid State Division

6. Irradiation Effects on Alloys and Structural Materials . . . 71

Radiation Effects on Pressure-Vessel Steels 72

Impact Tests on Irradiated Heat-Affected-Zone Samples of ASTM A-212B Pressure-Vessel Steel 72

The Annealing of Radiation Hardening in Tensile Samples of ASTM A-212B Pressure-Vessel Steel 76

Tensile Tests on Irradiated Iron 78

Dislocation Dynamics in Irradiated Iron 96

The Preparation and Purification of Single Crystals of Niobium 105

High Vacuum Electron Beam Floating Zone Refiner 105

Purification of Niobium by Electron Beam Floating Zone Refining 108

[redacted]

[redacted]

Examination of the Perfection of Niobium Single Crystals Using Borrmann Topography 121

Dislocation Etch Pits in Niobium 126

Slip Line Observations on Irradiated Niobium Single Crystals 133

Dislocation Dynamics in Niobium Single Crystals by Stress Relaxation Techniques 139

Thermal-Neutron Irradiation of Hastelloy-N Tensile Samples 144

[redacted]

[redacted]

[redacted]

[redacted]

SUMMARY

1. Controlled Precipitation in Nuclear Materials

The study of controlled precipitation in titanium-doped Al_2O_3 to improve work-to-fracture of this ceramic continued. Efforts were made to determine the character of the precipitate in situ by x-ray diffraction method. Because these efforts were unfruitful, analyses were conducted on a similar system, zirconium-doped MgO, to obtain useful insights upon the precipitation process in general. Examinations of as-received, impure crystals revealed two secondary x-ray spectra, one corresponding to magnesium-stabilized, cubic ZrO_2, the other to calcium-stabilized, cubic ZrO_2. Both showed a [100] ‖ [100] crystallographic orientation relationship with the matrix. After annealing at 2000°C and quenching, the former precipitate appeared to have dissolved while the latter remained. Since x-ray lines failed to appear for needles of a precipitate believed to be $CaZrO_3$ on the basis of metallographic observations, it was concluded that this precipitate may not have a unique orientation relationship with the matrix.

Controlled precipitation to improve elevated-temperature mechanical properties in aluminum using the SLIS method are being studied. The eutectic composition for the aluminum-rich, aluminum-cerium alloy was determined to be 11 wt % Ce; anodes were prepared in the eutectic alloy for converting material to SLIS powder by a process which combines spinning-consumable-anode atomization with "splat-cooling." An ultrafine, stable dispersion of ZrB_2 in thorium was prepared by internally boronating solid-solution, Th–4.65 wt % Zr alloy powders. Compacts extruded at 750°C gave hot hardnesses in the temperature range of 600 to 800°C that were more than two times higher than for thorium alloys or dispersions tested heretofore.

2. Fuel Element Development

In this period, fabrication of UO_2 by direct conversion of UF_6 has progressed into the fabrication of irradiation specimens for both solid and powder products. Work on conversion of UCl_4-UCl_5 was terminated

[redacted]

due to redirection of the program, and a report describing the process is being prepared. Following the successful conversion of UF_6 to uranium metal powder by the lithium vapor reduction process, we have modified the apparatus to determine the feasibility of producing uranium nitride powder.

Additional experiments in the thermochemical deposition of tungsten-rhenium alloys indicate that homogeneous deposits are obtained by introducing the gasses into the deposition zone by use of an injector system. Scaleup of the process is under way.

Experiments in the fabrication behavior of UAl_3 in an aluminum matrix for high-performance research reactor fuel elements have been reactivated in an attempt to overcome a swelling problem. Currently, no explanation for the phenomenon is apparent.

3. Nondestructive Test Development

We are developing new techniques and equipment for the nondestructive evaluation of materials and components. The major emphasis has been on eddy-current, ultrasonic, and penetrating-radiation methods.

We have designed a new multifrequency oscillator and power and video amplifiers for the phase-sensitive eddy-current instrument. The improved circuits allow higher frequency operation, reduced harmonic distortion and decreased drift due to temperature changes. We have also designed new instruments operating on the beat-frequency principle for very accurate measurement of electrical resistivity.

In ultrasonics we have continued study on fabrication of realistic reference standards using electro-discharge machining with emphasis being placed on correction factors to be applied for circumferential notches.

4. Zirconium Metallurgy

Two lots of Zircaloy-4 and four lots of Zircaloy-2 tubing have been received from commercial vendors. The "average" basal pole figures were determined by the microhardness technique. Axial tension and compression tests were completed on all six lots of tubing. Torsion tests are in progress.

[redacted]

The method reported by Wheeler and Ireland for determining the yield surface of anisotropic materials by analysis of hardness anisotropy was improved. It is now possible to determine the biaxial yield loci accurately on all three biaxial stress planes from Knoop microhardness measurements on a specimen of the material. The agreement between experimental and the predicted data is excellent.

A method is reported for correcting Knoop microhardness measurements for anisotropic recovery to improve the fit between the experimental data and the biaxial yield behavior predicted from the hardness measurements.

An empirical correlation for Zircaloy-2 has been established between tensile and compression yield strengths, yield strength ratios, and strain anisotropy constants (k values). It is now possible to calculate five yield strengths, and ten anisotropy constants from an experimental measurement of one yield strength and the two associated anisotropy constants. The three dimensional anisotropy of yield strengths and plastic flow in uniaxial tension and compression in Zircaloy-2 can be completely described to within an accuracy of 5% or better from data obtained by one simple uniaxial tensile or compression test, whatever the texture or the orientation of the texture in the material. An example calculation is presented to demonstrate the method.

The behavior of single crystal and polycrystalline zirconium alloys in pure shear is being studied. Single-crystal specimens are being used to obtain values of critical resolved shear stress for the operation of all possible slip systems, including a $\langle 11\bar{2}3 \rangle$ slip direction. Polycrystalline specimens are being used to determine how texture is changed during pure shear. The data will be used in the analysis of texture development during fabrication, so that texture can be controlled in commercial mills by design of the strain paths of the fabrication sequence. The behavior of two polycrystalline zirconium specimens is presented. The data indicate that all grains, whatever their initial orientation, will rotate and deform to a single final crystallographic orientation if the shear is sufficiently large. The basal pole of the grains are at 65° to the shear direction, 60° to the normal of the

[redacted]

shear plane of the specimen, and 40° from the direction normal to those two, when the shear direction is in the normal direction of rolled sheet zirconium. The crystallography of the shear plane and direction is not yet well established.

A polar chart recorder was electrically coupled to a polarizing light microscope to read directly stage and analyzer rotation. This permits rapid and direct plotting of the basal pole position in space of individual grains. Such measurements on 100 to 200 grains of a specimen can be used to determine a quantitative basal pole density figure for either macrotexture or microtexture. Texture variations and texture gradients can now be examined in much more detail and much more easily than possible before.

Electrical conductivities of oxide films in place on zirconium specimens are being measured in an attempt to relate electrical and optical properties to reveal information on the defect structures present in the films. Anodic oxide films formed in a solution containing phosphoric acid have lower conductivities and dissolution rates in the metal than do anodic films formed in 1% KOH at the same film thickness and experimental conditions. Absorption spectrophotometry indicates the presence of the phosphate ion in the films formed in solutions containing phosphoric acid. It is believed that the phosphorus incorporated in the film causes the differences observed in the properties.

Single crystals were grown in as-deposited crystal bar zirconium by zoning at temperatures below the melting point so that impurities would not be lost by vaporization. Voids and cracks stopped the growth of individual grains, and none of the grains occupied the entire cross section of the bar.

Single crystals of Zircaloy-2 up to 5 cm long were grown in 7-mm-diam rods after quenching from the beta field. The yield is too low as yet, being not more than 10%; however, the as-grown crystals have a higher perfection than do similarly grown crystals of zirconium.

Large single crystals up to 15 cm long by 1 cm wide were grown in Zircaloy-4 tubing after beta quenching. Regions not beta quenched remained fine grained. The large grains were more than twice as large as those produced in Zircaloy-2 by the same technique.

[redacted]

Another single-crystal sphere of zirconium has been oxidized in air. The pattern showing the anisotropy of oxidation is much sharper than previously observed, and shows more detail. Greater perfection of crystalline structure, better surface preparation, or both may have been the cause of a sharper pattern with more detail.

A single-crystal sphere of hafnium was oxidized in air in the as-grown condition. The pattern of anisotropy of oxidation is like that of zirconium in some respects but totally unlike it in others. The fastest oxidation rate was observed near $\{10\bar{1}3\}$ and $\{31\bar{4}0\}$ on the hafnium, as compared to (0001) and $\{10\bar{1}0\}$ in zirconium.

5. Fission-Gas Release and Physical Properties of Fuel Materials During Irradiation

A hollow-cylinder specimen of single-crystal UO_2 is being irradiated for the purpose of measuring thermal conductivity during irradiation. In these experiments the specimen is oscillated sinusoidally in the reactor so as to oscillate the neutron flux and thus oscillate the fission rate in the specimen in a sinusoidal manner. The specimen temperature, measured by axial thermocouples, will also oscillate in response to the changing fission power. The base specimen temperature can be controlled by air-cooling the outside of the specimen capsule.

The response of the specimen temperature will not be instantaneous with change of fission power, but will have a time lag depending on the specific heat, thermal conductivity, and emissivity of the specimen. The amplitude of the temperature oscillations will depend upon the amplitude of the fission-rate oscillations and the frequency of the oscillations. From measurements of phase shift and temperature amplitude as a function of frequency and amplitude of fission-rate oscillations, the thermal conductivity of the specimen can be calculated. By changing the axis of fission-rate oscillations and the air-cooling rate, the change of thermal conductivity as a function of fission rate and temperature can be measured.

An attempt to reirradiate specimens that were stored for a year was not successful because the specimens were broken, probably during the capsule handling.

[redacted]

[redacted]

6. Irradiation Effects on Alloys and Structural Materials

The Radiation Metallurgy Section of the Solid State Division at ORNL is continuing its study of radiation-hardening and radiation-embrittlement in the BCC metals and of radiation effects on diffusion-controlled reactions in alloys. In this report, recent progress is reported on (1) investigations of the effect of radiation and post-irradiation annealing on the impact properties of simulated weld heat-affected-zone samples of a commercial pressure vessel steel, (2) radiation-hardening and post-irradiation annealing in iron and steel, with special emphasis on the effect of dose rate, (3) dislocation dynamics in irradiated iron by stress relaxation techniques, and (4) plastic deformation in niobium, including the preparation and purification of single crystals, the use of Borrmann anomalous x-ray transmission to see dislocations in stereo view, etch-pit measurements of dislocation velocity, slip line observations in unirradiated and irradiated single crystals, and stress relaxation measurements.

Since the heat-affected-zone adjacent to welds in a welded structure often has poorer notch-impact ductility, this region may be of critical importance in the overall integrity of a reactor pressure vessel. Unirradiated simulated weld heat-affected-zone samples of ASTM A-212B pressure-vessel steel corresponding to a heat input of 100,000 joules/inch exhibited a ductile-brittle transition temperature at 20 ft-lbs of 60°C, which is about 80°C higher than for the base plate. Despite the higher initial ductile-brittle transition temperature, the heat-affected-zone samples for 100,000 joules/inch heat input underwent an increase in ductile-brittle transition temperature of about the same magnitude as for the base plate (an increase of about 90°C after irradiation to 9×10^{18} neutrons/cm^2, $E > 1$ Mev, at 70°C). Another series of heat-affected-zone samples, corresponding to 50,000 joules/inch, exhibited similar properties to those of the base plate before and after irradiation. Both series of heat-affected-zone samples showed poorer response to post-irradiation recovery anneals.

[redacted]

[redacted]

The effect of radiation and post-irradiation annealing on the tensile properties of ASTM A-212B pressure-vessel steel is also being studied. Irradiation at 235°C to about 10^{19} neutrons/cm^2 (E > 1 Mev) produced about a 75% increase in yield stress, whereas approximately the same dose at 292°C caused an increase of only about 50%. Upon post-irradiation annealing, the 292°C-irradiated samples recovered at somewhat higher temperatures and more gradually than the 235°C-irradiated samples.

Because of the disparate dose rates at which reactor vessels are exposed and materials evaluation irradiations are done, it is important to determine whether dose rate has a specific influence on radiation hardening and embrittlement. The dose rate effect is being investigated for radiation hardening in vacuum-melted iron. For values corrected to a constant dose of 4.6×10^{18} neutrons/cm^2 (E > 1 Mev) at 94°C and test temperature of 30°C, a three-fold increase in yield stress was observed, but over a dose-rate range from 4 to 300×10^{11} neutrons/cm^2 (E > 1 Mev) there was only a slight tendency for greater hardening at the lower dose rates. Whether this apparent trend is real or not will be more easily decided when samples from a still lower dose-rate irradiation are tested. Results are also described below for tensile tests as a function of grain size, strain rate, and post-irradiation annealing. For a two-hour annealing time, the temperature for 50% recovery is about 350°C and the annealing activation energy is about 3 ev.

In the investigation of dislocation dynamics in iron by stress relaxation techniques, an internal or threshold stress is determined that must be exceeded for macroscopic dislocation motion. It is found that radiation hardening in iron is governed mostly by the increase in this stress rather than a change in the stress dependence of the dislocation velocity. The stress relaxation measurements also yield a curve for the activation volume for plastic deformation as a function of effective shear stress. This curve was found to be the same for irradiated and unirradiated samples.

Our study of plastic deformation in single crystal niobium has continued since the last reporting period. As part of the Research

[redacted]

[redacted]

Materials Program in the Solid State Division, an electron-beam floating-zone refiner has been installed and the analysis of the purity of the niobium single crystal produced in the refiner has begun. A particularly striking and promising development is the success in achieving anomalous x-ray transmission or Borrmann topographs for the single crystals of niobium. These photographs enable one to see dislocations in stereo view in relatively thick samples and are an indication that the dislocation densities are quite low (less than 10^5 dislocations/cm^2). The low dislocation density is borne out by direct counting of dislocation etch pits. The etch-pitting technique is also being used for the first time for niobium to measure the dislocation velocity as a function of applied stress.

Slip line observations have been made on polished surfaces of irradiated and unirradiated niobium. They clearly show the tendency for inhomogeneous slip and the clustering of slip lines into coarse bands in irradiated samples. Stress relaxation measurements have also been carried out on the single crystal niobium tensile samples.

In collaboration with investigators in the Metals and Ceramics Division at ORNL, an experiment in the Thermal Flux Irradiation Facility in the BSR is underway on grain-boundary radiation-embrittlement in Hastelloy-N nickel alloys.

[redacted]

[redacted]

PART I.

METALS AND CERAMICS DIVISION

[redacted]

[redacted]

[redacted]

1. CONTROLLED PRECIPITATION IN NUCLEAR MATERIALS

J. L. Scott J. P. Hammond

Work is in progress to develop means for improving the performance properties of both fissionable and nonfissionable materials by optimizing the microstructure through controlled precipitation of stable dispersed phases.

Effect of Dispersed Precipitates on the Properties of Ceramic Materials

Precipitation Studies in Alumina and Magnesia D. I. Matkin[1]

In order to understand the precipitation process that occurs during heat treatment of titanium-doped Al_2O_3, we have recently been studying the identification of the whisker-shaped precipitates. Initial studies on titanium-doped Al_2O_3 single crystals were unsuccessful so we have resorted to a simpler system, zirconium-doped MgO. Previous identification of precipitates in MgO has involved the selective etching away of the matrix, either for surface-reflection electron diffraction or for selected-area electron diffraction of precipitates completely extracted from the matrix.[2,3] By these techniques, precipitates in undoped, but impure, as-received crystals of MgO were identified as stabilized cubic ZrO_2, some of which went into solution during annealing at 2000°C (ref. 3). Subsequent aging at 1300°C produced whisker-shaped precipitates that have been identified as $CaZrO_3$ (ref. 3). We have used x-ray diffraction techniques to follow these changes, and the results are discussed below.

---

[1]On loan from AERE, Harwell, England.

[2]J. D. Venables, J. Appl. Phys. 34, 293 (1963).

[3]D. I. Matkin and D. H. Bowen, Phil. Mag. 12, 1209 (1965).

In the as-received, impure crystals, two sets of x-ray lines were obtained. One set was consistent with magnesium-stabilized cubic ZrO_2, while the other set was consistent with calcium-stabilized cubic ZrO_2. The lattice of the cubic ZrO_2 in both cases was found to have a unique orientation relationship with the lattice of the MgO matrix, namely, [100] ‖ [100]. After the crystals had received a 2000°C anneal in argon followed by rapid cooling, the magnesium-stabilized ZrO_2 precipitates appeared to have gone into solution while the calcium-stabilized ZrO_2 remained in precipitate form. No diffraction lines were observed from the $CaZrO_3$ whiskers, probably because there is no unique orientation relationship between the $CaZrO_3$ lattice and the MgO lattice.

Dispersion Strengthening of Metals by Controlled Precipitation

J. P. Hammond

Aluminum Alloys

Studies on dispersion hardening of aluminum using the SLIS method[4] and cerium and beryllium as alloying additions are continuing. Of three methods examined for preparing powders, one using a spinning, consumable anode for generating liquid particles preliminary to quenching on a rotating disk appears to offer greatest promise for early development. However, to achieve acceptable results by this method, the anode should be of a eutectic alloy and should be homogeneous throughout.

Arc-cast buttons were prepared of the alloy systems of interest with which to establish their aluminum-rich eutectics. Examinations of the aluminum-cerium alloy specimens were completed and the eutectic was shown to occur at 2.32 at. % (11 wt %) Ce by the disappearing-phase metallographic method. Anodes (2 1/4-in.-OD and 7 in. long) for preparing powders in this alloy were successfully fabricated by a process

---

[4]A. R. Kaufmann and W. C. Muller, Development of Zirconium-Base Alloys Strengthened by SLIS Technique, NMI-1263 (Jan. 15, 1965).

employing hot extrusion in conjunction with straight-polarity, consumable-electrode, arc melting. Anodes in the aluminum-beryllium alloy appear to be fabricable by a simpler method, that of induction melting followed by casting and machining. Preparation of anodes in the aluminum-cerium alloy was not successful by the latter method as a result of a marked tendency for cerium to segregate at the bottom of the casting. Anodes in the two alloys will be shipped shortly to Nuclear Metals, Inc., for conversion to powder.

Thorium Alloys

In the last quarterly report,[5] hot hardness results were given for a Th–1.3% Be alloy prepared by the SLIS method together with those for early attempts to dispersion harden a solid-solution Th–4.65% Zr alloy by internal boronation. In the interim the boronation technique was refined and a procedure for dispersion hardening thorium with ThO_2 by particle embedment was developed. In both procedures, the final step involves kneading the additive (ThO_2 or boron) into fine metal powder by ball-milling.

Results of hot hardness tests on specimens prepared by these techniques are given in Table 1.1 (specimens Nos. 5 and 6, and 9 and 10) along with data for unalloyed cast thorium, the cast Th–5% Zr alloy (most promising of arc-melted alloys),[5] the SLIS-prepared Th–1.3% Be alloy, and an early boronated Th–4.65% Zr alloy (specimens 1–4), for comparison. It should be noted that specimen 4 contained 1.1% B, which corresponds to the amount required to form stoichiometric ZrB_2 (the intended precipitate) with the zirconium present. Specimens 5 and 6 contained 0.54 and 0.27% B, respectively, and samples 7 and 8 represent hardness reruns on Nos. 5 and 6 after a stabilization heat treatment of 24 hr in vacuum at 800°C.

---

[5]J. P. Hammond, Fuels and Materials Development Program Quart. Progr. Rept. Dec. 31, 1965, ORNL-TM-1400, pp. 8–12.

Table 1.1. Hot Hardness of Dispersion-Hardened Thorium Alloys

Specimen Number	Method of Hardening	Composition	Hot Hardness[a] (DPHN) at Temperatures (°C) of									
			25	100	200	300	400	500	600	700	750	800
1[b]	None	Thorium	85	45	41	35	33	30	22	15	11	ND
2[c]	Alloying	Th–5% Zr	104	93	83	90	77	71	60	42	37	ND
3[d]	SLIS	Th–1.3% Be	139	140	105	105	114	86	71	45	37	28
4[e]	Boronation	Th–4.65% Zr–1.1% B	126	ND	ND	ND	90	69	49	40	ND	28
5[f]	Boronation	Th–4.65% Zr–0.54% B	494	ND	ND	ND	320	208	120	81	ND	61
6[g]	Boronation	Th–4.65% Zr–0.27% B	419	ND	ND	ND	156.5	139	89.5	54	ND	39.5
7[h]	Boronation	Th–4.65% Zr–0.54% B	486	ND	ND	ND	196.5	179	125.5	80	ND	60.5
8[i]	Boronation	Th–4.65% Zr–0.27% B	417	ND	ND	ND	161.5	135.5	80.5	48.5	ND	37.0
9[j,k]	Embedment	Th–5% ThO_2	326	ND	ND	ND	166	126.5	68.5	23	ND	7
10[k,l]	Embedment	Th–10% ThO_2	296	ND	ND	ND	138.5	91.5	60.5	21.5	ND	5.5

[a]Values reported represent average of two measurements.

[b]Chemical analysis: 99.8 wt % Th, 340 ppm C, 2000 ppm O, and 180 ppm N.

[c]Thorium has same chemical content as that used in specimen 1 and was prepared by arc casting.

[d]Thorium same as in specimen 1; prepared by horizontal-jet SLIS method and hot upset extrusion at 600°C.

[e]Thorium same as in specimen 1; prepared from –325 mesh powder of hydrided and dehydrided alloy and 1.1 wt % B by ball-milling dry for 3 hr, hot pressing at 1000°C, and extruding at 750°C.

[f]Thorium same as in specimen 1; prepared by hydriding alloy casting, ball-milling in hexane 24 hr, dehydriding, introducing 0.54% ball-milled boron, again ball-milling in hexane for 24 hr, cold pressing at 37 tsi, sintering in vacuum 3 hr at 800°C, and extruding at 750°C.

[g]Differs from specimen 5 only in the amount of boron added.

[h]Same as in specimen 5 and annealed in vacuum 24 hr at 800°C.

[i]Same as in specimen 6 and annealed in vacuum 24 hr at 800°C.

[j]Thorium was calcium reduced; chemical analysis: 0.64 wt % ThO_2, 1500 ppm Ca, other elements individually <100 ppm.

[k]Prepared by hydriding calcium-reduced thorium powder and then ball-milling with 5% ultrafine ThO_2 in hexane 24 hr, dehydriding, ball-milling again in hexane 24 hr, cold pressing at 37 tsi, sintering in vacuum 3 hr at 800°C, and extruding at 750°C.

[l]Differs from specimen 9 only in the amount of ThO_2 added.

ND: Not determined.

It is to be noted that although refinement of the method for dispersing the boron resulted in greatly improved hardness (compare results for specimens 5 with 4), still additional improvement is desirable, especially as respects the microstructure and conservation of the amount of boron (separated ^{11}B isotope) used. Figure 1.1a shows that boron in the earlier test (specimen 4) formed clumps surrounded by a shell of reacted boron, possibly ThB_6 or ThB_4. While the clumping was circumvented by the modified procedure (specimen 5) a dispersion of fairly coarse particles of a reaction product persisted (Fig. 1.1b). To account for the extraordinarily high hot hardness achieved by the boronation process, it is likely that the matrix contains a submicroscopic dispersion (ZrB_2). The stabilization heat treatment at 800°C did not significantly soften these alloys for the higher test temperatures of 600 to 800°C (compare specimens 7 with 5 and 8 with 6). The hardnesses obtained for the ThO_2-containing dispersions at the high temperatures are curiously low (specimens 9 and 10), notwithstanding the fact that the microstructures showed an extremely fine distribution of the dispersant.

Because the boronation method of dispersion hardening thorium was far superior to the other methods examined, future work will concentrate on this process. Attention will be given to the mechanisms involved in hardening, reduction of amount of boron used, and the use of a colloidal or amorphous grade of boron.

[redacted]

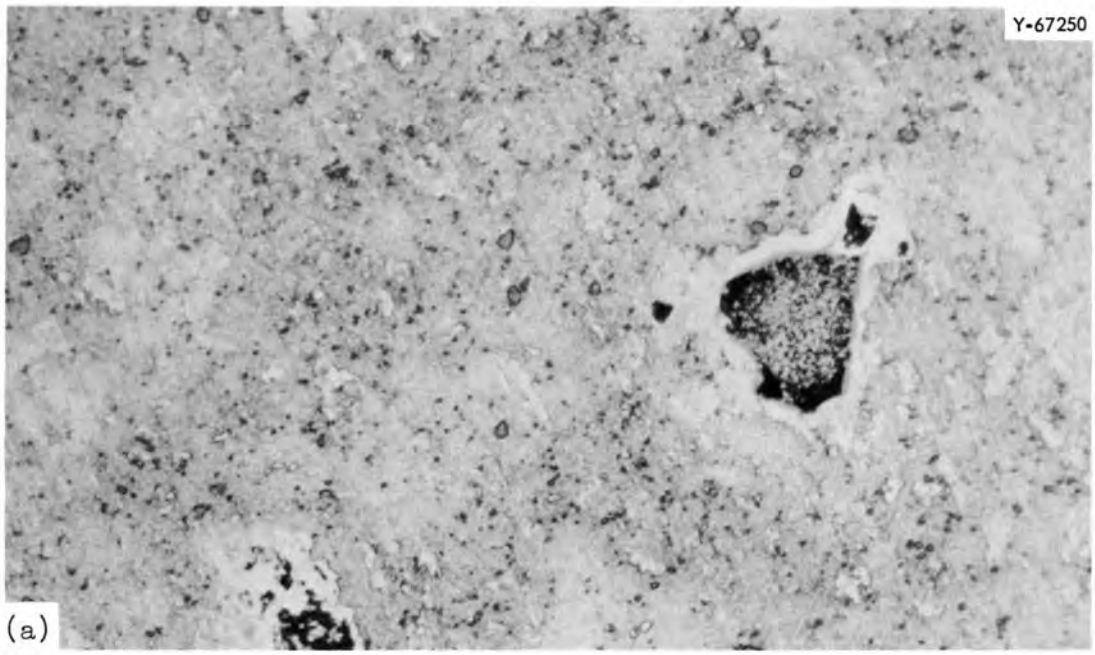

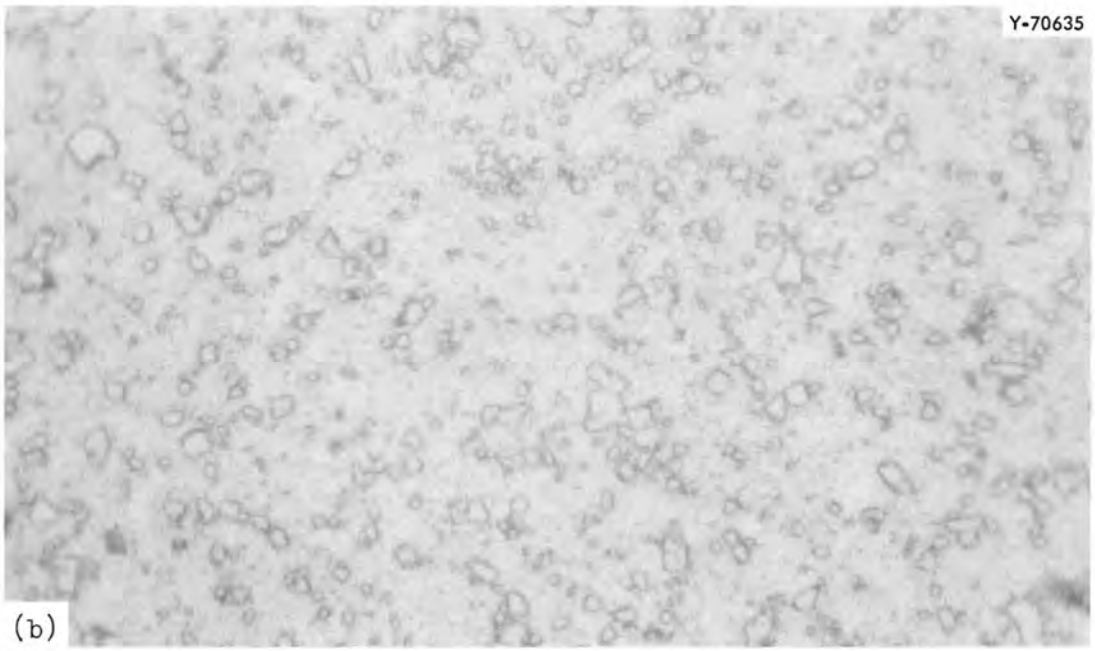

Fig. 1.1. Microstructures of Th–4.65% Zr Alloys Dispersion Hardened by Internal Boronation. (a) Prepared by dry ball-milling 1.1% B into –325 mesh dehydrided alloy powder 24 hr, followed by hot pressing at 1000°C and extruding at 750°C. Specimen 4 in Table 1.1. 500×. (b) Prepared by ball-milling hydrided alloy powder 24 hr in hexane, dehydriding, then introducing 0.54% once ball-milled boron and ball-milling the mixture in hexane 24 hr followed by cold pressing, sintering at 800°C and extruding at 750°C. Specimen 5 in Table 1.1. 1500×. Both polish etched with 5% oxalic acid.

[redacted]

2. FUEL ELEMENT DEVELOPMENT

G. M. Adamson, Jr.

Thermochemical deposition continues to be favored as a promising fabrication tool for refractory metals, alloys, and ceramic fuel compounds. Fabrication of fuels by the direct thermochemical conversion of the halides offers the advantages of remote handling, fast processing, and a minimum of equipment to produce either solid deposits or submicron powders. Currently, irradiation specimens are being prepared both as solid deposits and submicron powders for fabrication of cold-pressed and sintered pellets. It has been demonstrated that UO_2 may be deposited directly onto thoria thus giving a fertile-fissile duplex pellet. Uranium powder has been obtained by direct reduction of UF_6 by lithium vapor with the next step being to synthesize uranium nitride powder.

Experiments in producing UO_2 by thermochemical reduction from chlorides have been terminated due to deaccentuation of the chloride fuel element reprocessing cycle. A topical report summarizing the results is being prepared.

Fabrication schemes currently used for refractory metals involve considerable working of either powder of cast billets to produce tubing or sheet stock. Alloying studies of tungsten-rhenium by thermochemical deposition have progressed to where it is feasible to produce homogeneous deposits; thus, a finished alloy tube may be formed directly by coreduction of the halides. Deposition parameters for specific alloys are currently being determined.

Due to current interest in high-burnup research reactor fuels we have reactivated studies on the fabrication behavior of UAl_3 in aluminum.

Deposition of Uranium Dioxide by Hydroreduction of Uranium Hexafluoride

R. L. Heestand C. F. Leitten, Jr.

Studies of the sintering characteristics of UO_2 powders produced directly by thermochemical conversion are continuing; however, sufficient data for conclusions are not complete at this time. Currently, the

apparatus is being modified to handle enriched materials for preparation of irradiation specimens for both solid and powder UO_2. In the case of powders, an enrichment of 2.5% ^{235}U will be used for fabrication of pressed and sintered pellets 0.400 in. in diameter by 0.5 in. high. Solid deposits for coatings on thoria pellets will be prepared from fully enriched material. This work is being done in conjunction with the thorium utilization program to provide data of mutual benefit to both programs. The fuel concept in this case consists of a fertile thoria pellet coated with a thin layer of fissile material which may be readily removed, thus simplifying reprocessing. Depleted UO_2 has been coated on thoria in thicknesses up to 0.020 in. in recent experiments. Figure 2.1 illustrates a UO_2 coated thoria pellet of this type. On metallographic examination, cracks are observed in the coating along with cracks that originate in the thoria and progress through the UO_2, such as is shown in Fig. 2.2. A number of cracks of this type were present in the thoria prior to coating. This, however, does not appear to affect the bond between the two oxides which has maintained its integrity. In the next quarter, sufficient pellets for irradiation experiments will be produced.

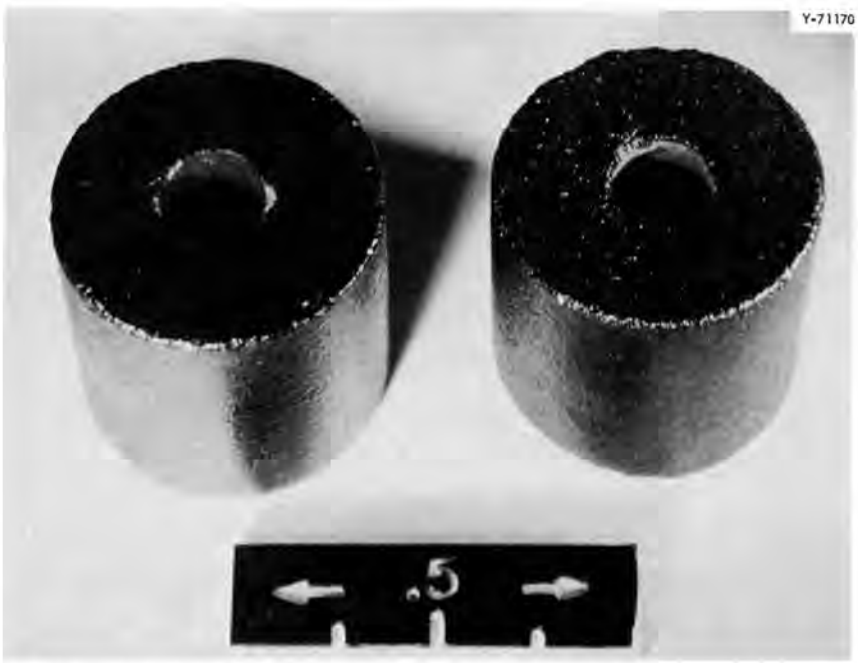

Fig. 2.1. Thoria Pellets, 0.400 in. in diameter, Coated with 0.020-in-thick UO_2 by Thermochemical Deposition.

[redacted]

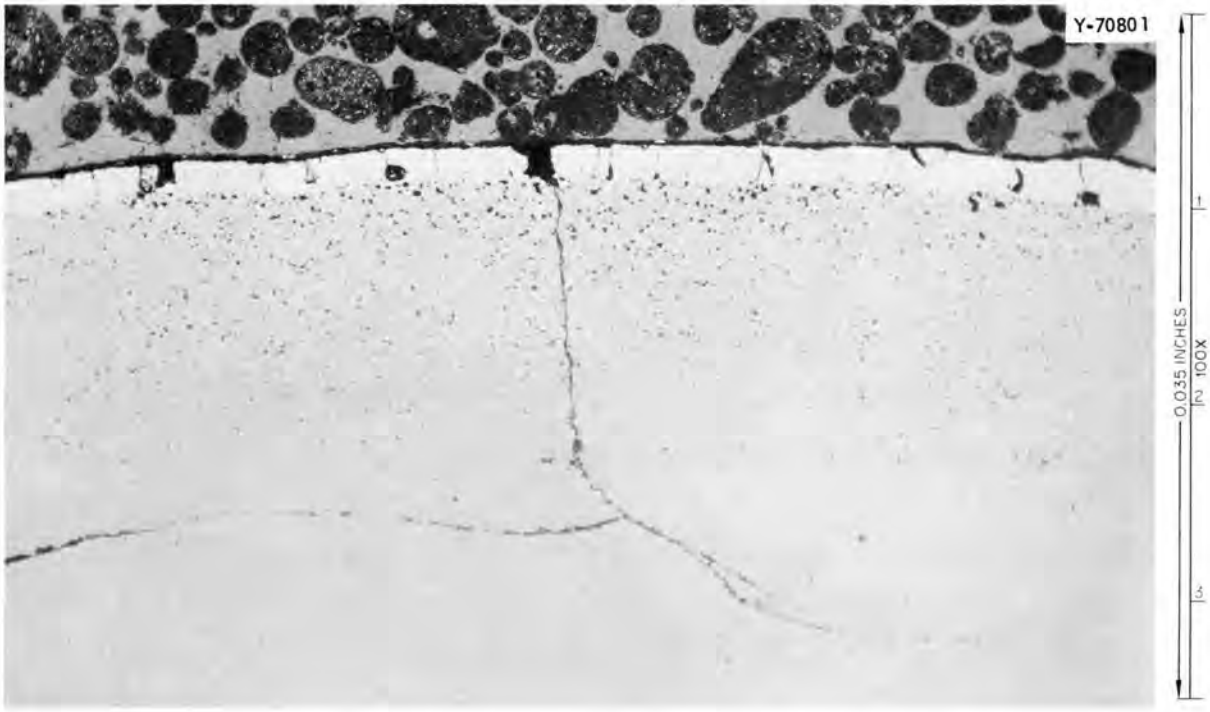

Fig. 2.2. Interface of UO_2 Coating on Thoria Pellet Showing Propagation of Cracks. As polished.

Deposition of Uranium Compounds by Lithium Vapor Reduction of Uranium Hexafluoride

W. C. Robinson C. F. Leitten, Jr.

Studies were continued to examine the feasibility of the direct fabrication of uranium compounds by lithium vapor reduction of UF_6. The direct synthesis of UO_2 fuel from gaseous uranium halide has already been demonstrated[1,2] and involves the reduction-hydrolysis of the uranium halide with hydrogen and oxygen. Fast reactor considerations indicate the advantages of a UN or UC fuel. Hydrogen, however, is not a sufficiently strong reducing agent to allow synthesis of these refractions. Therefore, vaporized lithium is being investigated. It is anticipated that reduction of UF_6 with lithium in the presence of a

---

[1]R. L. Heestand and C. F. Leitten, Jr., Nucl. Appl. 1(6), 584 (1965).

[2]F. H. Patterson, W. C. Robinson, and C. F. Leitten, Jr., "Conversion of Uranium Chlorides to Urania by Gas-Phase Reduction-Hydrolysis," to be published.

[redacted]

nitrogenous or carbonaceous gas will produce the desired products UN or UC.

The feasibility of the lithium reduction of the UF_6 to uranium metal was established previously,[3,4] and the reaction was forced to occur in the vapor phase.

The uranium metal product was in the form of a very fine powder which reacts when exposed to H_2O or air to form UO_2. In the experiments reported previously, mixtures of LiF and uranium metal powder were found in the reaction zone since the reactions were performed at relatively low temperatures (750°C). Experiments in this period were run at temperatures in increasing increments ranging from 800 to 1000°C. Lithium transfer rates were high at these temperatures, and the reaction product was obtained as a pyrophoric uranium metal powder which collected in the cold trap of the system. Lithium fluoride was collected as a deposit at the outlet of the furnace hot zone along with small amounts of UF_4. No massive deposits of uranium metal were obtained.

We have modified the apparatus for experiments to synthesize uranium nitride powder by adding nitrogen to the injection system and installing powder collectors in the exit gas stream. Future experiments will be oriented toward determining parameters for producing uranium nitride powder.

Preparation of Uranium Dioxide by Hydroreduction of Uranium Chlorides

F. H. Patterson W. C. Robinson
C. F. Leitten, Jr.

The fluoride and the chloride volatility processes have both been applied for reclaiming fuels from spent zircaloy-clad uranium-plutonium

---

[3]W. C. Robinson and C. F. Leitten, Jr., Fuels and Materials Development Program Quart. Progr. Rept. Sept. 30, 1965, ORNL-TM-1270, pp. 11–12.

[4]W. C. Robinson and C. F. Leitten, Jr., Fuels and Materials Development Program Quart. Progr. Rept. Dec. 31, 1965, ORNL-TM-1400, pp. 16–17.

dioxide fuel elements.[5,6] The chloride yields the uranium as mixed UCl_5-UCl_6 while the fluoride separation process gives UF_6 as a product. The chloride separation work demonstrated that uranium chlorides may be converted to uranium dioxide in a "closed-loop" fuel-recycle system. Laboratory quantities of UO_2 were produced by the direct reaction of mixed UCl_5-UCl_6 with oxygen and the subsequent reduction of the intermediate reaction product by wet hydrogen.[7] Chemical analysis shows that the powders have oxygen-to-uranium ratios of approximately 2.02 and residual chlorine contents of approximately 50 ppm.

No further evaluation of this material was done since characteristics are similar to powder produced by the thermochemical reduction of UF_6 to UO_2 (ref. 8). Further optimization of the hydroreduction process for the cholorides was discontinued because in the decladding step the urania-plutonia separation proved to be more advantageous by the fluoride volitilization process and also the fluoride volitilization process involves fewer corrosion problems.[9]

The calculations, experimental procedure, and results of the direct conversion of the uranium chlorides to UO_2 experiments will be presented in a forthcoming report.[2]

---

[5]T. A. Gens, Chloride Volatility Experimental Studies: The Reaction of U_3O_8 with Carbon Tetrachloride and Mixtures of Tetrachloride and Chlorine, ORNL-TM-1258 (August 1965).

[6]Reactor Handbook (ed. by F. M. Stoller and R. B. Richards), 2nd ed., Vol II, Chap 6, Interscience Publishers, Inc., New York, 1961.

[7]F. H. Patterson, W. C. Robinson, C. F. Leitten, Jr., Fuels and Materials Development Program Quart. Progr. Rept. Dec. 31, 1965, ORNL-TM-1400, pp. 15–16.

[8]R. L. Heestand, R. A. Potter, C. F. Leitten, Jr., Fuels and Materials Development Program Quart. Progr. Rept. Dec. 31, 1965, ORNL-TM-1400, pp. 13–14.

[9]Private communication with W. H. Carr, Chemical Technology Division, Oak Ridge National Laboratory.

Deposition of Tungsten Alloys

J. I. Federer C. F. Leitten, Jr.

Thermochemical deposition studies of tungsten-rhenium alloys have continued for the purpose of developing an alternate fabrication process for refractory-metal-clad, high-temperature fuel elements. Previous studies of hydrogen reduction of WF_6-ReF_6 mixtures at temperatures between 450 and 800°C have shown that compositional variations occur in the deposits because ReF_6 is more easily reduced to metal than is WF_6 (ref. 10). Thermodynamic calculations, however, indicate that under equilibrium conditions the composition of the deposits will correspond to the metal content of the WF_6-ReF_6 mixture when the reduction occurs at about 1000°C. Thus, the reaction must be prevented from occurring in the temperature gradient leading to the hot zone, and the reaction must be completed in the 1000°C hot zone.

Reaction studies at higher temperatures are being conducted in an apparatus similar to that used previously except that a stationary injector is used to deliver the WF_6-ReF_6 mixture directly into the hot zone. The injector is 3/8-in.-OD and water cooled to prevent deposition and ultimate plugging on the tip. Mandrel surface temperatures were 475°C adjacent to the tip and 800°C at a point 3 in. downstream for a nominal furnace temperature of 800°C. Consequently, the calculated optimum deposition temperature of 1000°C has not been attained even though the furnaces have been operated at near maximum power input.

Initial experiments were conducted to determine the character and distribution of the deposit in a stationary hot zone for a furnace temperature of 800°C, a pressure of 10 torr, and H_2, WF_6, and ReF_6 flow rates of 1000, 30, and 10 cm^3/min, respectively. When hydrogen was injected with the WF_6-ReF_6 mixture, the deposit began 1 in. upstream from the injector tip and ended 6 to 7 in. downstream. When the hydrogen

---

[10] J. I. Federer and C. F. Leitten, Jr., Fuels and Materials Development Program Quart. Progr. Rept. Mar. 31, 1965, ORNL-TM-1100, pp. 7–9.

flowed around the injector, the deposit began adjacent to the injector tip and ended about 4 in. downstream. Since the deposit was confined to a smaller area in the latter case, that arrangement was selected for deposition in a moving hot zone. In both cases the surface texture of the deposits was smooth.

Deposits have been prepared using this injector design in a moving hot zone in an effort to obtain alloys containing 5, 25, and 90% Re. The nominal furnace temperature was 800°C, and the WF_6 and ReF_6 flow rates were in proportion to the desired rhenium content of the alloys. The surface texture of deposits containing approximately 5 and 25% Re was generally smooth with no ridges or large nodules. The rhenium-rich deposits, however, consisted of relatively small amounts of solid coating which were distinctly nodular and large amounts of powder.

The rhenium content of several deposits is shown in Table 2.1. Deposits WRe-73, -74, and -79 were intended to contain 25% Re. The most uniform of these was WRe-73 which averaged $26.1^{+1.0}_{-0.7}$% Re over a 6-in. length. Deposit WRe-75 approached the intended 90% Re content.

Table 2.1. Rhenium Content of Deposits Prepared in a Moving Hot Zone With an Injector

Distance Along the Deposit (in.)	Rhenium (%)			
	WRe-73	WRe-74	WRe-75	WRe-79
1	27.1	32.9	86.3	25.0
2	a	a	91.8	27.9
3	25.6	24.2	89.0	24.7
4	a	a	87.6	23.0
5	26.1	24.8	81.9	22.9
7	25.4	16.8		
9	21.4			
9.5	19.9			

[a]Sample not analyzed.

The microstructure of the alloys shown in Fig. 2.2 indicate an improvement in uniformity of composition through the thickness of the deposits. These alloys, which contain about 25% Re, were prepared under similar conditions except that an injector was not used for the alloy shown in Fig. 2.2a. The latter exhibits definite layers which etched at different rates. The microstructure of WRe-73 in Fig. 2.2b shows less evidence of a rhenium gradient through the thickness. Electron probe analysis, in fact, shows that the rhenium content is very uniform through the thickness except for a slightly higher value in the thin layer on the last deposited surface.

For the deposit shown in Fig. 2.2a, the reacting gases encountered a temperature gradient of 25°C to the furnace temperature (800°C), whereas in the case of WRe-73 the gases encountered temperatures ranging from 475 to 805°C. This temperature range is well below the thermodynamically calculated optimum temperature for homogeneous deposition (1000°C), yet the microstructure in Fig. 2.2b indicates better radial uniformity of composition. Further improvements are expected in the alloys deposited at a nominal furnace temperature of 900°C. Presently, experiments are being conducted to determine whether a noncooled hot injector can be used in order to increase the temperature at which the reaction actually occurs.

Rhenium-rich alloys have been deposited in the external coating apparatus previously described.[11] In this apparatus, 3/4-in.-OD mandrels, heated internally, are contained within a 4-in.-ID × 12-in.-long mixing chamber. This design is intended to minimize the nonuniform depletion of ReF_6 in the reacting gases which occurs during deposition on the inner wall of a relatively long, narrow tube. Thus, the possibility exists of depositing alloys of uniform composition at temperatures less than 1000°C in the external coating apparatus. Alloys have been deposited at about 600°C, a 10-torr pressure, and H_2, WF_6, and ReF_6 flow rates of 1000, 45, and 5 cm^3/min, respectively. These deposits have usually contained

[11] J. I. Federer and C. F. Leitten, Jr., Fuels and Materials Development Program Quart. Progr. Rept. Dec. 31, 1965, ORNL-TM-1400, pp. 19–20.

[redacted]

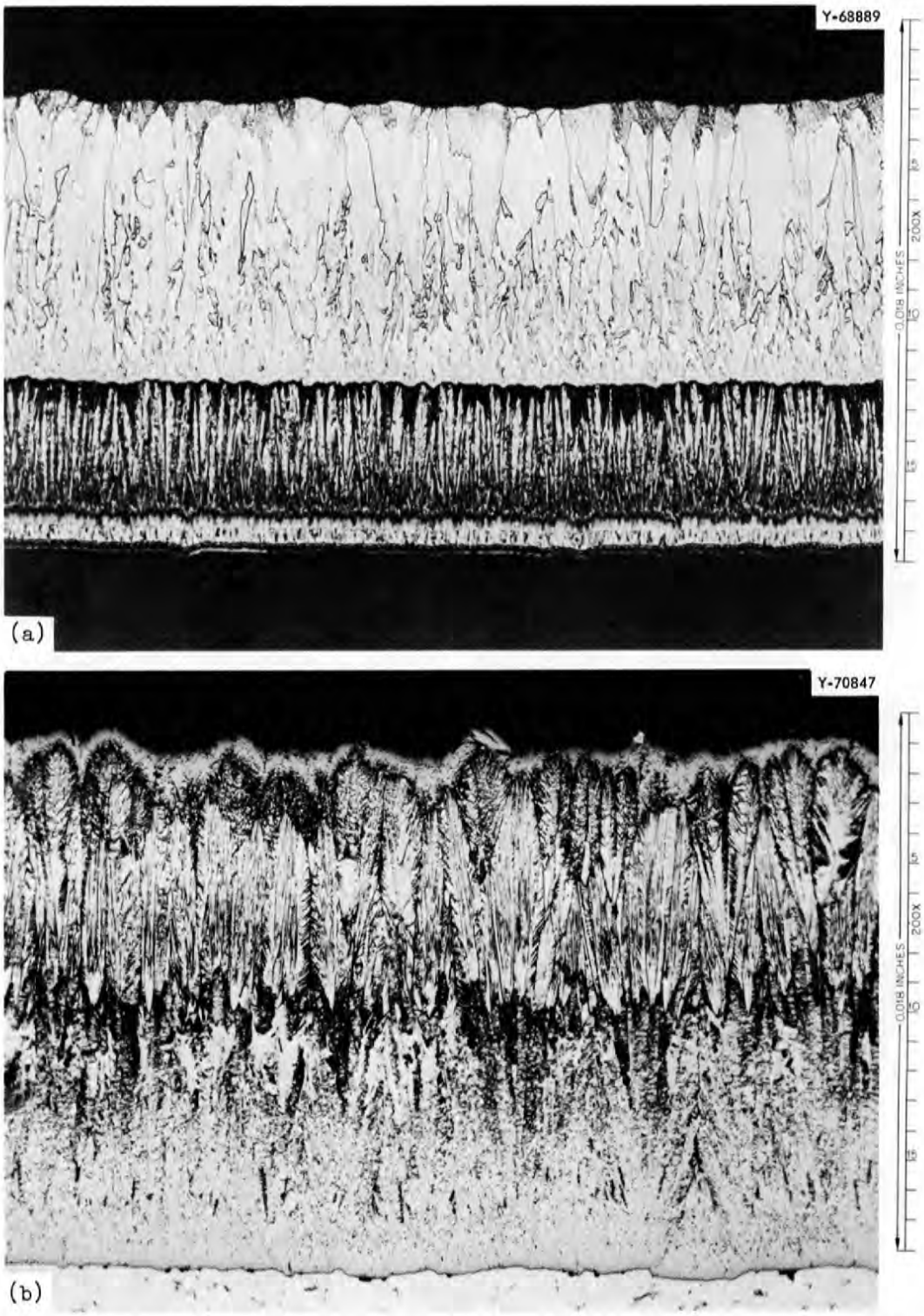

Fig. 2.2. Comparison of Microstructures of Tungsten-Rhenium Alloys Deposited in a Moving Hot Zone. (a) Without an injector for the WF_6-ReF_6 Mixture. (b) With an injector (WRe-73). Etchant: 50 parts NH_4OH and 50 parts H_2O_2 (30%).

[redacted]

regions of nodular growths and dark, porous coatings. Rhenium contents up to 72% have been obtained. The poor quality of the deposits appears to limit the external coating apparatus to tungsten-rich deposits. Deposition of rhenium-rich alloys, such as WRe-75 in Table 2.1, have been more successful in the apparatus using an injector.

Deposition of Molybdenum

J. I. Federer C. F. Leitten, Jr.

Molybdenum has been deposited in an apparatus employing an injector as described in the previous section. These experiments were intended to provide information on the distribution of molybdenum in the deposition zone prior to depositing tungsten-molybdenum alloys. The nominal furnace temperatures were 800 and 900°C with temperature profiles as discussed in the previous section. Both hydrogen and MoF_6 were admitted to the stationary deposition zone through the injector at H_2-to-MoF_6 ratios of 1000:50, 1000:25, and 2000:50 at 800°C and 500:25 at 900°C. Under these conditions, the deposits consisted of numerous growth cones or nodules near the injector tip and a smooth coating further downstream. The deposits were about 5 in. long at 800°C, but only 3 in. long at 900°C. Metal recoveries ranged between 65 and 85% of the metal content of MoF_6 used.

These experiments indicate that optimum conditions for pure molybdenum, and possibly for molybdenum-rich alloys, have not yet been achieved. The possibility of increasing the temperature of the reaction zone by use of an uncooled injector is currently being investigated.

Fabrication of Enriched UAl_3 Dispersion Fuel Plates

W. J. Werner M. M. Martin
J. H. Erwin

The uranium-aluminum intermetallic fissile material under investigation was previously fabricated successfully into four fuel elements for the Oak Ridge Research Reactor.[12] Currently, each element has

[12]W. J. Werner, J. H. Erwin, and M. M. Martin, Fuels and Materials Development Program Quart. Progr. Rept. June 30, 1965, ORNL-TM-1200, pp. 9–12.

completed 80% of the planned 60 at. % burnup without indication of failure. We expect to initiate postirradiation examination on one spent element early in FY-1967.

The fuel elements are of the ORR design with 19 curved fuel plates but differ from the standard element in three ways

1. a 30 wt % UAl_3-Al dispersion replaces the usual 18.6 wt % U-Al alloy core in each fuel plate,
2. loading increases from 200 g ^{235}U to 240 g ^{235}U per element, and
3. fully annealed type 6061 aluminum substitutes for the normal 20% cold-worked type 1100 aluminum cladding.

We used the conventional picture-frame technique to fabricate the fuel plates without difficulty. The plates were of high quality and showed no blister or ultrasonic nonbond indications after two anneals at 500°C. Each fuel compact for the plates was individually prepared by dry bending the powders, cold compacting the mixture at 22.5 tsi, and degassing the dense rectangular shape at a pressure of less than 5×10^{-2} torr for 2 hr at 590°C. Average growth of compacts during the degassing was 1.1%.

In November 1965, work was initiated on the production of a series of instrumented fuel plates for five special ATR fuel elements. Plate design called for a split fuel core consisting of two separate layers with provisions for inserting a thermocouple in the aluminum section between the cores. Additionally, the fuel material was to be stoichiometric UAl_3 supplied by ORNL. Plate fabrication techniques were to be similar to those developed for the production of the HFIR-ATR irradiation test miniature plates[13] and UAl_3 was to be produced according to procedures developed during the production of the four special ORR fuel elements described above. This consisted of hydriding high-purity uranium metal to produce fine particles and intimately mixing with the proper amount of high-purity aluminum by oblique dry blending. The blend was placed in a graphite die and the hydrogen removed by the application of heat and vacuum. The mixture was then hot pressed at 1000°C, followed

[13]M. M. Martin, W. J. Werner, and C. F. Leitten, Jr., Fabrication of Aluminum-Base Irradiation Test Plates, ORNL-TM-1377 (February 1966).

[redacted]

by crushing to the proper particle size. Fabrication innovations added included the use of evacuated billets to eliminate air entrapment under the compacts in the composite assembly, the use of a disk crusher for sizing the UAl_3 to the desired −170 +325 particle size range, and the use of aluminum backup strips during fuel plate marforming to prevent core cracking. Serious swelling problems were encountered during the vacuum degassing treatment performed on the fuel compacts prior to billet assembly. Figure 2.3 shows a comparison of an as cold-pressed structure and the effects of swelling after vacuum degassing at 590°C for 2 hr. The outgassed pellets exhibited a volume change of approximately 14%. A comparison of the average growth of these compacts with the uniform growth encountered when U_3O_8 is substituted for UAl_3 as the fissile material and during ORR production is shown in Table 2.2.

Subsequent experiments to determine the source of this difficulty have been unsuccessful to date. The parameters, composition (wt % UAl_3), outgassing temperature (350 to 590°C), cold-pressing lubricant (CCl_4-stearic acid, acetone-stearic acid, and no lubricant), UAl_3 production method (hydride process and arc cast from 99.97 U metal + 99.999 Al), cold-compacting pressure (5, 10, 22.5 tsi), aluminum dispersant powder (type 101, X8001, and high purity UAl_3 crushing method — hand vs disk), and vacuum degassing of UAl_3 powder prior to blending were studied; using 1/2-in.-diam × 1/2-in.-high pellets. The parameters that affected the swelling were outgassing temperature and pellet composition — the amount of swelling decreasing with decreasing temperature and UAl_3 content. It should be noted that at the ORR composition the swelling was several times that observed perviously. Additionally, the growth predicted for the conversion of UAl_3 to $UAl_{4.5}$ is only 0.65% using 6.7 and 5.7 g/cm^3 as the densities of UAl_3 and $UAl_{4.5}$, respectively.

The appearance of the microstructure of outgassed pellets suggested the formation of a gaseous reaction product at the fuel-matrix interface. Additionally, the odor of the pellets immediately after outgassing suggests the presence of H_2S. Chemical analyses of the aluminum powders and the UAl_3 show that approximately 20 ppm S is present in both materials. Analyses of the gaseous product from vacuum heat-treated pellets, however, failed to substantiate the presence of a sulfurous reaction product.

[redacted]

[redacted]

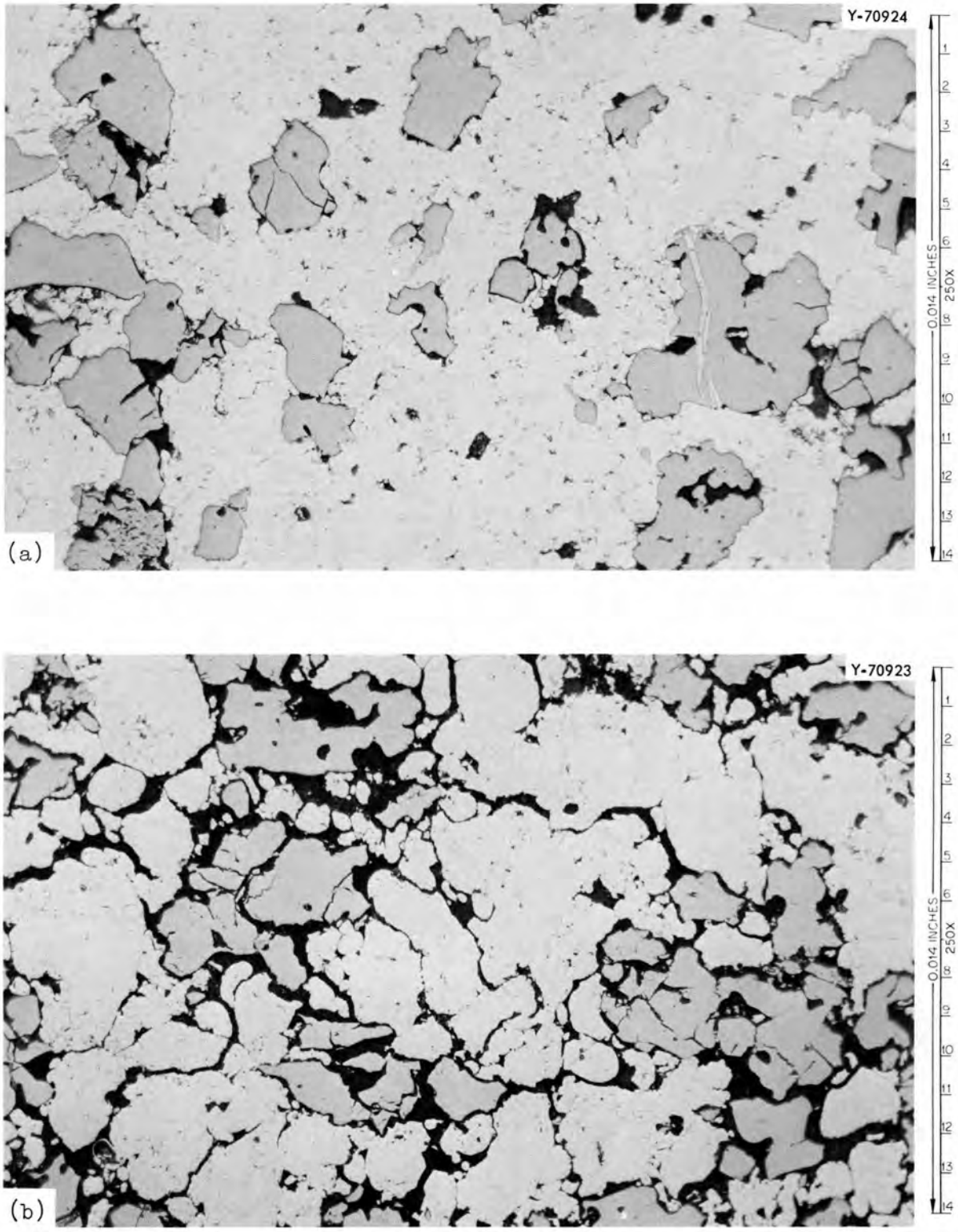

Fig. 2.3. Microstructures of UAl_3-X8001 Compacts. (a) As cold compacted, and (b) after degassing for 2 hr at 590°C in vacuum. As polished.

[redacted]

[redacted]

Table 2.2. Comparison of Average Growth of Fuel-Aluminum Compacts During Vacuum Degassing at 590°C

Type Compact	Composition (wt %)	Volume Change (%)
ATR-UAl_3-Al-B_4C	51.1 UAl_3, 48.7 X8001 Al, 0.2 B_4C	14.44
ATR-U_3O_8-Al-B_4C	44.7 U_3O_8, 55.1 X8001 Al, 0.2 B_4C	0.84
ORR-UAl_3-Al	30.3 UAl_3, 69.7 101 Al	1.12

The swelling problem was circumvented for this particular batch of experimental plates by reducing the outgassing temperature to 525°C where approximately 4% growth occurs. Compacts processed in this manner have been successfully rolled to the desired configuration with no evidence of blistering. Due to the emphasis being placed on the use of this fuel for high-performance research reactors and the difficulty encountered in plate production, we will continue the evaluation of this material combination.

[redacted]

3. NONDESTRUCTIVE TEST DEVELOPMENT

R. W. McClung

Our program is intended to develop new and improved methods of evaluating reactor materials and components. To achieve this we have studied various physical phenomena, developed instrumentation and other equipment, devised application techniques, and designed and fabricated reference standards. Among the methods being actively pursued are electromagnetics (with major emphasis on eddy currents), ultrasonics and penetrating radiation. In addition to our programs oriented toward the development of methods, we are studying these and other methods for evaluation of problem materials and developing techniques for remote inspection.

Electromagnetic Test Methods

C. V. Dodd

Phase-Sensitive Eddy-Current Instrument

Further improvements have been made in the phase-sensitive eddy-current instrument. A new video amplifier has been designed which has reduced harmonic distortion to a value less than 0.2% over a 1 kc to 1 Mc range.

A new oscillator and power amplifier have been constructed having harmonic distortion less than 0.2% from 1 to 1000 kc. The oscillator provides output frequencies of 1, 2, 5, 10, 20, 50, 100, 200, 500, 1000, 2000, and 5000 kc. The power amplifier will supply 1.5 w to a coil and the output voltage varies less than 15 mv for a 15°C temperature increase.

A new discriminator and flip-flop which will work at higher frequencies is being constructed. This new discriminator will allow us to measure the thickness of very thin metal sheets.

Beat-Frequency Eddy-Current Instrument

A new, stable beat-frequency eddy-current instrument has been designed and constructed to measure the electrical resistivity of tensile specimens. The instrument operates at a frequency of 200 kc and has a temperature drift that represents a sample resistivity change of 0.06 microhm cm/°C. Twelve samples were measured a number of times. The repeatability was ±0.2 microhm cm (out of 100 microhm cm), which could be caused by a ±1°C change in the samples. However, small variations in diameter between samples caused a variation in resistivity readings.

A high-frequency beat-frequency instrument has been constructed to measure the diameters of the tensile specimens. The instrument operates at a frequency of 20 Mc and will measure the diameter within 0.0001 in. This measurement is used to correct the resistivity error due to diameter variations.

Ultrasonic Test Methods

K. V. Cook

Tubing Inspection

We are continuing to work on the problems encountered in tubing inspection. A major problem is the establishment of realistic reference notch standards for calibration. Electro-discharge machining appears to be a reliable method for making both outer- and inner-surface notches, and we are continuing to use this technique for our studies. Recently, we have been studying the problems associated with fabricating circumferential notches on both the outside and inside of tubing.

As mentioned previously,[1] preshaping of the etching tool is required if constant depth transverse notches are to be fabricated. For instance, if we assume a cutting tool that initially conforms to the outer surface

[1]K. V. Cook, Fuels and Materials Development Program Quart. Progr. Rept. Dec. 31, 1965, ORNL-TM-1400, p. 36.

[redacted]

of the tube (as shown in Fig. 3.1) the cutting begins at points A, B, and C at the same time. The total tool movement is a distance, X, at all three points. However, at point B (the tool center), X coincides with a radial path across the wall (true notch depth), whereas at points A and C (the tool corners) X is measured on a line which is at an angle, θ, with the radial path. Therefore, if the actual notch depth, d, is to be held constant (same as point B), an additional cut, Y, at points A and C would have to be made ($d \cong [x + y] \cos \theta$). For this reason the tool must be reshaped to a smaller diameter than the tube outer diameter for outer-surface notches. This provides more cutting at the tool edges than at the center. For inner-surface notches a diameter larger than the inner diameter is used for preshaping. With this system we can fabricate both inner- and outer-surface transverse notches with average depths ±10% of nominal values. Studies will be made to improve accuracy and precision.

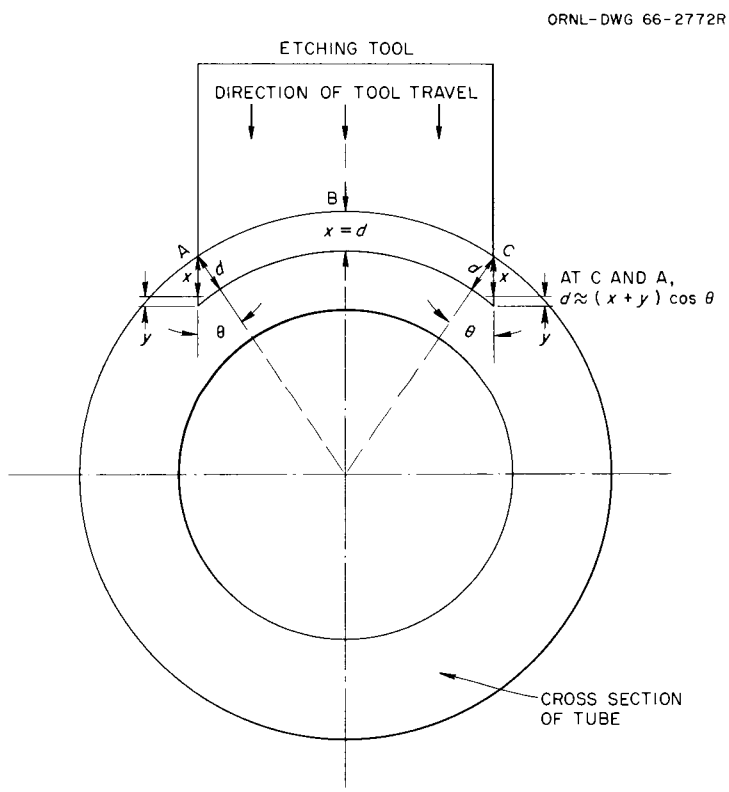

Fig. 3.1. Geometric Relationships for Preshaping Tools for Electro-Discharge Machining of a Transverse Notch in the Outer Surface of a Tube.

[redacted]

4. ZIRCONIUM METALLURGY

M. L. Picklesimer

We are conducting research along several lines on zirconium-base alloys of potential use as structural materials for water-cooled and/or -moderated reactor systems. The principal projects are: (1) studies of the physical metallurgy, including transformation kinetics and morphologies, mechanical properties, phase diagrams, and heat-treatment response; (2) the development, evaluation, and utilization of preferred orientation and strain anisotropy in α-zirconium alloys during fabrication, and the utilization of yield stress anisotropy in increasing maximum permissible design stresses in structures; (3) the determination of the effects of composition, temperature, and environment on the oxidation-corrosion rates in the thin film stage of oxide growth; (4) a study of the effects of alloy composition and oxidation environment on the structural properties of thin oxide films *in situ*; and (5) investigation of stress orientation of hydrides in Zircaloy-2.

Anisotropy in Zircaloy-2 and Zircaloy-4

P. L. Rittenhouse M. L. Picklesimer

Zircaloy Tubing

Two lots of Zircaloy-4 and four lots of Zircaloy-2 tubing have been received from commercial vendors. Some data were presented in the previous report.[1] The preferred orientations of all six lots of tubing were determined by the Knoop microhardness technique.[2] The "average" basal pole figures determined for two of the materials are presented in Fig. 4.1. In "C" material, the majority of the basal poles of the

[1]P. L. Rittenhouse and M. L. Picklesimer, *Fuels and Materials Development Program Quart. Progr. Rept. Dec. 31, 1965*, ORNL-TM-1400, pp. 43–45.

[2]P. L. Rittenhouse and M. L. Picklesimer, "Comparison of Pole Figure Data Obtained by X-Ray Diffraction and Microhardness Measurements on Zircaloy-2," accepted for publication in the *Transactions of the Metallurgical Society of AIME*.

ORNL-DWG 66-3421

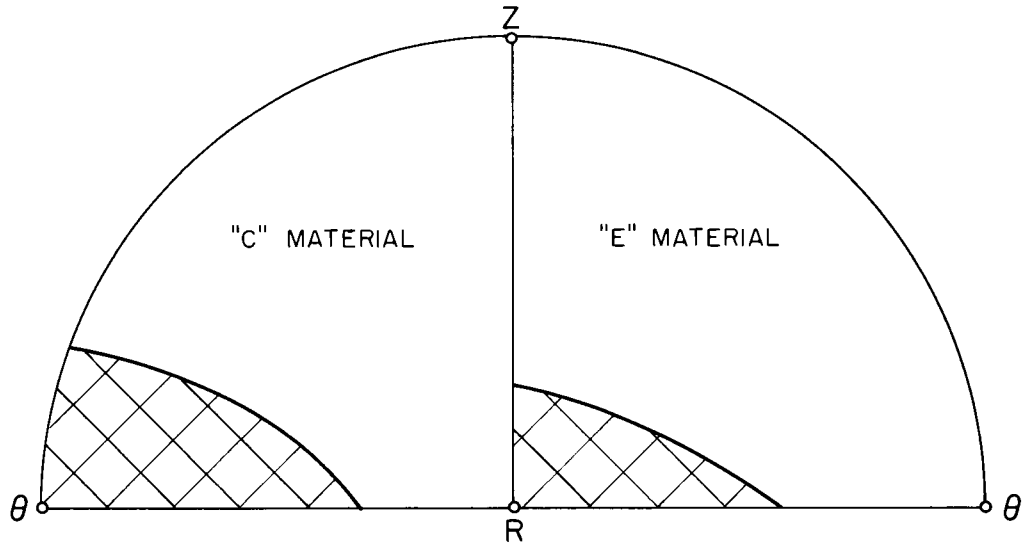

Fig. 4.1. Basal Pole Figures for Zircaloy Materials "C" and "E" Determined by Knoop Microhardness Technique.

texture are nearly parallel to the tangential direction, θ, of the tubing, and in material "E" they are nearly parallel to the radial direction, R. The textures of the other four lots of tubing are described in Table 4.1.

Table 4.1. Zircaloy Tubing Texture and Property Data

Material Code	Material Description	Basal Pole Distribution	Axial (Z) Direction Yield Strength (psi)	
			Tension	Compression
			$\times 10^3$	$\times 10^3$
A	3/4-in.-OD Zircaloy-2	$R \cong \theta \ggg Z$	61.0	71.0
B	1/2-in.-OD Zircaloy-2	$R \cong \theta \ggg Z$	56.5	61.0
C	3/4-in.-OD Zircaloy-2	$\theta > R \ggg Z$	51.0	54.2
D	1/2-in.-OD Zircaloy-2	$R \gg \theta \ggg Z$	49.0	64.3
E	3/4-in.-OD Zircaloy-4	$R \gg \theta \ggg Z$	56.6	67.7
F	1/2-in.-OD Zircaloy-4	$R \cong \theta \ggg Z$	60.0	65.0

Axial tension and compression tests of the six lots of tubing were made and the results are presented in Table 4.1. The correlation of yield strengths with texture must await more accurate and complete determinations of the textures present. The compression yield strengths for all but material "A" were obtained on short-section specimens. These specimens, 3/4 in. long, were first tested to determine if they could give yield strength data comparable to those determined on full-size tube specimens. Five short specimens of material "A" had an average yield strength of 70,700 ± 500 psi compared to a value of 71,000 psi for full-size specimens. The use of the short specimens for axial compression tests produces results at least as good as those of full-size tubes and decreases by at least a factor of 10 the amount of time and material required for the test. Torsion tests on these materials are presently in progress and tests combined with internal pressure will be conducted shortly.

Determination of Yield Surfaces

A method of obtaining flow curves in stress space using the anisotropy of Knoop microhardness measurements on zirconium alloys was described in a recent paper by Wheeler and Ireland.[3] The curve determined is the cross section of the flow surface on the octahedral plane of stress space. The analysis of the method presented by Wheeler and Ireland is based on the idea that the Knoop indenter produces deviatoric shear stresses. These shear stresses can be related to flow strengths in particular directions in the material by proper orientation of the indenter on three orthogonal surfaces of the specimen of the material. The basis of the analysis is not clear, although the fit with experimental data is surprisingly good. We developed an explanation which we believe places it on firmer grounds and also allows it to be extended to produce more information on the cross-sectional shape of the flow surface.

---

[3]R. G. Wheeler and D. R. Ireland, "Multiaxial Plastic Flow of Zircaloy-2 Determined from Hardness Data," paper presented at the Symposium on Zirconium and Its Alloys, 1965 Fall Meeting of the Electrochemical Society, Buffalo, New York, October 10–14, 1965.

The Knoop microhardness indenter has an asymmetric shape consisting of four flat facets whose intersections make included angles of 130° 0' and 172° 30'. The impression formed in the test material by the indenter is in the shape of a shallow, elongated pyramid having a depth of about one-thirtieth of the long diagonal of the base and a diamond-shaped base with a long-to-short diagonal ratio of 7.11.

Plastic flow occurring under the Knoop indenter as the hardness impression is made can be examined by the analysis of wedge indentation developed by Hill, Lee, and Tupper.[4] From this analysis, the forces causing plastic flow can be resolved into a hydrostatic compressive force and a set of shear stresses lying in a family of planes at 45° to the normal of the wedge face and parallel to the long edge of the wedge. The conditions are those of plane strain and the cross section of the family of planes forms the "slip-line field." Along the "slip line," which goes through the leading edge of the wedge, the material suddenly goes from an elastic-strain state to a plastic-strain state. This is equivalent to the shear condition operating in a uniaxially loaded compression specimen at the yield point. Since the hardness (resistance to indentation) is related to the shear stress along this "slip line," the hardness can be related to the yield strength. In this analysis, the yield strength in tension is assumed to be the same as that in compression. Thus, the shear stress, K, along this slip line can be equated to the tensile yield strength by the relation, $K = YS_t/2$, if Mohr's criterion of plastic flow is assumed to hold, or by $K = YS_t/\sqrt{3}$ if von Mises' criterion is assumed.

Since we know that in Zircaloy-2 the yield strength in tension can be very much different from that in compression along the same test axis, the yield strength to which the shear stresses (and the hardness) must be related is then that in compression.

Wheeler and Ireland[3] have analyzed the stresses produced in the indenter in terms of a hydrostatic compressive stress that produces no

---

[4]R. Hill, E. H. Lee, and S. J. Tupper, Proc. Roy. Soc. (London), Ser. A 188, 273–90 (1947).

flow and a deviative shear stress along the same family of planes as those of the "slip-line field" of Hill, Lee, and Tupper.[4] So far as we can determine, the two shear stresses are the same.

The problem now becomes one of relating these "deviatoric shear stresses" (i.e., hardnesses) to the yield behavior in three-dimensional stress space. To accomplish this, we must first be able to transform the hardness data obtained on three orthogonal surfaces of the test specimen to the deviatoric shear stress-yield locus on the octahedral plane of three-dimensional stress space. We must then transform these data into the cross section of the yield surface and transform that, in turn, into the biaxial yield loci on the appropriate biaxial stress planes of that three-dimensional stress space.

Consider a three-dimensional geometric space having orthogonal axes of Z, R, and θ. If tubing material is being studied, these axes are in the axial, radial, and tangential directions, respectively. If sheet or plate material is being used, these axes are the rolling, normal, and transverse directions, respectively. Let the Knoop microhardness impression be made on the (Z, θ) plane with the long diagonal of the indenter in the θ direction. The traces of the four facets of the indenter are shown on the stereographic projection of Fig. 4.2 as traces 1, 2, 3, and 4. The normals to the facets are shown as the points N_1, N_2, N_3, and N_4. The direction of the deviatoric shear stress. lying in the shear plane at 45° to the indenter facet is shown as point "a" for facet 4, transposed for convenience from the lower to the upper surface of the stereographic sphere. The deviatoric shear direction for facet 3 is given as point "b." The magnitude of the shear stress, τ, is unknown but the ratio of its components along the Z and θ axes can be determined. This ratio is given by the ratio of the cosines of the angle ϕ and ψ as defined in Fig. 4.2. The magnitude of the deviatoric shear stress is proportional to the hardness number for that indenter orientation but the proportionality constant is not known.

Next consider a three-dimensional stress space having orthogonal axes of σ_Z, σ_R, and σ_θ. A biaxial yield locus can be produced on each of the planes (σ_Z, σ_θ), (σ_θ, σ_R), and (σ_R, σ_θ) by appropriate experimental testing techniques. These yield loci define intersections between the

[redacted]

ORNL-DWG 66-3418

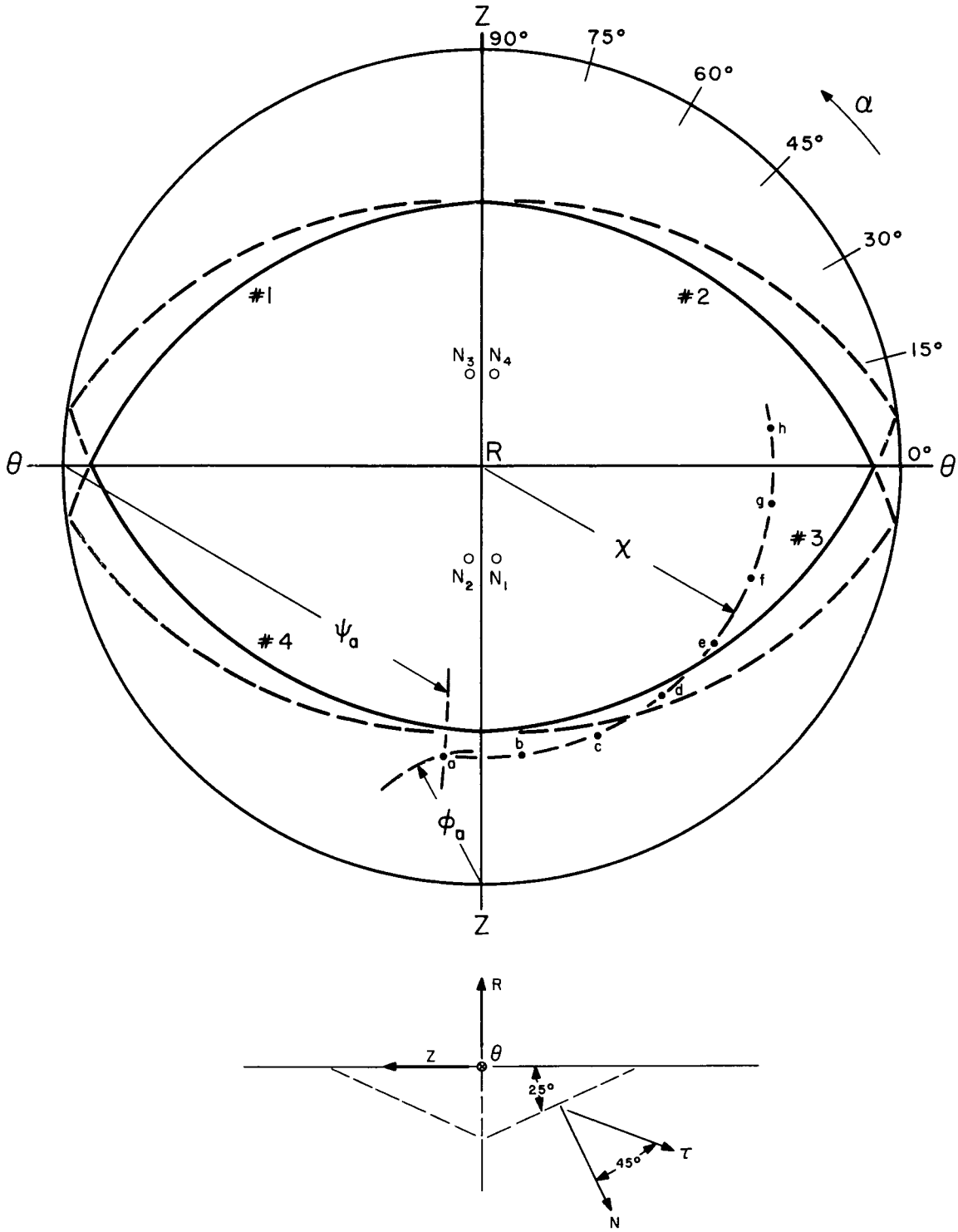

Fig. 4.2. Stereographic Projection Showing Knoop Indenter Facet Traces and Normals and the Associated Deviatoric Shear Stresses.

[redacted]

planes and the yield surface in stress space, and, therefore, a trace or cross section of the yield surface on the octahedral plane which satisfies the deviatoric stress equation

$$S_Z + S_\theta + S_R = C_1 = \text{a constant} \quad . \tag{1}$$

The deviatoric stress S_i is defined by

$$S_i = \sigma_i - \sigma_o \quad , \qquad i = Z, \theta, R \quad , \tag{2}$$

and

$$\sigma_o = \frac{\sigma_Z + \sigma_\theta + \sigma_R}{3} = \text{hydrostatic component} \quad . \tag{3}$$

It is assumed that the hydrostatic component does not affect the <u>cross-sectional shape</u> of the three-dimensional yield surface (although the <u>size</u> may be affected).

For hardness data taken on the (Z, θ) plane, S_R is constant for any angle α between the long diagonal of the indenter and the θ direction (see Fig. 4.2), that is Eq. (1) becomes

$$S_Z + S_\theta = C_2 = C_1 - S_R \quad . \tag{4}$$

The ratio S_Z/S_θ varies with α, and as stated previously, is proportional to the ratio of the cosines of the angles ϕ and ψ as defined in Fig. 4.2. The ratios S_Z/S_R and S_θ/S_R are similarly determined. The values of these ratios as functions of the angle of indenter rotation, α, are given in Table 4.2.

Table 4.2. ϕ, ψ, S_Z/S_θ, and σ_Z/σ_θ for Knoop Microhardness Measurements in the (Z, θ) Plane

α (deg)	Stress Directions	ϕ (deg)	ψ (deg)	S_Z/S_θ	σ_Z/σ_θ
0	a, b	22, 22	82, 82	6.66	1.65
15	b, c	22, 30	82, 69	3.58	1.46
30	c, d	30, 42	69, 55	1.72	1.19
45	d, e	42, 55	55, 42	1.00	1.00
60	e, f	55, 69	42, 30	0.58	0.84
75	f, g	69, 82	30, 22	0.28	0.69
90	g, h	82, 82	22, 22	0.15	0.61

With the indenter again in the (Z, θ) plane, $\sigma_R = 0$, and

$$S_Z = (2\ \sigma_Z - \sigma_\theta)/3 \quad , \tag{5}$$

$$S_\theta = (2\ \sigma_\theta - \sigma_Z)/3 \quad , \tag{6}$$

and

$$\sigma_Z/\sigma_\theta = \frac{1 + 2(S_Z/S_\theta)}{2 + (S_Z/S_\theta)} \quad . \tag{7}$$

The ratios of the stresses now permit determination of the positions of the lines in the octahedral plane, Eq. (1), along which the ratios of of the deviatoric shear stresses produced by the indenter and those produced by multiaxial stress are the same. It is along these lines that the appropriate hardness numbers may be plotted to define the cross-sectional shape of the three-dimensional yield surface. The stress ratios are given in Table 4.2 and plotted in Fig. 4.3 on the octahedral plane of stress space.

The next problem to be resolved is that of the scaling of the hardness numbers on the octahedral plane of stress space so that the cross-sectional shape of the yield surface can be defined. On the (Z, θ) plane of geometric space, Fig. 4.2, the hardness will scale radially on concentric circles having the R axis as a common center.

[redacted]

ORNL-DWG 66-3419

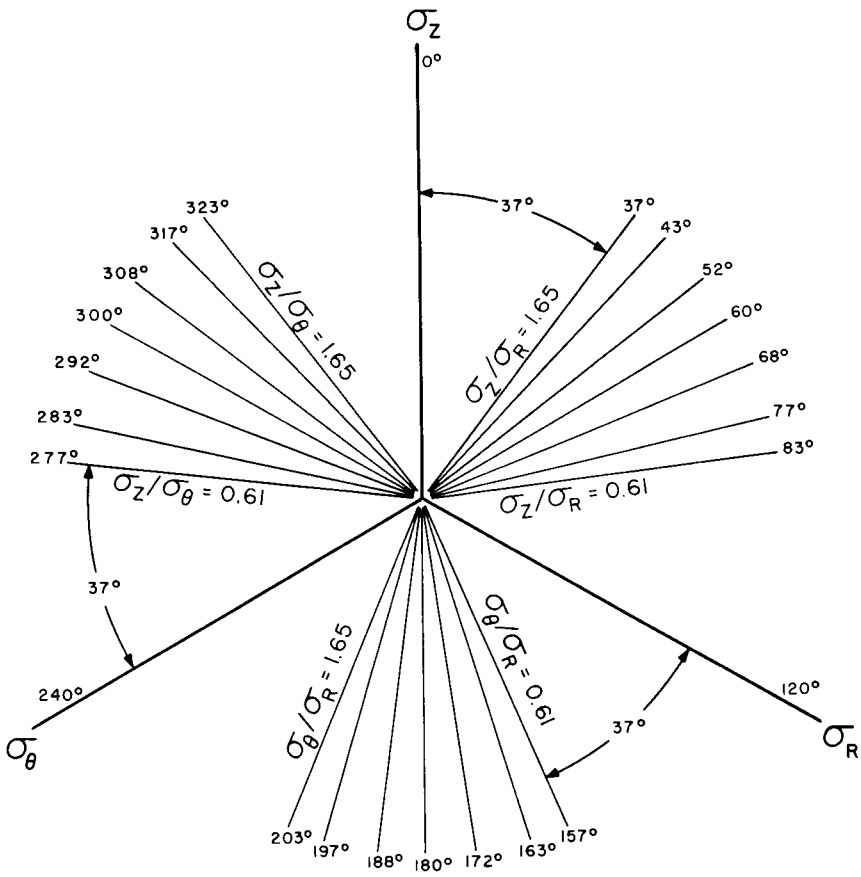

Fig. 4.3. Stress Ratio Lines on the Plane $S_Z + S_\theta + S_R = C_1$ on which the Knoop Microhardness Data are Plotted.

In this case, the hardnesses would be directly proportional to the compressive yield strengths for each of the indenter orientations. This polar hardness scale projects on the octahedral plane of stress space, Fig. 4.4, as a set of concentric ellipses having an axial ratio of $\sqrt{2}$ with the minor axes parallel to the R axis. Only the portion of the ellipses lying between the σ_Z and σ_θ axes and intersecting the σ_Z/σ_θ ratio lines has any physical meaning on this projection. A circle having its radius equal to the semiminor axis of one of the ellipses is drawn in Fig. 4.4. Within the limits of the stress ratio lines of the figure, the use of a circular scale of hardness rather than an

[redacted]

[redacted]

ORNL-DWG 66-3417

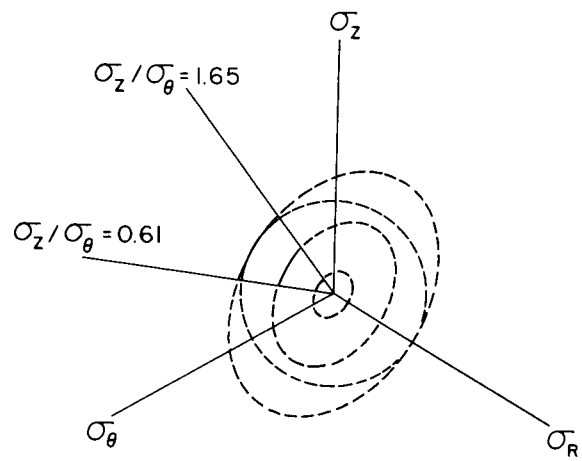

Fig. 4.4. Projection of Polar Hardness Scale onto the Octahedral Plane.

elliptical scale causes no more than 3% error in the location of any of the hardness points. This error is well within that for the hardness determination alone, and so can be neglected. Thus, all hardness scales on the octahedral plane of stress space will henceforth be considered to be circular, since this is much easier to use.

In order to predict biaxial stress properties, we must project the cross section of the yield surface obtained on the octahedral plane to each of the three biaxial stress planes and scale it to read in yield stresses. In the absence of evidence to the contrary, we assume that the hydrostatic component of the multiaxial stress does not change the shape of the cross section of the yield surface though it may change the size (but not necessarily). This is a less stringent requirement than that for the case in the yield theory of isotropic materials. In both cases, it must also be assumed that the axis of the yield surface makes equal angles with all three reference axes and that the three-dimensional shape of the yield surface is topologically a cylinder. These assumptions then allow the cross-sectional shape of the yield surface to be projected by lines parallel to the axis of the surface onto a biaxial stress plane to define the shape of the yield locus on

[redacted]

that plane. The intersection of the yield locus with one of the compression axes in the biaxial stress plane is equated to the experimentally determined compressive yield strength on that axis. This then establishes the scale of stresses on that plane.

A typical determination of the cross-sectional shape of the yield surface and its projection onto one of the biaxial stress planes is demonstrated in Figs. 4.5a and b. The fit with the limited experimental data presently available is excellent.

Correction of Knoop Microhardness Measurements for Anisotropic Recovery

The design of the Knoop microhardness indenter was based on the assumption that little recovery occurs in the direction of the long diagonal of the impression on removal of the indenter while the major recovery occurs in the direction of the short diagonal. Thus, the projected area of the indenter that supports the load at the time the indenter is in place could be calculated with small error from a measurement of the long diagonal of the impression. That this assumption is not true even in isotropic materials can be readily shown by determining the ratio of long-to-short diagonals for hardness impressions made on a number of materials. Measurements on hardness calibration blocks of steels (KHN from 300 to 800) show the diagonal ratio to be between 6.7 and 6.8 in comparison to an indenter ratio of 7.11. If the assumption were true, these ratios would all be greater than 7.11, not less. Similar measurements have been made on copper, brass, and aluminum alloys and the ratios have ranged from 6.5 to 6.8. In Zircaloy-2 single crystals, the values of this ratio have ranged between 5.2 and 7.6, depending on the relative orientations of the indenter and the "c" axis of the specimen.

A calculation of the projected area of the indenter from a measurement of the length of the short diagonal of the impression should be just as valid as that from the long diagonal. If there were no recovery of the impression, the KHN calculated from the short diagonal measurement would be the same as that from the long diagonal. If there were appreciable recovery in the direction of the long diagonal, the KHN calculated

[redacted]

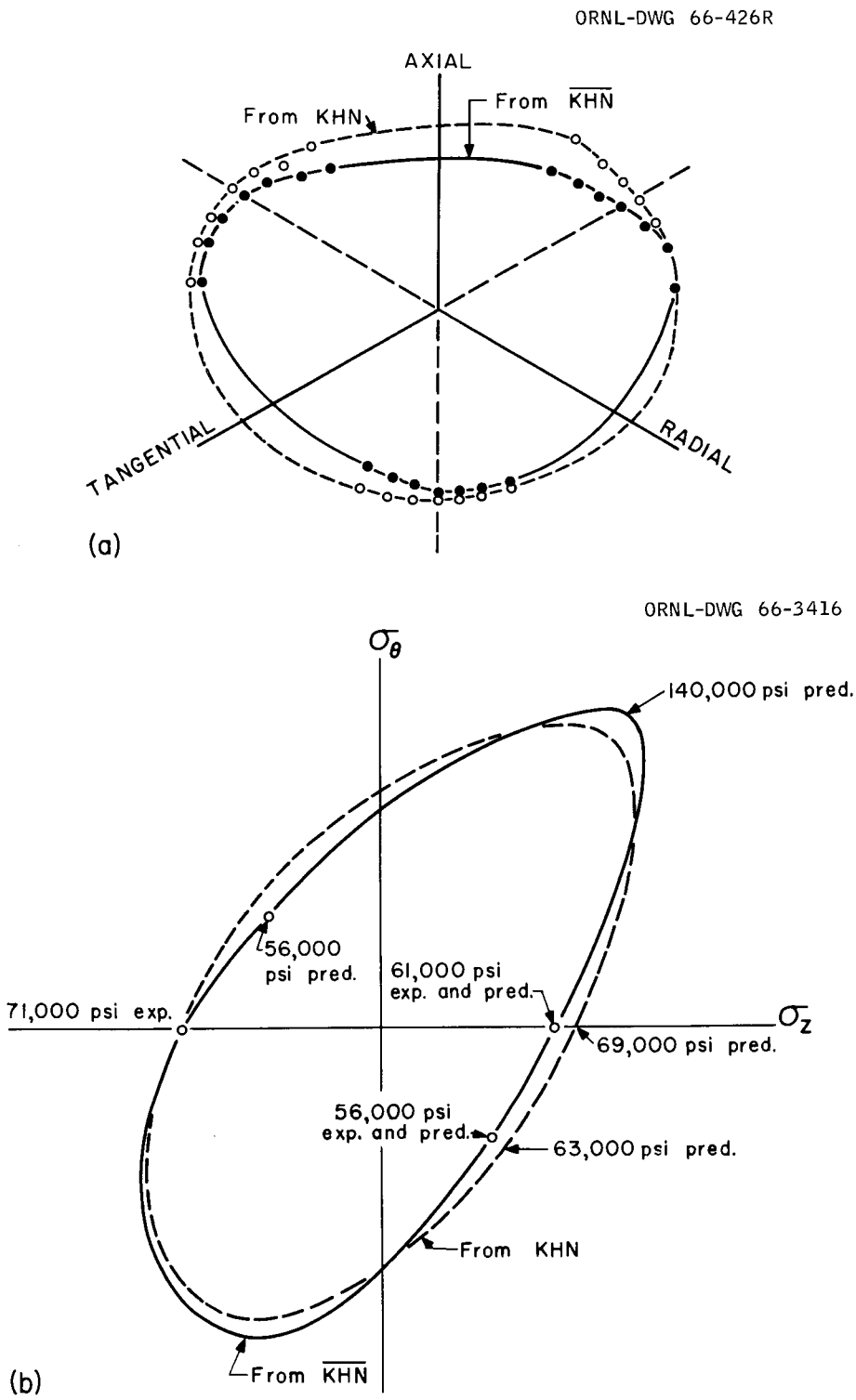

Fig. 4.5. Cross-Sectional Shape of the Yield Surface and Its Projection onto the Biaxial Stress Plane. (a) Yield surface traces for Zircaloy-2 tubing "A" material. (b) Biaxial yield stress figures derived from yield surface traces.

[redacted]

from it would be too high (i.e., too hard). If the diagonal ratio were also less than 7.11, the KHN calculated from the short diagonal would be less than that from the long diagonal, and both will be greater than the true hardness of the materials (i.e., than if no recovery occurred in either direction). Thus, the lower KHN is a better measure of the true hardness.

The standard tables of KHN vs length of the long diagonal can be used to calculate the KHN from the short diagonal measurement by the following equation, if the diagonal ratio is determined:

$$KHN_{SD} = KHN_{LD}\ [(LD/SD)/7.11]\ . \qquad (8)$$

Since the lower KHN is closer to the true hardness (if no recovery occurs), corrections are not made if the ratio LD/SD is equal to or greater than 7.11. Henceforth, the symbol $\overline{KHN}$ will be used to indicate that the hardness has been calculated from a measurement of the short diagonal if the diagonal ratio was less than 7.11, and from the long diagonal if it was equal to or greater than 7.11. Thus, $\overline{KHN}$ means that the hardness measurements have been corrected for anisotropic recovery as much as possible.

The yield surface traces determined from corrected and uncorrected hardness data for one lot of 3/4-in.-OD Zircaloy-2 tubing ("A" material) are shown in Fig. 4.5a. The biaxial yield figures on the (σ_Z, σ_θ) plane projected from these yield surface traces are shown in Fig. 4.5b and compared to the yield values found experimentally for this material. As can be seen, the fit of experimental data with the projected yield figure is much better when hardnesses corrected for diagonal ratios ($\overline{KHN}$) are used. This conclusion holds for every lot of Zircaloy-2 so far examined.

Yield and Flow in Uniaxial Tension and Compression

When working with anisotropic materials, it is imperative that the anisotropy of properties be determined in three-dimensional space. For the anisotropy of mechanical properties, it would be quite advantageous

to be able to characterize the anisotropies of strength and plastic flow in a given material in tension and compression from the results of a single, simple uniaxial test. This uniaxial characterization[5] requires the specification of 12 strain anisotropy constants (k's), only 4 of which are independent, and 6 uniaxial yield strengths, 3 in tension and 3 in compression. The correlation previously proposed[5] between the strain anisotropy constants (k's) in tension and compression has been proven by the examination of the data from eight lots of Zircaloy-2 having widely varying textures. This correlation now reduces the number of independent k values from four to two. Thus, values of k_{ij} and k_{jk}, for example, allow determination of the other 10 values (4 in tension, 6 in compression).

The yield strengths and k values in both tension and compression have been determined experimentally for eight lots of Zircaloy-2 of known and widely varying textures. Using these data, empirical relationships were established between the various k values, yield strengths, and yield strength ratios. It is now possible, through these empirical relationships, to obtain all of the strain constants (k's) and yield strengths required to characterize the uniaxial anisotropy of a material from a single uniaxial tension or compression test.

The empirical relationships are shown in the curves of Figs. 4.6–4.9. The use of the relationships is illustrated by the following example. A uniaxial compression test is made on a specimen having the compression axis along the rolling direction of a plate material. The compression yield strength (CYS_{RD}) is determined, and the bulged cross section of the specimen is measured to determine the two values of k, (k_{-xy} and k_{-xz}) pertinent to it. The value of the compression yield strength (CYS_{ND}) in the normal direction is found from Fig. 4.6, a plot of CYS_{ND} vs k_{-xy}. The value of the compression yield strength in the transverse direction (CYS_{TD}) is calculated from the ratio of compression yield strengths

[5]P. L. Rittenhouse and M. L. Picklesimer, Fuels and Materials Development Program Quart. Progr. Rept. Sept. 30, 1965, ORNL-TM-1270, pp. 28–32.

[redacted]

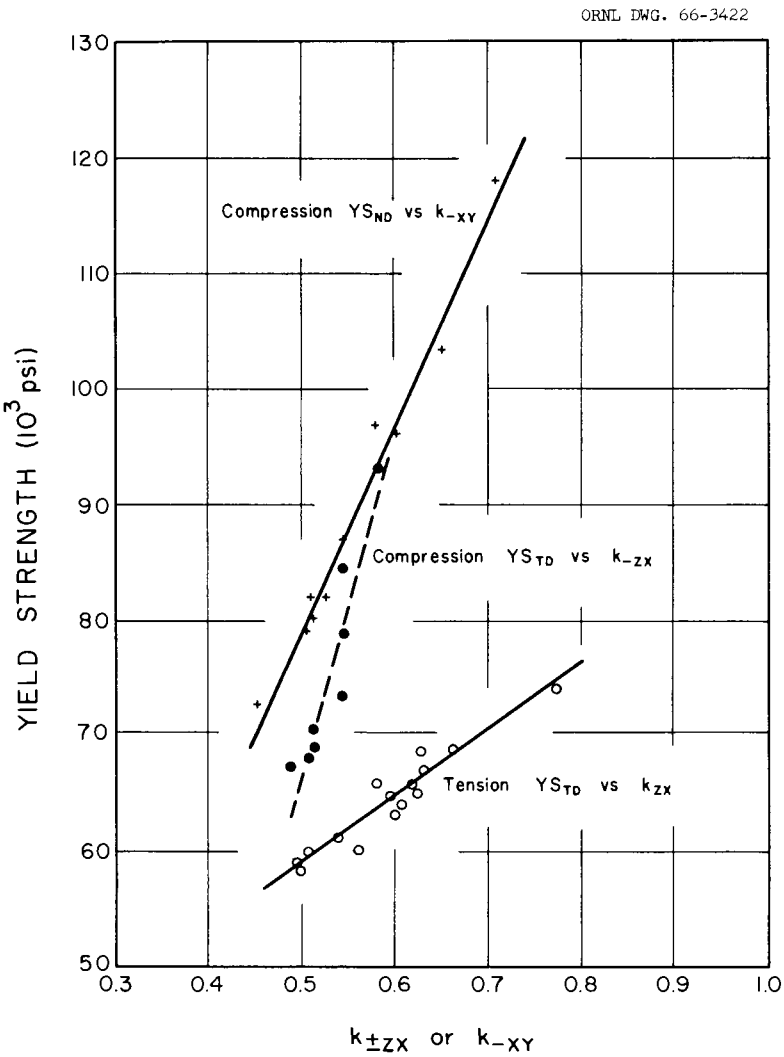

Fig. 4.6. Yield Strengths in Tension and Compression as Functions of the Strain Anisotropy Constants in Zircaloy-2.

obtained from Fig. 4.7, after the appropriate ratio of k values is determined; or it may be calculated from the equation of the line in Fig. 4.7, with the appropriate subscripts; that is,

$$CYS_{TD}/CYS_{ND} = 0.88\ (k_{-xz}/k_{-xy}) + 0.19 \quad . \tag{9}$$

Then, k_{-zx} is determined from the curve of CYS_{TD} vs k_{-zx} of Fig. 4.6.

At this point, the compression yield strength in the rolling direction and k_{-xy} and k_{-xz} have been experimentally determined, and the

[redacted]

[redacted]

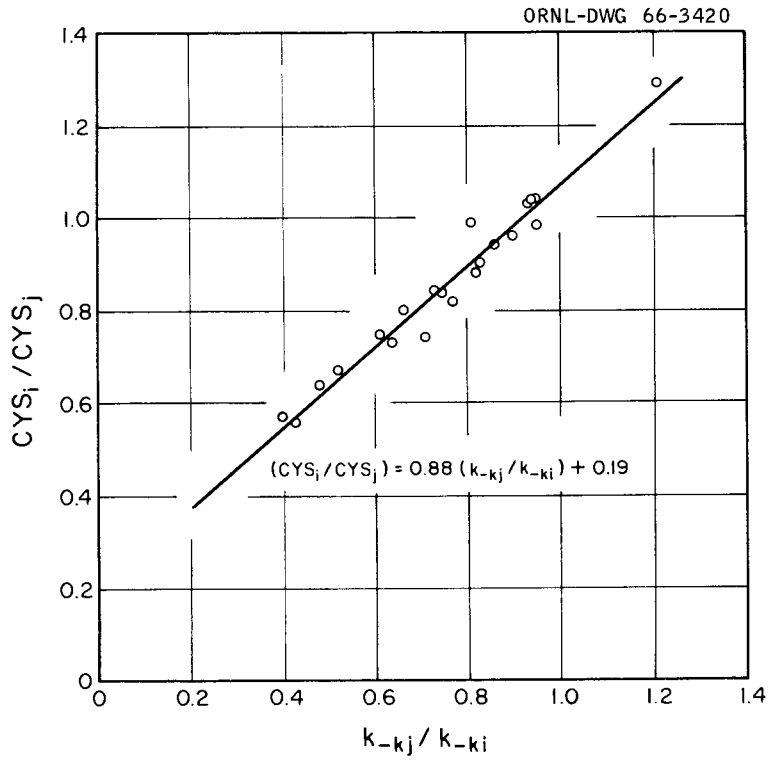

Fig. 4.7. Ratios of Compression Yield Strengths as Functions of Ratios of Strain Anisotropy Constants in Zircaloy-2.

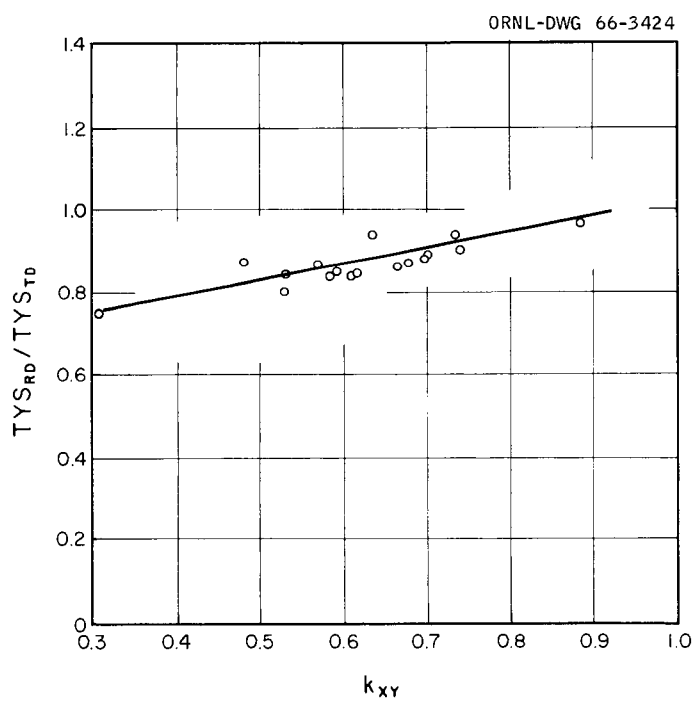

Fig. 4.8. Ratio of Tensile Yield Strength in Rolling to Transverse Directions as a Function of the Strain Anisotropy Constant in Zircaloy-2.

[redacted]

[redacted]

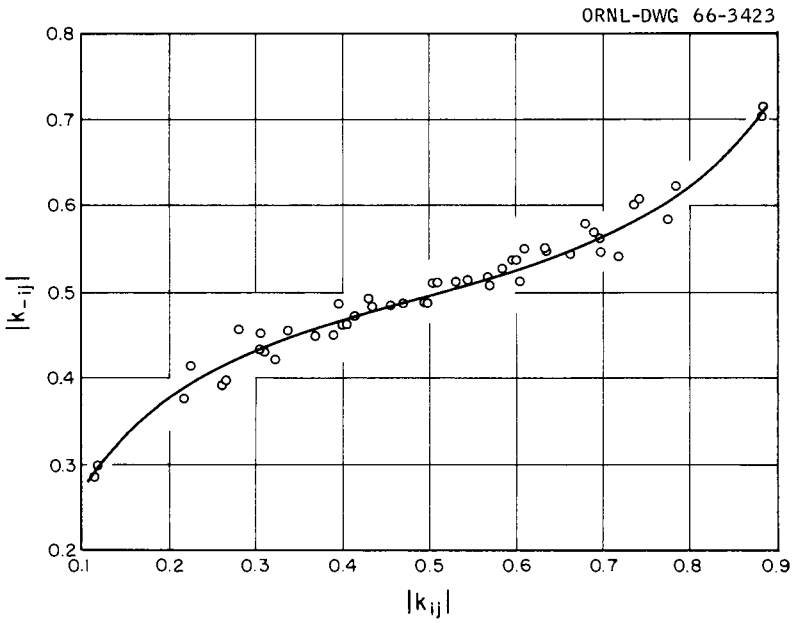

Fig. 4.9. Relationship of Strain Anisotropy Constants in Tension to Those in Compression in Zircaloy-2.

compression yield strengths in the transverse and normal directions and k_{-zx} have been calculated from the empirical curves.

Now, k_{-zy} is calculated from the relationship[5]

$$k_{\pm ij} + k_{\pm ik} = -1; \; i,j,k = x,y,z \quad . \tag{10}$$

The simultaneous solution of Eq. (10) and the equation relating all of the strain anisotropy constants,[5]

$$\frac{k_{\pm xy}}{k_{\pm xz}} \cdot \frac{k_{\pm yz}}{k_{\pm yx}} \cdot \frac{k_{\pm zx}}{k_{\pm zy}} = 1 \tag{11}$$

yields a value for k_{-yx}; that is,

$$k_{-yx} = \frac{k_{-xy} \cdot k_{-zx}}{k_{-xz} \cdot k_{-zy} + k_{-xy} \cdot k_{-zx}} \quad .$$

Then k_{-yz} is calculated by Eq. (10).

[redacted]

[redacted]

The empirical correlation previously established between the values of k in tension and those in compression,[4] shown in Fig. 4.9, now allows the determination of all the k values in tension (i.e., k_{+ij}, k_{+jk}, etc.). Once the k values in tension are determined, the yield strengths in tension in the rolling and transverse direction can be found from the curves of Figs. 4.6 and 4.8. The tensile yield strength in the normal direction can be approximated from the curve of Fig. 4.8 by substituting TYS_{ND} for TYS_{TD} and k_{xz} for k_{xy}. We have no direct experimental data to validate the approximation of TYS_{ND}, but comparison of yield strengths in tension and compression in the transverse direction as functions of texture indicate that the approximation should be reasonable.

This same information can be obtained if the starting data are the yield strength and k values for a single tensile specimen. We obtained a cross-check on the accuracy of the empirical correlations and the calculation of the various values from them. Starting with the yield and k data for one tensile or one compression specimen for each of the eight lots of Zircaloy-2, all of the yield strengths and k values for all eight lots have been calculated from the curves of the empirical relationships established. In every case, the calculated values have agreed with the experimental values to within 5%. The testing of the empirical correlation will continue as new experimental data can be obtained.

Studies of Zirconium Alloys in Shear

D. O. Hobson M. L. Picklesimer

The rolling textures observed in zirconium and Zircaloy-2 cannot be adequately explained or analyzed if the only deformation systems operating are those reported in the literature, nor can the stability of the rolling texture to further rolling be explained.[6] These reported deformation systems were determined on single- or large-grained polycrystalline specimens tested in either uniaxial tension or uniaxial

---

[6]M. L. Picklesimer, "Deformation, Creep, and Fracture in Alpha-Zirconium Alloys," accepted for publication in Electrochemical Technology.

[redacted]

[redacted]

compression. Basal plane slip in zirconium was not reported until Reed-Hill observed the accommodation strains occurring during twinning in deformed polycrystalline zirconium.[7] If it is assumed that other deformation systems can be forced to operate in the complex stress situation existing in a polycrystalline specimen during deformation, then both the development and stability of the observed rolling textures can be satisfactorily analyzed. One set of deformation systems, involving $\langle 11\bar{2}3 \rangle$ slip directions on $(10\bar{1}0)$, $(10\bar{1}1)$, $(11\bar{2}1)$, and $(11\bar{2}2)$ planes satisfies all of the requirements of the analysis, permits cross slip and climb, and provides more than the five slip systems required to satisfy the continuity equations. These systems have not been experimentally observed in zirconium although a $\langle 11\bar{2}3 \rangle$ slip direction has been observed in zinc.

The movement of the texture of polycrystalline zirconium during straining in tension and compression has been cursorily examined in several studies. No study has been conducted on the behavior of the texture during straining by pure shear. Yet it is the behavior of the texture in pure shear that must be known if the shaping processes are to be designed to produce the specific strain paths necessary for texture control during commercial manufacture of mill products.

A program has been initiated to study the critical resolved shear stresses of all possible slip systems in zirconium as functions of alloying element and temperature. This will be accomplished by deforming in pure shear single-crystal specimens so aligned that the shear can occur only on a specific crystallographic plane in a specific crystallographic direction. A shear jig was built that causes a specimen 1/8 × 1/8 × 1/2 in. to be sheared under total restraint on two parallel planes 1/8 in. apart. Such total restraint is required if the specific strain path is to be realized. The more complete the restraint, the more precisely located will be the shear direction, and the thinner will be the shear zone. A photograph of the partially assembled shear jig is

---

[7]R. E. Reed-Hill, "Role of Deformation Twinning in the Plastic Deformation of a Polycrystalline Anisotropic Metal," pp. 295–320 in Deformation Twinning (ed. by R. E. Reed-Hill, J. P. Hirth, and H. C. Rogers), Gordon and Breach Science Publishers, New York, 1964.

[redacted]

presented in Fig. 4.10. The specimen is held in the square hole of the blade by the adjustable block under it. The blade is fitted into the long groove in the jig body with the specimen positioned in the transverse slot. The exposed surfaces of the specimens are restrained when the two L-shaped side plates are clamped in place. The specimen is sheared on two parallel planes by downward movement of the blade. The stress-strain curve is obtained by appropriate sensing devices when the compression jig is operated in a standard tensile testing machine.

The present work with the shear jig is concerned with the movement of the texture during shear deformation of polycrystalline specimens of zirconium having known textures. The behavior in two polycrystalline specimens of zirconium is shown in Fig. 4.11. One specimen was sheared approximately 5% of the specimen thickness; the other was sheared approximately 25% of the thickness. The crystallographic texture of both specimens was such that the basal poles of the undeformed specimens were concentrated in the normal direction to a high degree of intensity (i.e., the typical texture of rolled sheet zirconium, with the rolling direction of the sheet being in the shear direction of the specimen). In polarized light microscopy with a sensitive tint accessory plate, the

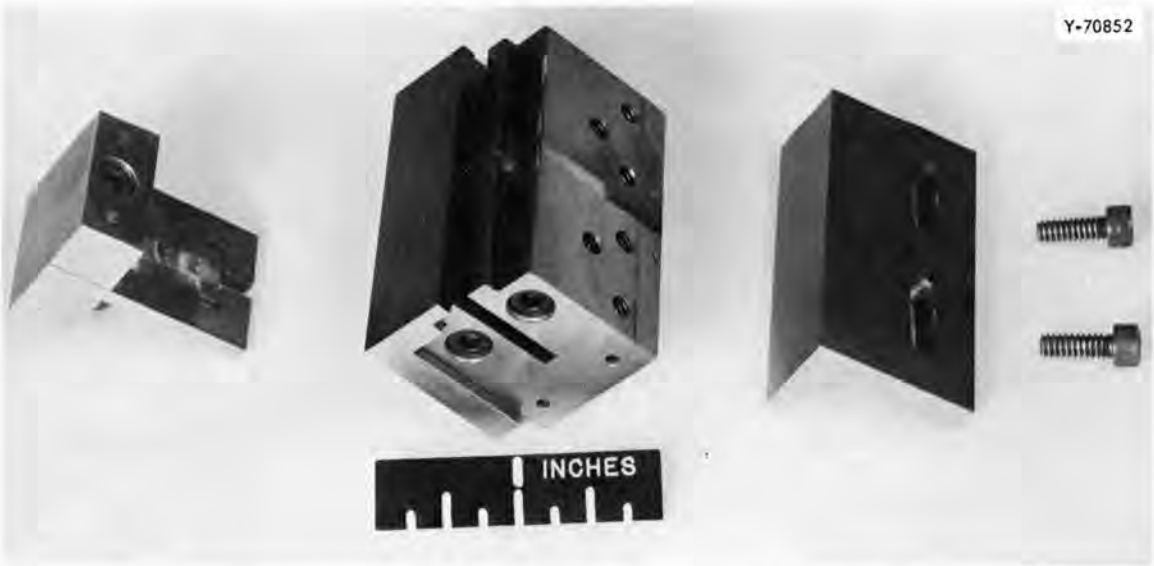

Fig. 4.10. Partially Assembled Shear Jig.

[redacted]

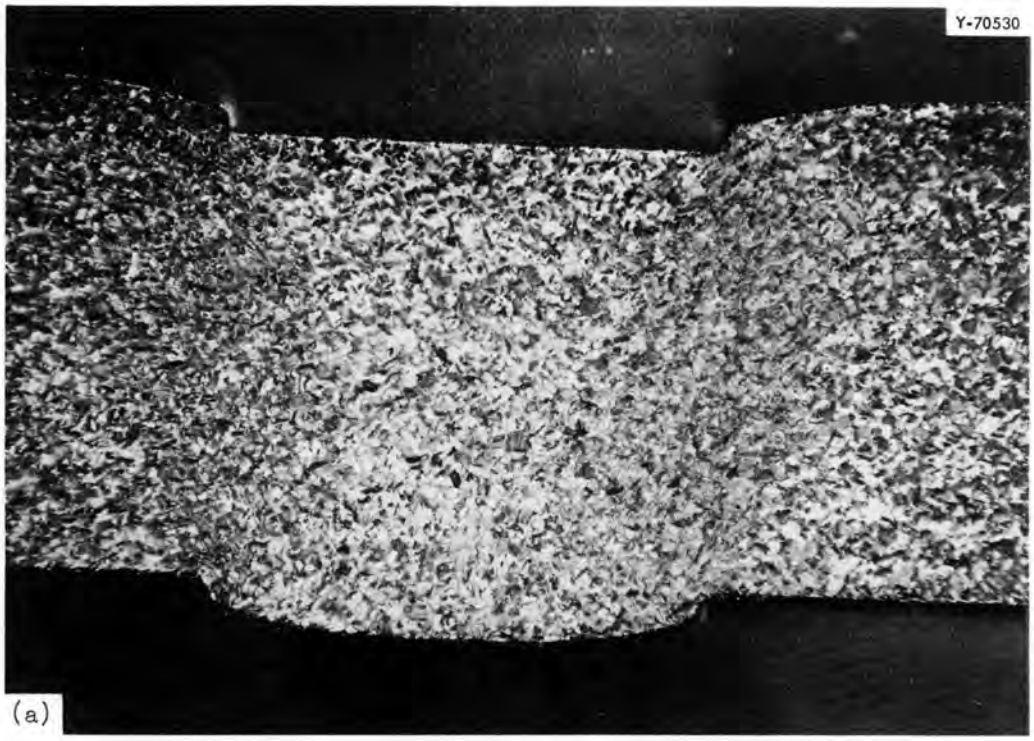

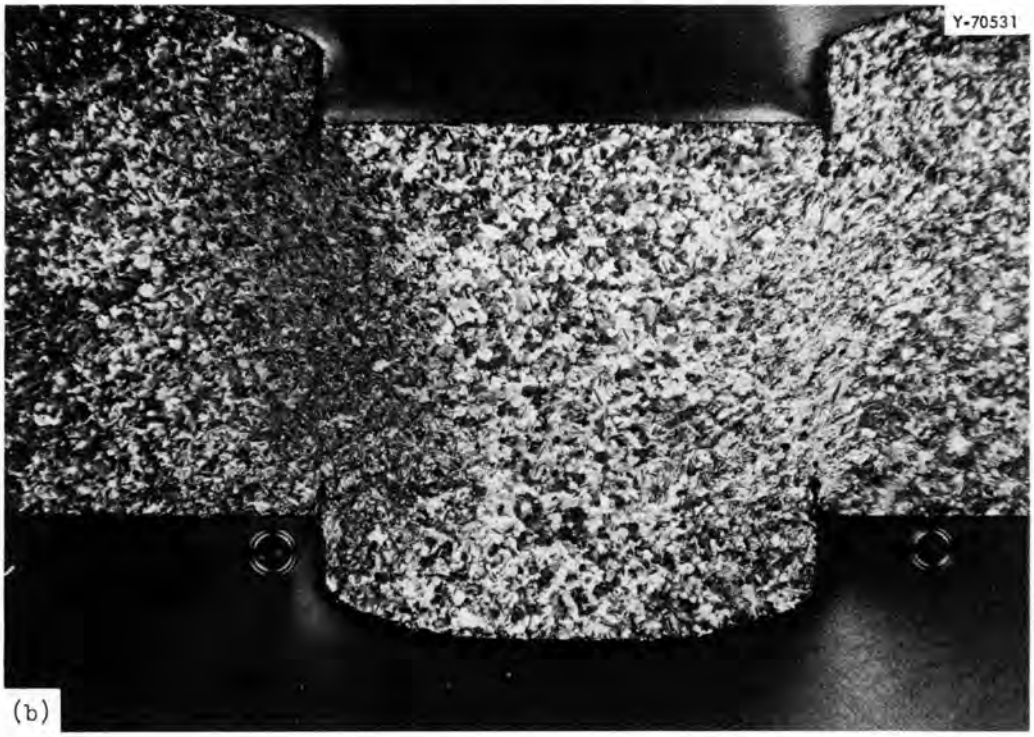

Fig. 4.11. Photomicrographs of Shear Specimens of Polycrystalline Zirconium. Note the development of strongly oriented deformed grains in the shear zone. Polarized Light. 25×. (a) Sheared approximately 5% of specimen thickness. (b) Sheared approximately 25% of specimen thickness.

[redacted]

equiaxed grains of the undeformed regions have an almost random distribution of red, blue, and purple colors. As the shear zone is approached, the colors of the deformed grains rapidly change to only small variations of shades of one predominant color. This indicates that, in the shear zone, all deformed grains have essentially the same basal pole orientation in space. The exact color observed depends on the orientation of the shear zone relative to the axes of the polarized light of the microscope (i.e., the color changes with stage rotation). The progress of the development of the shear texture can be approximated as a function of shear by comparison of the two photomicrographs. Measurement of the approximate basal pole orientation in space of the region of most shear deformation was accomplished by the polarized light technique reported previously.[8] The shear plane contained the normal and rolling directions and the shear direction was the rolling direction of the sheet. With these directions as reference axes, the average basal pole position can be described as being 65° from the rolling direction, 60° from the transverse direction, and 40° from the normal direction; and it is tilted in the direction of the shear. The tilts for the two shear planes are in the opposite sense when related to an outside reference system, but in the same sense when related to the shear planes from the center of the specimen. More orientation work must be performed before the crystallographic shear planes can be identified.

Polycrystalline specimens of known texture were sheared various amounts on shear planes variously oriented to the texture. Some of the specimens are being annealed to produce a relatively large grain size in the region of greatest shear. Crystallographic orientations will be determined in both as-sheared and sheared-and-annealed conditions. The orientations of grains receiving less deformation in the region of the shear zone will be examined. It is hoped that these examinations will show how the texture changes with shear plane and direction.

---

[8] L. T. Larson and M. L. Picklesimer, Fuels and Materials Development Program Quart. Progr. Rept. June 30, 1965, ORNL-TM-1200, pp. 36–39.

[redacted]

Single crystals of zirconium have been grown by the electron-beam zone-melting method by J. C. Wilson. Crystals of selected orientations will be cut to the shear specimen shape and size by an electrical-discharge machining apparatus presently under construction. The shear directions and planes of the specimens will be aligned with specific crystallographic directions and planes in the cutting operation. Analysis of the stereographic projection for zirconium has shown that a single family of planes, the $(11\bar{2}5)$, is perpendicular to the eleven families of planes that contain the $\langle 11\bar{2}3 \rangle$ slip direction. The cut and electropolished specimens will be anodized before shearing. The anodized coating is useful in enhancing the optical properties of the surface of the specimens for polarized light examination, and also acts as a brittle stress coat for analyzing the surface strain pattern of the specimen during shearing. After each specimen is examined optically, it will be sectioned for electron microscopy so that the Burgers vectors of the dislocations present can be determined.

Basal Pole Figures by Quantitative Polarized Light Microscopy

M. L. Picklesimer

The use of the measurement of one of the optical properties of α-zirconium, the angle of rotation, to determine the tilt of the basal pole of a grain from the normal to the specimen surface was reported previously.[8] A similar set of measurements are now being made for determining the same type of curves for Zircaloy-2 and Zircaloy-4.

The method discussed above can be used to determine a basal pole density figure (one type of quantitative basal pole figure) for zirconium if such measurements are made on 100 to 200 grains in a specimen. If the macrotexture is desired, the grains measured must be randomly selected over a large cross section of the specimen. If microtexture or texture gradient information is desired, the grains of selected regions must be examined in a pattern suitable to the problem. However, the technique is rather slow and laborious, since three goniometer readings (two stage angles and one analyzer angle) must be made visually and manually recorded for each grain.

[redacted]

A basal pole plotter was constructed which greatly speeds and eases the determination of a basal pole density figure. A polar chart recorder was coupled electrically to the stage and analyzer of the microscope. The stage of the microscope drives the rotation of the circular chart at a ratio of 1:1, and the analyzer rotation drives the recording pen radially from the center (zero rotation) to the circumference of the chart (maximum rotation of the analyzer). A remotely operated pen prints a point on the chart when the stage and analyzer are properly positioned for the basal pole position of each grain. In operation, the chart rotates as the microscope stage is rotated to bring the basal plane trace of the grain into correct alignment with the polarizer of the microscope. The microscope analyzer is then rotated to extinction, driving the recording pen from the center towards the circumference of the chart to indicate the basal pole tilt angle. The pen is then caused to print, leaving on the chart an inked point that shows the basal pole position for that particular grain relative to the selected reference axes. The procedure is repeated for every grain desired to count. The specimen is translated on the microscope stage in a pattern selected to best yield the specific texture information desired. The basal pole orientations of two or three grains can be determined in each minute. Thus, the basal pole positions of 200 grains can be determined in no more than 100 min. The polar chart records directly the basal plane trace angle and the angle of analyzer rotation. The true basal pole tilt for each grain must be determined from the specific optical property curve for that material and wavelength of light used in the measurement. Then, the number of basal poles per millisteradian must be counted and the data then plotted as a pole density, either in pole concentration units or as "times random." However, for most work, the texture determination can be handled entirely as recorded since it is relative textures and texture changes that are of interest. The complete conversion to quantitative pole density figures need be made only when absolute pole density plots are required.

The basal pole figure plotter with the microscope will be used to examine texture and texture gradients in the Zircaloy-2 and Zircaloy-4 tubing being used in the study of anisotropy in biaxial stress, the

change in texture of the polycrystalline shear specimens, and on Zircaloy-2 and Zircaloy-4 specimens prepared to study the development of texture gradients and texture banding in sheet, plate, and tubing. It will permit studies not previously possible by any other technique, since it can examine a texture grain by grain.

Oxide Film Studies

J. C. Banter

The vacuum system which will be used with the spectrophotometer[9] for the study of oxide films *in situ* as they are formed on or dissolved into zirconium alloy specimens was assembled and checked for leaks. When the system is leak-tight, runs will be made to develop the operational procedures for use of the system during the experimental work.

We continued to make measurements of the room temperature electrical conductivities (direct current) of oxide films on zirconium and have developed the following procedure to eliminate the problems previously encountered.[9] The specimens were masked with Scotch tape to expose a known free area of the oxide film. The specimen was then connected in series with an electrometer (ammeter operational mode) and an external direct-current power supply. One electrical contact was made directly to the substrate metal and the other contact made through a pool of mercury to the exposed oxide surface of the specimen. A known voltage of the order of 1 to 2 v was applied across the specimen. This voltage was always more than 100 times the full-scale input drop of the electrometer when it was operating in the ammeter mode. The film resistance was obtained by dividing the applied voltage by the current flow as read by the electrometer. The electrical conductivity was then calculated, using the exposed area of the film, the measured resistance, and the spectrophotometrically determined film thickness.

A series of specimens was anodized in a solution containing water, glycerine, lactic acid, citric acid, ethyl alcohol, and phosphoric acid

---

[9]J. C. Banter, Fuels and Materials Development Program Quart. Progr. Rept. Dec. 31, 1965, ORNL-TM-1400, p. 50.

to produce films of various thicknesses. The conductivities of these films were then determined as 2 to 3 $\times 10^{-15}$ ohm^{-1} cm^{-1} for the films thicker than 750 A. The conductivities increased progressively with decreasing film thickness up to approximately 2 $\times 10^{-14}$ ohm^{-1} cm^{-1} for a film 150 A thick.

The specimens were then annealed at temperatures from 400 to 575°C in a vacuum of less than 5 $\times 10^{-7}$ torr and the film conductivities remeasured. The vacuum annealing resulted in resistances of only 10 to 15 ohms and conductivities of the order of 10^{-6} ohm^{-1} cm^{-1} for all film thicknesses.

In contrast to these results, conductivities of anodic films formed in 1% KOH solutions have been reported[10] as high as 1.2 $\times 10^{-12}$ ohm^{-1} cm^{-1}. To compare the techniques, we anodized a series of specimens in 1% KOH to produce films of thicknesses comparable to those above and measured their conductivities. The conductivities observed for these films were relatively independent of thickness and were in the range of 1 $\times 10^{-14}$ ohm^{-1} cm^{-1} initially. However, over a period of 3 to 5 min, the conductivities dropped to a constant value in the range of 5 to 8 $\times 10^{-14}$ ohm^{-1} cm^{-1}. These results indicate that the films formed in 1% KOH do indeed have higher conductivities than those formed in the organic solution, but not as high as previously reported. On vacuum annealing, the KOH-formed films showed an increase in conductivity similar to that observed in those formed in the organic solution.

During the vacuum annealing operations, we noted that the films formed in the organic solutions dissolved into the zirconium base metal at a much slower rate than did those formed in 1% KOH. For example, thickness decreases of 50 and 710 A were found on vacuum annealing films formed in the organic solution and the KOH solution respectively at 450°C for 16 hr. Even greater differences in dissolution rates were observed at higher temperatures.

---

[10] D. K. Dawson and R. H. Creamer, Brit. J. Appl. Phys. 16, 1643 (1965).

The differences observed indicated that the two types of films were appreciably different in some unknown way. Smyth and co-workers[11] have suggested that oxide films formed on tantalum by anodizing in solutions containing phosphoric acid contain phosphorus in an outer layer of the oxide film that exhibits the low conductivity. Since the organic anodizing solution used on the zirconium specimens contains phosphoric acid, it was thought possible that these films also contained phosphorus. One of the anodized films was examined in transmission in the infrared spectrophotometer. The resulting absorption spectrum is shown, in part, in Fig. 4.12. The band at 413 μ is the first order interference minimum of the film (due to its thickness); that at 14.3 μ is attributed to absorption by ZrO_2. Miller and Wilkins[12] have recorded the absorption spectra of a number of inorganic phosphates, and all exhibit strong absorption between 9 and 10 μ. The unexplained absorption occurring at 9.2 μ in Fig. 4.12 is thus attributed to phosphate ion incorporated in the film.

The presence of phosphate ion in the oxide films on zirconium is believed, then, to impart greater electrical insulating character to the films as well as greatly decrease the rate of dissolution by the base metal at high temperatures. Since the oxidation of zirconium proceeds partially through the dissolution of the oxide in the base metal, it is possible that preanodizing zirconium to incorporate phosphate ion in the oxide films would be beneficial in limiting the corrosion of the metal at high temperatures.

---

[11] D. M. Smyth, T. B. Tripp, and G. A. Shirn, J. Electrochem. Soc. 113, 100 (1966).

[12] F. A. Miller and C. H. Wilkins, Anal. Chem. 24, 1253 (1952).

[redacted]

ORNL-DWG 66-3536

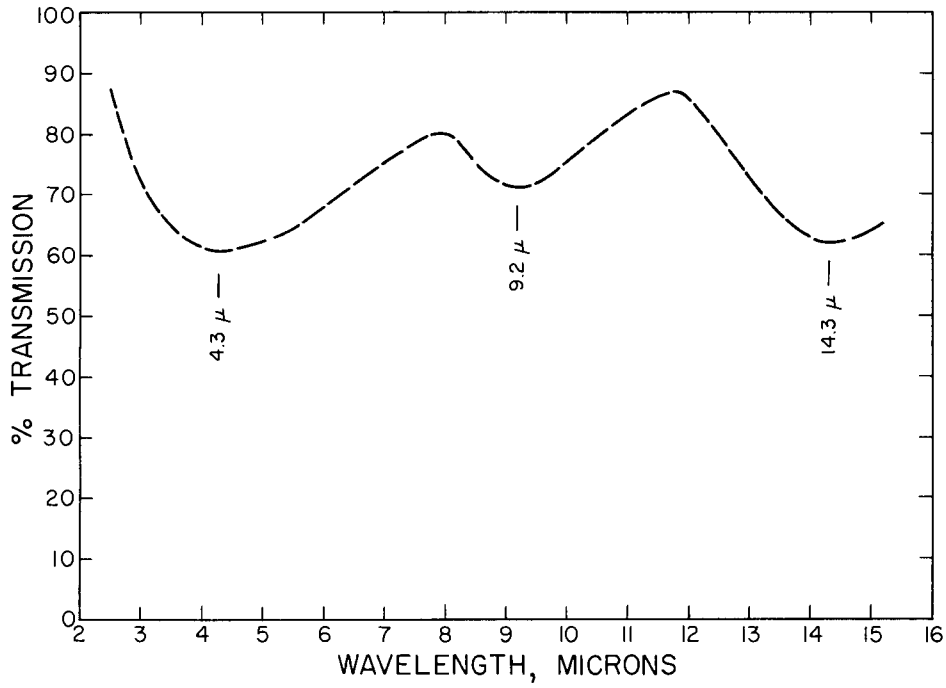

Fig. 4.12. Transmission Spectrum of 5000-A-Thick Anodic Film Formed on Zirconium in Anodizing Solution Containing Phosphoric Acid.

Preparation of Single Crystals of Zirconium and Its Alloys

J. C. Wilson

Large crystals were grown in as-deposited crystal bar zirconium by zoning below the melting point so that volatile impurities (particularly iron) would not be lost. Grains up to 5 cm long are easily grown in a single pass at 2 cm/hr, but these grains rarely occupy more than one-third of the cross section of the 18-mm-diam bar. Voids and cracks in the as-deposited bar are able to stop the growth of very large grains.

Crystals of Zircaloy-2 up to 5 cm long were grown in 7-mm-diam bars after quenching from the beta field. An electron-beam heated hot zone was traversed along the bar at a rate of 5 to 10 mm/hr. The maximum temperature in the center of the hot zone was about 1250°C. Large

[redacted]

crystals were grown earlier in 2-mm-thick Zircaloy-2 strips,[13] but the yield decreased in thicker sections. The yield of usable crystals is quite low in the 7-mm-diam bar (about 10%); large beta grains grow well, but several alpha grains are usually formed from each beta grain. Surprisingly, the large Zircaloy-2 grains appear to be more perfect (from Laue photographs) before annealing than do most of the zirconium single crystals.

Large crystals of Zircaloy-4 were grown in 18-mm-OD tubing with a 1-mm wall. The beta quenching operation was conducted by traversing a 1300°C zone along the bar at 4 cm/min and allowing the bar to cool by radiation in vacuum behind the traveling zone. Growth took place at a maximum temperature of 1200°C with the zone being traversed at 1 cm/hr. A photograph of a portion of the tube is shown in Fig. 4.13. Some grains are 15 cm long and up to 1 cm wide. The beta quench was carried out up to the position indicated on the photograph. The growth of large grains stopped there, although the zone traversed the full length of the tube during the growth pass. We believe this is the first time grains of this size have been produced in Zircaloy-4. A similar Zircaloy-2 tube, under identical growth conditions produced grains only half as large. The tubes will be analyzed for loss of alloying elements.

---

[13]J. C. Wilson and M. L. Picklesimer, "Variable-Gradient, Electron-Beam Heating Methods for Growing Single Crystals of Zirconium," pp. 502–20 in First International Conference on Electron and Ion Beam Science and Technology, ed. by R. Bakish, John Wiley & Sons, Inc., New York, 1965.

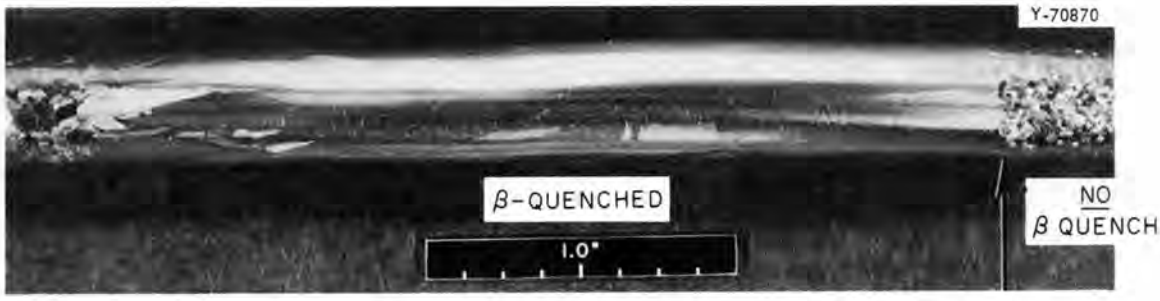

Fig. 4.13. Large Grains Grown in Zircaloy-4 Tubing by Zone-Heating Method (Solid State). Tubing is 18-mm-OD, 1-mm-thick wall. Note that large grains were not produced in the end of the tube that was not beta quenched.

[redacted]

Properties of High-Purity Zirconium

J. C. Wilson

Oxidation

We are studying the effects of crystal orientation and purity on the oxidation of zirconium so that we may obtain a more basic understanding of the variables that affect oxidation in engineering alloys. Since the oxidation of zirconium depends upon crystallographic orientation, and deformed alloys are often strongly textured, it is conceivable that texture control might be used to improve oxidation resistance of engineering alloys.

The anisotropy of oxidation after 20 min in air at 362°C in a single-crystal sphere of zone-refined zirconium is shown in Fig. 4.14. Compared to the work which we reported elsewhere,[14] much more fine detail is visible. The improved detail may be due to a more perfect crystal, or a better surface preparation, or both. The oxide is thickest (about 800 A) on this specimen in the narrow, light-colored (actually blue-white) regions bounded by dark (dark blue-to-purple) areas where the oxide thickness is between 400 and 500 A. The larger light areas (light brown-to-yellow) are covered with an oxide about 300 A thick. With the improved resolution, it can be seen on the specimen that the orientations very close to $\{0001\}$ have thinner films than those close to $\{10\bar{1}0\}$.

Oxidation of an as-grown, single-crystal sphere of hafnium at 362°C for 47 min in air produced the pattern shown in Fig. 4.15. There are obvious similarities to the pattern shown by zirconium (Fig. 4.14), but the thickest oxide (about 500 A) is found near $\{10\bar{1}3\}$ at the three large dark-ringed ovals, and near $\{31\bar{4}0\}$, at the smaller, more diffuse ovals. Also the oxide on $\{11\bar{2}0\}$ is thicker than on $\{10\bar{1}0\}$, just the reverse of the behavior on zirconium. The pattern is somewhat diffuse, but it probably will be better on an annealed sphere. This is believed to be the first semiquantitative determination of the anisotropy of oxidation in hafnium.

---

[14] J. C. Wilson, Metals and Ceramics Div. Ann. Progr. Rept. June 30, 1965, ORNL-3870, p. 183.

[redacted]

[redacted]

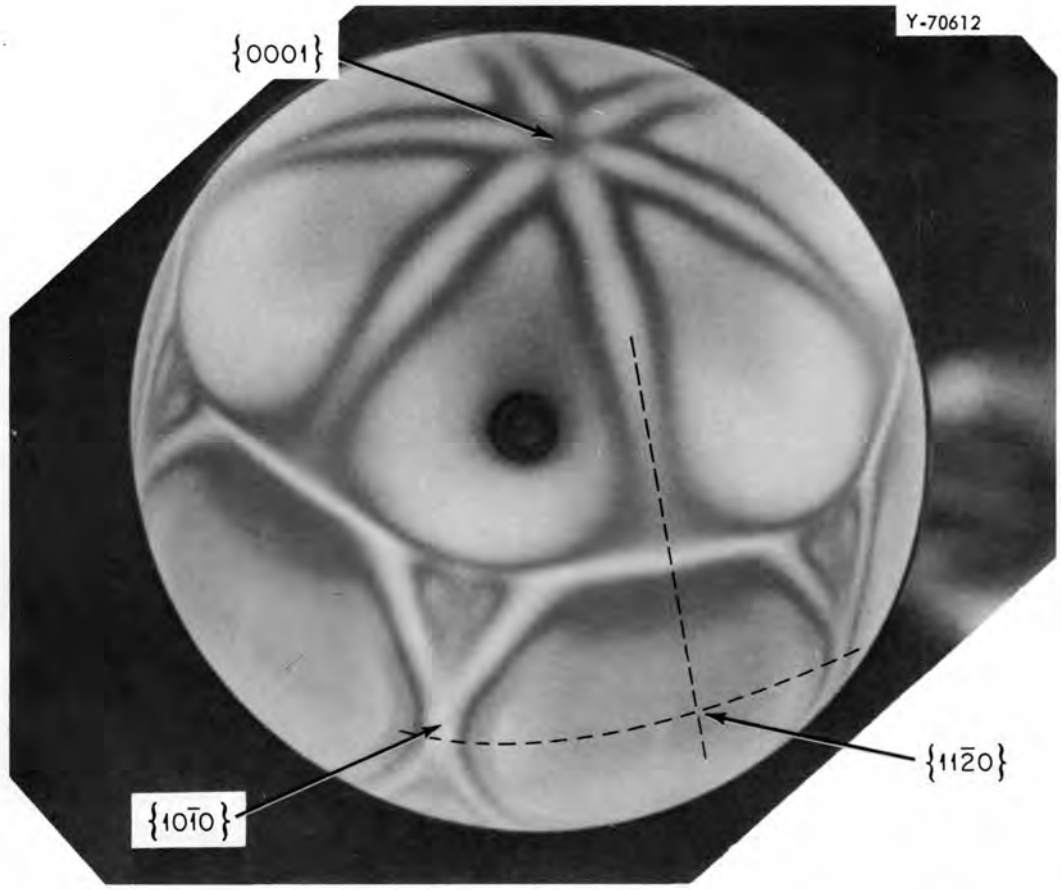

Fig. 4.14. Anisotropy of Oxidation of a Single-Crystal Sphere of Zirconium. Oxidized in air for 20 min at 362°C. The arrowheads indicate the poles of the designated planes. The diameter of the sphere is 1/2 in. See text for detailed description.

The study of the oxidation of such spheres is being continued to longer times and other temperatures. Other spheres have been made for oxidation in steam and in high-pressure water. Strip specimens from a rolled and annealed, zone-refined zirconium bar have been submitted for corrosion in 360°C water. An apparatus is being built to permit oxidation in 500°C steam at 1 atm.

[redacted]

[redacted]

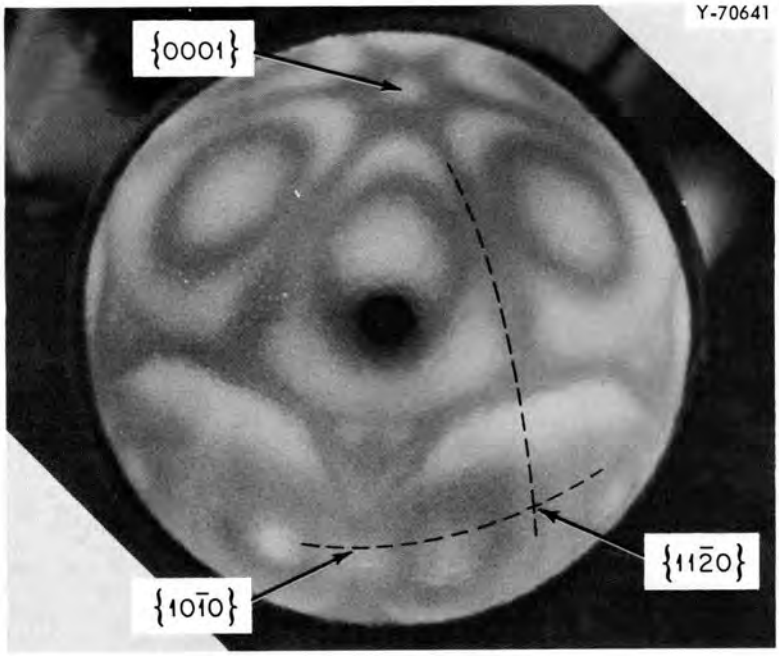

Fig. 4.15. Anisotropy of Oxidation of a Single-Crystal Sphere of Hafnium. Oxidized in air for 47 min at 362°C. The arrowheads indicate the poles of the designated planes. The diameter of the sphere is 3/8 in. See text for detailed description and compare with zirconium specimen in the previous figure.

[redacted]

[redacted]

[redacted]

[redacted]

PART II.

REACTOR CHEMISTRY DIVISION

[redacted]

[redacted]

[redacted]

[redacted]

5. FISSION-GAS RELEASE AND PHYSICAL PROPERTIES OF FUEL MATERIALS DURING IRRADIATION

R. M. Carroll J. G. Morgan
O. Sisman

We are studying the release of fission gas from UO_2 during irradiation in an effort to obtain a general formula to predict the behavior of fission gas in fuel materials. To accomplish this we irradiate carefully selected and characterized specimens in an irradiation facility where the neutron flux is controlled by positioning the specimen in the reactor and the temperature is controlled by air cooling the specimen capsule. Released fission gas is carried outside the reactor by a sweep gas where it is analyzed by gamma-ray spectrometry.

As a result of these studies, we have formed a defect-trap theory to explain the fission-gas release.[1] The mathematical formulation of the theory[2] required values of parameters that could not be obtained by steady-state-testing methods, so that we are also doing dynamic testing wherein either fission rate or temperature is oscillated about a selected value. In essence, a slight ripple of steady-state conditions is imposed on the specimen and the response of the specimen to the ripple is analyzed by use of perturbation theory.[3,4]

The experimental technique for the oscillating experiments requires an elaborate irradiation facility supported by precision instrumentation to produce the controlled perturbations. The mass of data resulting from the perturbations requires that the data be taken in a punch tape format and processed by computer techniques. The technique and equipment used for fission-gas release studies can also be applied to physical property measurements. The first such measurement has been thermal conductivity studies during the period of this report.

---

[1]R. M. Carroll and O. Sisman, Nucl. Sci. Eng. 21, 47 (1965).

[2]R. M. Carroll, R. B. Perez, and O. Sisman, J. Am. Ceram. Soc. 48(2), 55 (1965).

[3]R. M. Carroll and O. Sisman, Fuels and Materials Development Program Quart. Progr. Rept. Sept. 30, 1965, ORNL-TM-1270, pp.49–59.

[4]Ibid, Dec. 31, 1965, ORNL-TM-1400, pp. 59–71.

[redacted]

Uranium Dioxide Single-Crystal Specimens, C1-13, C1-18

The polished single-crystal specimens C1-18 were described in the last report.[4] These specimens were used to obtain the data necessary to develop the oscillating program. Early in this reporting period, these specimens began to emit fission gas in irregular steps which we have associated with specimen fracture. These specimens were removed from the reactor and examination showed that the specimens were broken into several large pieces, apparently along subgrain boundaries.

We think this breaking of the single-crystal specimens is caused by irradiation-generated defects accumulating at the subgrain boundaries until the thermal stress caused by the fission power exceeded the strength of the specimen. A high-temperature operation would cause the single crystal to fracture at moderate burnup. Such a fracture would not occur in a moderate-grain-size specimen because the generated defects could go to many grain boundaries instead of concentrating at a few locations.

Polished single-crystal specimens C1-13 were removed from the reactor in November 1964 and stored to await a suitable opportunity to continue the irradiation. After the C1-18 specimens showed signs of failure, the C1-13 specimens were reinstalled without difficulty. This was the first time a radioactive specimen had been loaded into the experiment.

When the irradiation began it became apparent that something was seriously wrong with the C1-13 specimens. The temperature measurements were not consistent with those previously measured for the same fission rate and air-cooling. Also the fission-gas release measurements were not consistent with the measured temperatures. The experiment was therefore terminated without obtaining any useful data.

Postirradiation examination showed that the C1-13 experiment had also broken into several large pieces, falling away from the thermocouple tips in the process (see Fig. 5.1). The breaking again seemed to be the result of the accumulation of defects at the subgrain boundaries. Since the specimen was not broken during its initial irradiation, the

[redacted]

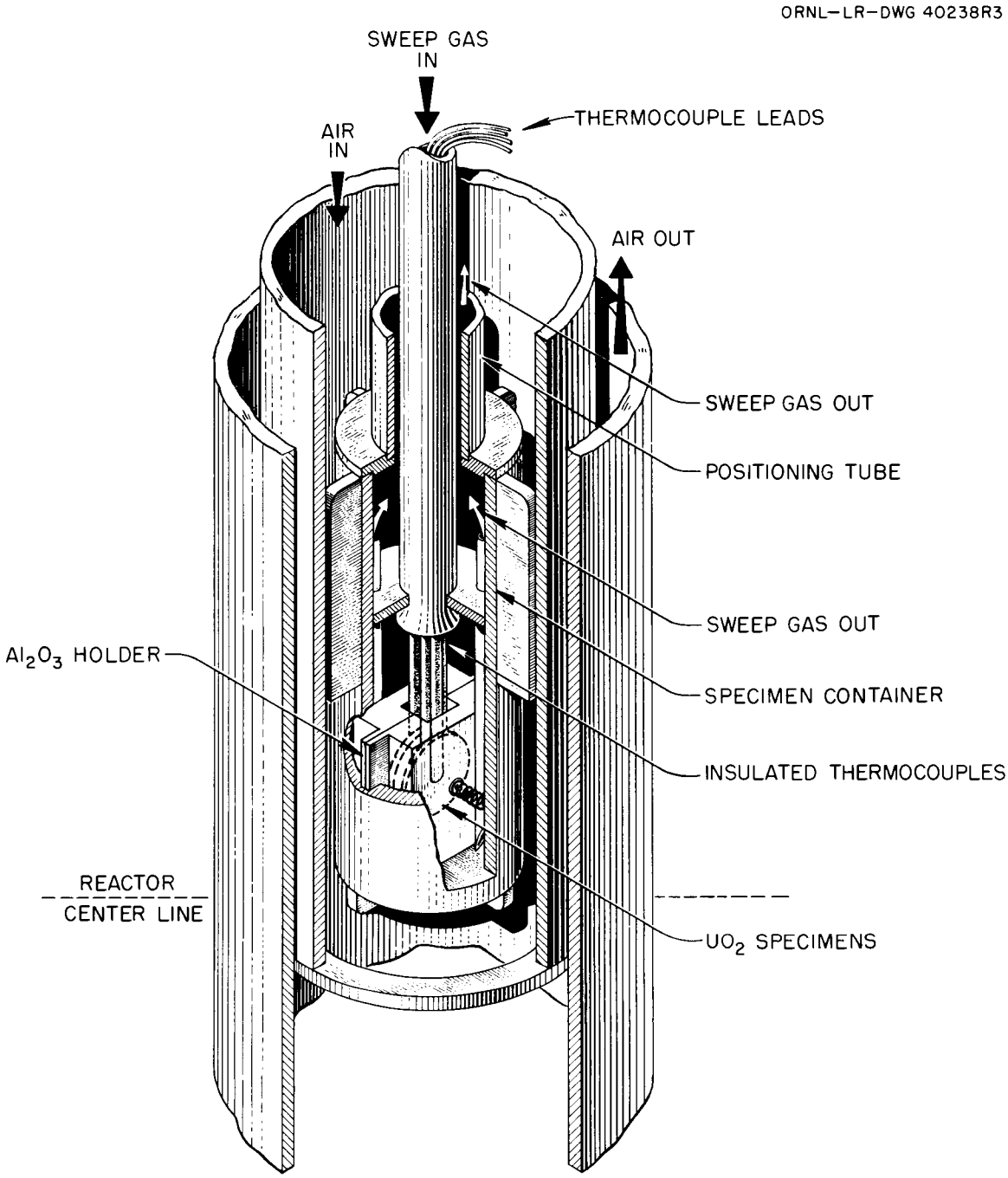

Fig. 5.1. Schematic of In-Reactor Capsule for Fission-Gas Release Experiments.

[redacted]

[redacted]

breaking happened during the removal, storage, or reinstallation (or possibly when the specimen was first reheated).

Uranium Dioxide Single-Crystal Specimen C1-19

In the past we have made some crude measurements of thermal conductivity of UO_2 during irradiation.[5] These measurements were secondary to fission-gas release studies and therefore the specimens were not designed to be really suitable for precise thermal conductivity measurements. The C1-19 specimen was designed to be used primarily for thermal conductivity and secondarily for fission-gas release measurements.

A single-crystal UO_2 specimen was machined into a hollow cylinder 2.92 cm long, 0.59 cm OD, and with a 0.25-cm axial hole (Fig. 5.2).

---

[5]R. M. Carroll and C. D. Baumann, Experiment on Continuous Release of Fission Gas During Irradiation, ORNL-3050 (February 1961).

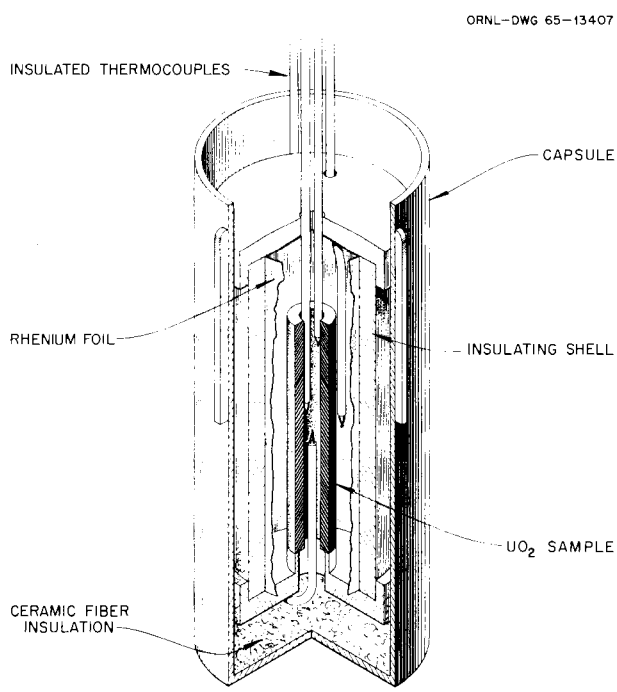

Fig. 5.2. Schematic of In-Reactor Capsule for Thermal Conductivity Experiments.

[redacted]

This specimen was inserted into an insulating shell, fitted with thermocouples, and placed in the in-reactor assembly in the same manner as before, replacing the capsules that contained the thin disk samples used for fission-gas release studies (see Fig. 5.1).

Essentially, the cylindrical specimen is suspended in an insulated cavity, surrounded by rhenium foil as a reflector. Three thermocouples are located along the specimen axis and three other thermocouples are located at various positions in the insulating layers. The purpose of the insulation is to reduce the thermal gradient between the outside of the specimen and the insulation and to allow high-temperature measurements without breaking the specimen through thermal stresses caused by high fission rates.

Methods of Thermal Conductivity Measurements

Thermal conductivity measurements have always been one of the more difficult physical property measurements. In-reactor measurements are complicated because of limited space, remote operations, and irradiation effects. One of the most formidable problems has been the measurement of temperature in a position where a high thermal gradient exists. We are trying to avoid this problem by measuring the temperature at the axis of the cylindrical specimen where thermal gradients are low.

In steady-state operation, two temperature measurements would be required, one at the center of the fuel and another at some other position. As mentioned above, the central measurement is easy; the other temperature is difficult to measure and the results uncertain. Since the difference of the two measurements is used in the thermal conductivity calculations, the uncertainty of the temperature produces uncertain thermal conductivity values.

The advantage of the oscillation method is that only the central temperature measurement is required. The fission power in the specimen is oscillated by moving the specimen capsule in a sinusoidal motion in the air-cooled irradiation tube (see Fig. 5.3). The fission power (fission rate) responds instantaneously to a change of neutron flux and the temperature of the specimen has a response that depends on

[redacted]

ORNL-DWG 64-7278

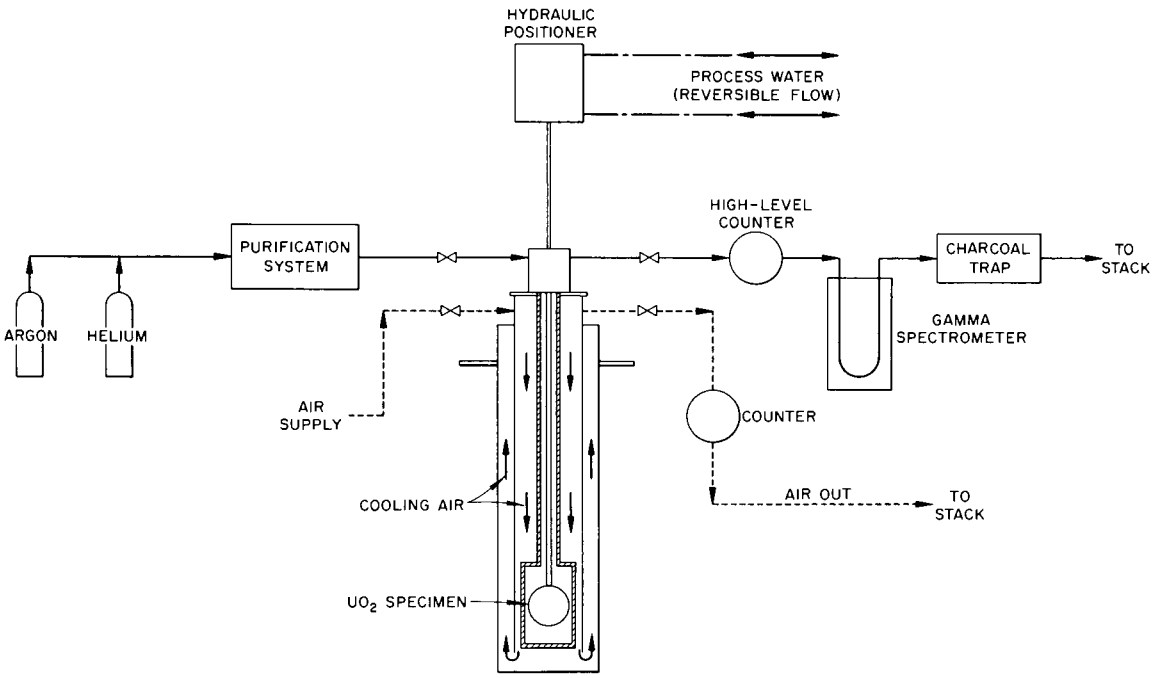

Fig. 5.3. Experiment Flow Pattern.

fission rate, specific heat, thermal conductivity, and emissivity of the specimen. The fission rate in the specimen is found by the use of the argon activation techniques developed for the fission-gas release measurements.[6,7]

When the neutron flux is oscillated, two aspects of the resultant temperature oscillations are measured — the phase shift between flux and temperature oscillations and the amplitude of the temperature oscillations. It is easy to change the frequency of the flux oscillation while maintaining a constant amplitude. The temperature then oscillates with the new frequency but with a different phase shift and amplitude. An example of how the temperature amplitude varies with frequency is given in Fig. 5.4.

---

[6]R. M. Carroll and O. Sisman, Fuels and Materials Development Program Quart. Progr. Rept. Sept. 30, 1965, ORNL-TM-1270, pp. 49–59.

[7]Ibid., Dec. 31, 1965, ORNL-TM-1400, pp. 59–71.

[redacted]

[redacted]

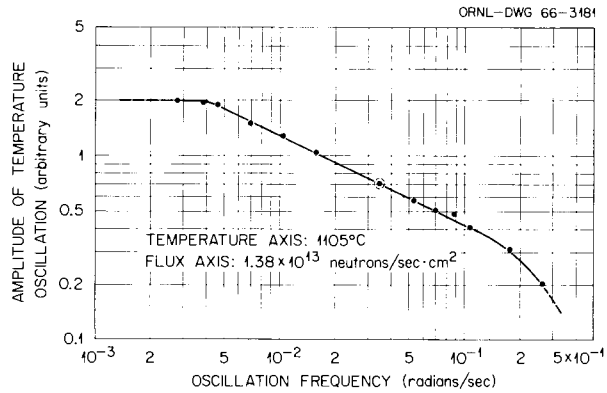

Fig. 5.4. The UO_2 Single-Crystal Temperature Response to Oscillating Fission Rate.

The temperature amplitude and phase shift are measured as a function of frequency and amplitude of flux oscillation; the mean values of temperature and flux remain constant. The mean specimen temperature is shifted by changing the air-cooling on the outside of the specimen capsule (see Figs. 5.1 and 5.3). The measurements can then be repeated with the new mean temperature as the only change. Later, the neutron flux axis is shifted and the entire range of measurements repeated. In this manner the thermal conductivity is measured as a function of temperature and fission rate. Measurements later in the experiment will determine the influence of burnup.

Data Processing

A large mass of data must be obtained during the oscillating programs. The data logging machinery used in the fission-gas release measurements is also used here.[6,7] A digital clock-Voltmeter alternately measures the position and temperature of the specimen and punches the measurements along with a time signal on a single paper tape. The tapes are processed through the computing center where the temperature and position cycles are analyzed and plotted separately. The curve analysis will be reprocessed to obtain values of thermal conductivity, specific heat, and emissivity.

[redacted]

[redacted]

The problems of processing large masses of data have been worked out. However, the first large processing of the data is just being completed at this time. The initial surveys of the data look very good. Oscillation periods as short as 24 sec are obtained and probably even shorter cycles can be used.

[redacted]

[redacted]

PART III.

SOLID STATE DIVISION

[redacted]

[redacted]

[redacted]

[redacted]

6. IRRADIATION EFFECTS ON ALLOYS AND STRUCTURAL MATERIALS

D. S. Billington M. S. Wechsler

The major emphasis of our research continues to be the study of radiation-hardening and radiation-embrittlement in the BCC metals and alloys. These metals have in common the tendency toward low-temperature brittleness, as displayed in a ductile-to-brittle transition. The increase in the ductile-brittle transition temperature upon irradiation is of technological interest particularly for low-carbon pressure-vessel steels because of the possible deterioration of the mechanical properties of reactor pressure vessels in service. In our program on pressure-vessel steels special consideration has been given to radiation effects on the heat-affected zones adjacent to welds. As is described below, simulated weld heat-affected-zone samples were observed to undergo about the same radiation embrittlement as the base plate, despite higher initial ductile-brittle transition temperatures for the heat-affected-zone samples in some cases. Also, the heat-affected-zone material appears to be less responsive to a post-irradiation annealing treatment. The annealing behavior of tensile samples of pressure-vessel steels is also being studied.

A rather extensive investigation is also underway on radiation hardening in vacuum-melted iron. Particular stress is placed on the possible specific influence of the dose rate. Whether or not there is a dose-rate effect is somewhat inconclusive at this time. However, the range of dose-rates surveyed is being extended, and a better evaluation of the matter should be possible in the near future. Plastic deformation in iron is being explored as a function of grain size, strain rate, and post-irradiation annealing. Also, the dislocation dynamics and thermally-activated properties are being studied using a stress relaxation technique.

As was mentioned above, the ductile-brittle transition phenomenon appears to be inherent in the BCC metals. Niobium is another BCC metal on which considerable effort is being exerted. In this case, high-purity single crystals can be prepared and the purification and crystal-growing

[redacted]

[redacted]

techniques are described below. Also, some of the results on etch pitting, slip line observations, and stress relaxation are given. Furthermore, mention is made of the use of a novel new technique, anomalous x-ray transmission topography, which permits dislocations to be seen in stereo view.

Finally, a brief description is given below of a cooperative program with investigators in the Metals and Ceramics Division at ORNL on grain-boundary radiation-embrittlement in Hastelloy-N nickel alloys. This embrittlement is thought to be due to helium production upon thermal neutron absorption by boron present as a trace impurity. Hence, to separate the effects of fast and thermal neutrons, the Thermal Flux Irradiation Facility in the BSR is being used to irradiate a series of Hastelloy-N tensile samples.

Radiation Effects on Pressure-Vessel Steels

R. G. Berggren W. J. Stelzman
T. N. Jones

Impact Tests on Irradiated Heat-Affected-Zone Samples of ASTM A-212B Pressure-Vessel Steel

Low-carbon steels may be given a thermal-cycling treatment to produce microstructures synthetically which reproduce those present in the heat-affected-zone of a weld. It was shown previously[1] that such synthetic heat-affected-zone samples of ASTM A-212B steel may have a considerably higher ductile-brittle transition temperature than the base plate. Furthermore, in an earlier study[2] of the effect of irradiation

[1]R. G. Berggren, W. J. Stelzman, and T. N. Jones, "EGCR Pressure-Vessel Surveillance Program," Radiation Metallurgy Section Solid State Division Progr. Rept. Aug., 1965, ORNL-3878, p. 62.

[2]R. G. Berggren, M. S. Wechsler, and T. N. Jones, "Brittle Fracture of Irradiated Structural Metals," Solid State Division Annual Progr. Rept. Oct. 31, 1963, ORNL-3213, p. 39.

[redacted]

on base-plate and simulated heat-affected-zone samples, it was found that the increase in transition temperature was approximately the same for the two materials, despite the higher initial transition temperature for the heat-affected-zone samples.

With the remote-controlled Charpy V-notch impact machine[3] installed in the hot cell and the calibration verified to be in accord with ASTM and AMRA specifications, a new series of impact tests on irradiated base-plate and heat-affected-zone samples was initiated. The results are shown in Figs. 6.1 to 6.4 and in Table 6.1. The unirradiated base plate gave a 20 ft-lb transition temperature of −20°C. The unirradiated heat-affected-zone material corresponding to a heat input of 50,000 joules/in. (Series 4B) had about the same transition temperature, but the unirradiated heat-affected-zone samples for 100,000 joules/in. (Series 2B) indicated a considerably higher transition temperature of 60°C. The heat-affected-zone samples received a stress relief anneal consisting of 4 hours at 620°C following the simulated weld thermal treatment cycle. As shown in Table 6.1, both types of heat-affected-zone samples showed about the same increase in transition temperature as the base plate upon irradiation.

The results of vacuum annealing treatments on the irradiated base-plate and heat-affected-zone impact samples are also shown in Figs. 6.1 to 6.4 and Table 6.1. For the base plate, 2-hr anneals at 300°C (Fig. 6.1) and 350°C (Fig. 6.2) caused a recovery of 65% and 85% of the radiation-induced transition temperature shift. In comparison to the 65% recovery at 300°C for the base plate, the 300°C-anneals for the heat-affected-zone samples produced recoveries of only 30% (Fig. 6.3) and 40% (Fig. 6.4) for the 2B and 4B series, respectively.

An irradiation experiment is now being prepared for exposure at 300°C. Recovery studies will not be conducted on these samples.

---

[3]R. G. Berggren, W. J. Stelzman, and T. N. Jones, "Hot Cell Equipment," Radiation Metallurgy Section Solid State Division Progr. Rept. Aug. 1965, ORNL-3878, p. 64.

[redacted]

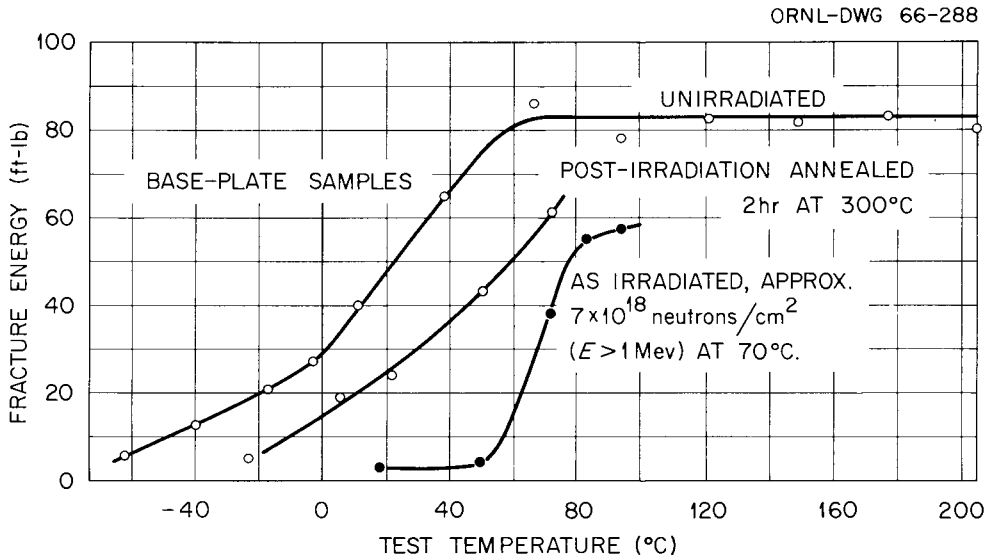

Fig. 6.1. Charpy V-Notch Fracture Energy vs Test Temperature for Unirradiated, Irradiated, and Post-Irradiation-Annealed Base-Plate Samples of ASTM A-212B Carbon-Silicon Steel, (SSD Item 147, Exp. ORR-30).

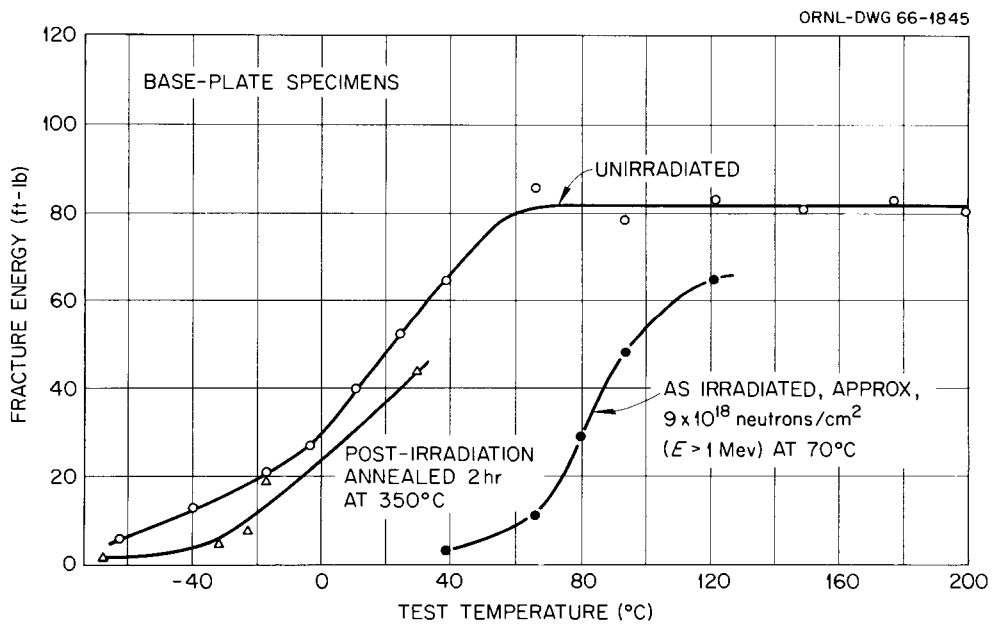

Fig. 6.2. Charpy V-Notch Fracture Energy vs Test Temperature for Unirradiated, Irradiated, and Post-Irradiation-Annealed Base-Plate Samples of ASTM A-212B Carbon-Silicon Steel, (SSD Item 147, Exp. ORR-30).

[redacted]

[redacted]

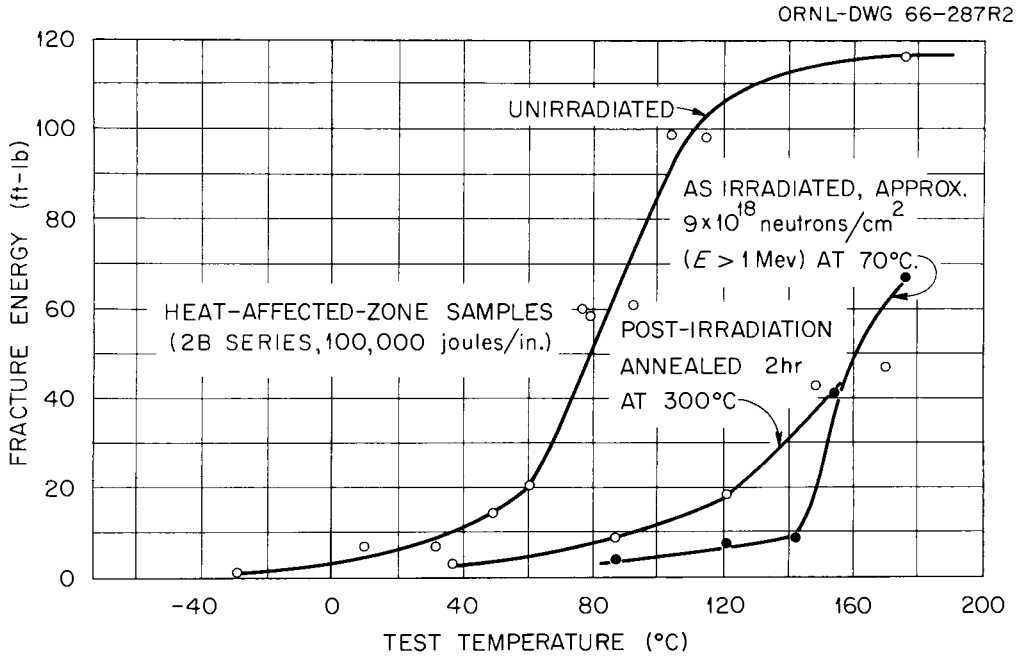

Fig. 6.3. Charpy V-Notch Fracture Energy vs Test Temperature for Unirradiated, Irradiated, and Post-Irradiation-Annealed Heat-Affected-Zone Samples of ASTM A-212B Carbon-Silicon Steel (SSD Item 147, HAZ 2B).

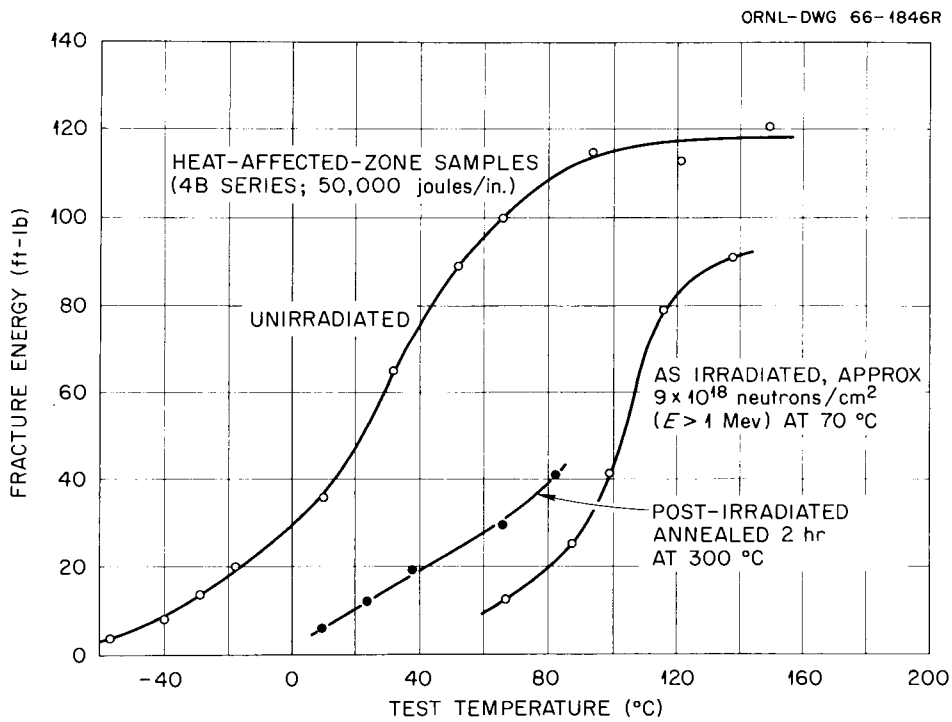

Fig. 6.4. Charpy V-Notch Fracture Energy vs Test Temperature for Unirradiated, Irradiated, and Post-Irradiation-Annealed Heat-Affected-Zone Samples of ASTM A-212B Carbon-Silicon Steel (SSD Item 147, HAZ 4B).

[redacted]

[redacted]

Table 6.1. The Effect of Irradiation and Post-Irradiation Annealing on the Ductile-Brittle Transition Temperature (DBTT) for Base-Plate and Heat-Affected-Zone Charpy Impact Samples of ASTM A-212B Pressure Vessel Steel.

Material	Dose[a]	DBTT at 20 ft-lb, °C				Anneal[b] Temp. (°C)	Recovery on Annealing (%)
		Before irrad.	After irrad.	change	After anneal		
	$\times 10^{18}$						
Base Plate	7	−20	62	82	10	300	65
	9	−20	74	94	−6	350	85
HAZ, 100,000 joules/in (Series 2B)	9	60	150	90	124	300	30
HAZ, 50,000 joules/in (Series 4B)	9	−18	80	98	40	300	40

[a]neutrons/cm^2, E > 1 Mev; irradiation temperature, 70°C.

[b]for 2 hr.

The Annealing of Radiation Hardening in Tensile Samples of ASTM A-212B Pressure-Vessel Steel.

Additional recovery studies were conducted on irradiated tensile test specimens of ASTM A-212B steel. Specimens were irradiated in a piggy-back position of the ORR poolside facility to fast neutron doses from 8 to 13 $\times 10^{18}$ n/cm^2 (E > 1 Mev). Exposure temperatures were 235°C ± 5°C for one experiment and 292°C ± 10°C for a second experiment. Recovery anneals were conducted in vacuum at temperatures ranging from 250 to 550°C for times of 25, 100, and 1400 minutes. Lower yield stresses after the 100-minute recovery treatments are presented in Fig. 6.5. Also shown in this figure are results adapted from Nichols and Harries,[4] for annealing of a silicon-killed steel after irradiation at 150°C to 7 $\times 10^{18}$

[4]R. W. Nichols and D. R. Harries, "Brittle Fracture and Irradiation Effects in Ferritic Pressure Vessel Steels," Radiation Effects on Metals and Neutron Dosimetry, ASTM-STP 341, Jan., 1963, p. 185.

[redacted]

[redacted]

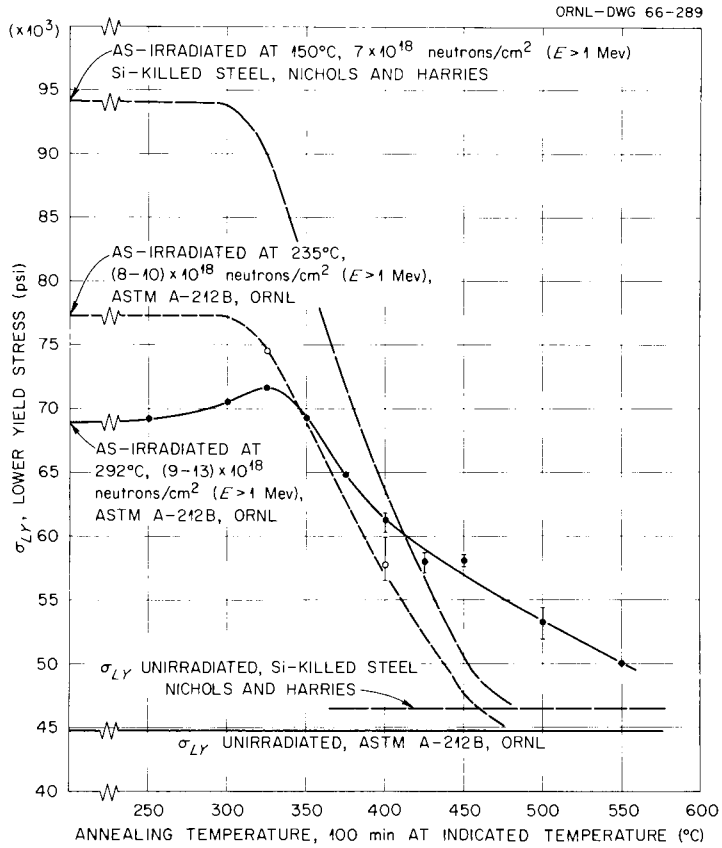

Fig. 6.5. Recovery of Lower Yield Stress of Irradiated Low-Carbon Pressure Vessel Steels.

neutrons/cm^2 (E > 1 Mev). The upper dashed curve represents and interpolation of their data for annealing times of 100 min. The lower dashed curve has the same shape as the upper one, but all yield stress values were reduced the same fractional amount necessary for agreement with the as-irradiated yield stress after irradiation at 235°C at ORNL. The points at annealing temperatures of 325°C and 400°C for irradiation at 235°C agree well with the adjusted Nichols and Harries curve for irradiations at 150°C, indicating a similarity of recovery mechanisms for the two studies. However, irradiation at 292°C results in rather different recovery kinetics. While the lower yield stress after irradiation at 292°C was lower than after irradiation at 235°C, the annealing above 350°C was more gradual for samples irradiated at 292°C. Similar results were obtained for recovery times of 25 and 1400 minutes. The activation energy obtained from this study

[redacted]

is presented in a following section.[5] An irradiation experiment is now being prepared for recovery studies of similar specimens after irradiation below 100°C.

Tensile Tests on Irradiated Iron

N. E. Hinkle N. K. Smith
M. S. Wechsler

The effect of neutron irradiation on the tensile properties of a high-purity vacuum-melted iron is being studied, with special emphasis on the specific role of dose-rate. The possible unique influence of the rate of neutron exposure is often neglected in assessing the radiation stability of structural materials. Yet, dose-rate effects may be quite important, since some reactor components such as the pressure vessels undergo radiation damage at low dose-rates over long periods of time (tens of years), whereas the materials evaluation work is done at high dose-rates for relatively short times (several months).

The experimental details of the irradiations have been given in previous reports[6-8] and some of the results are to be described soon in the open literature.[9] Six experiment assemblies containing samples of vacuum-melted iron were irradiated at a temperature of about 95°C in the poolside

---

[5] N. E. Hinkle, N. K. Smith, and M. S. Wechsler, this report.

[6] N. E. Hinkle and N. K. Smith, "Tensile Tests on Irradiated Iron," Fuels and Materials Development Program Quart. Progr. Rept. March 31, 1965, ORNL-TM-1270, p. 89.

[7] N. E. Hinkle and N. K. Smith, "Tensile Tests on Irradiated Iron," Radiation Metallurgy Section Solid State Division Progr. Rept. Aug., 1965, ORNL-3878, p. 27.

[8] N. E. Hinkle and N. K. Smith, "Tensile Tests on Irradiated Iron and Iron Alloys," Fuels and Materials Development Program Quart. Progr. Rept. March 31, 1965, ORNL-TM-1100, p. 65.

[9] N. E. Hinkle, S. M. Ohr, and M. S. Wechsler, "Radiation Hardening and Embrittlement in Iron, with Special Emphasis on the Effect of Dose Rate," to be presented at the ASTM Symposium on the Effects of Radiation on Structural Metals, Atlantic City, New Jersey, June 29-July 1, 1966.

of the ORR at various distances from the face of the reactor. The neutron fluxes were measured at each location using nickel monitors shielded with cadmium in order to eliminate the need for corrections due to ^{58}Co burn-up. The fluxes cover a range from 2×10^{11} to 3×10^{13} neutrons/cm^2 sec, corresponding to neutron energies greater than 1 Mev as calculated assuming a fission spectrum from the measured integral neutron fluxes greater than the 2.9 Mev ^{58}Ni threshold energy. Maximum void space was maintained between the experiment assemblies and the reactor core, and therefore no significant variation in spectrum from one experiment location to another is considered to have occurred.

The starting stock of vacuum-melted iron was Ferrovac-E in the form of 1 1/4-inch bars. The bars were swaged to 9/32-inch diameter and the tensile specimens were machined with a gage diameter of 0.146 inch and a gage length of one inch. The specimens were then given 2-hour vacuum-anneals at 885°C, 815°C, and 705°C, which resulted in grain sizes of 130μ, 60μ, and 17μ, respectively. For the work reported here, the 130μ and 17μ grain-size samples were used; these are designated as "coarse-grain" and "fine-grain," respectively. Photomicrographs of the grain structure, showing typical grain size variations for the coarse-grain and fine-grain samples, are given in Figs. 6.6a and b. The average grain diameter was determined by a lineal intercept count of the grains on a series of photomicrographs taken from two transverse sections from each specimen. In order to get a better measure of the grain size distribution in a given sample, a more refined technique involving counting each grain according to its size will be tried in the future.

Following the annealing, samples of the material were chemically analyzed, primarily to determine whether there was any pick-up of interstitial impurities during the annealing. The results of the post-annealing chemical analyses are given in Table 6.2, along with the mill analysis supplied by the manufacturer, Crucible Steel Company. No major change in composition upon annealing is seen, with the possible exception of nitrogen which increased from 1 ppm for the mill analysis to about 10 ppm after annealing.

PHOTO 82995

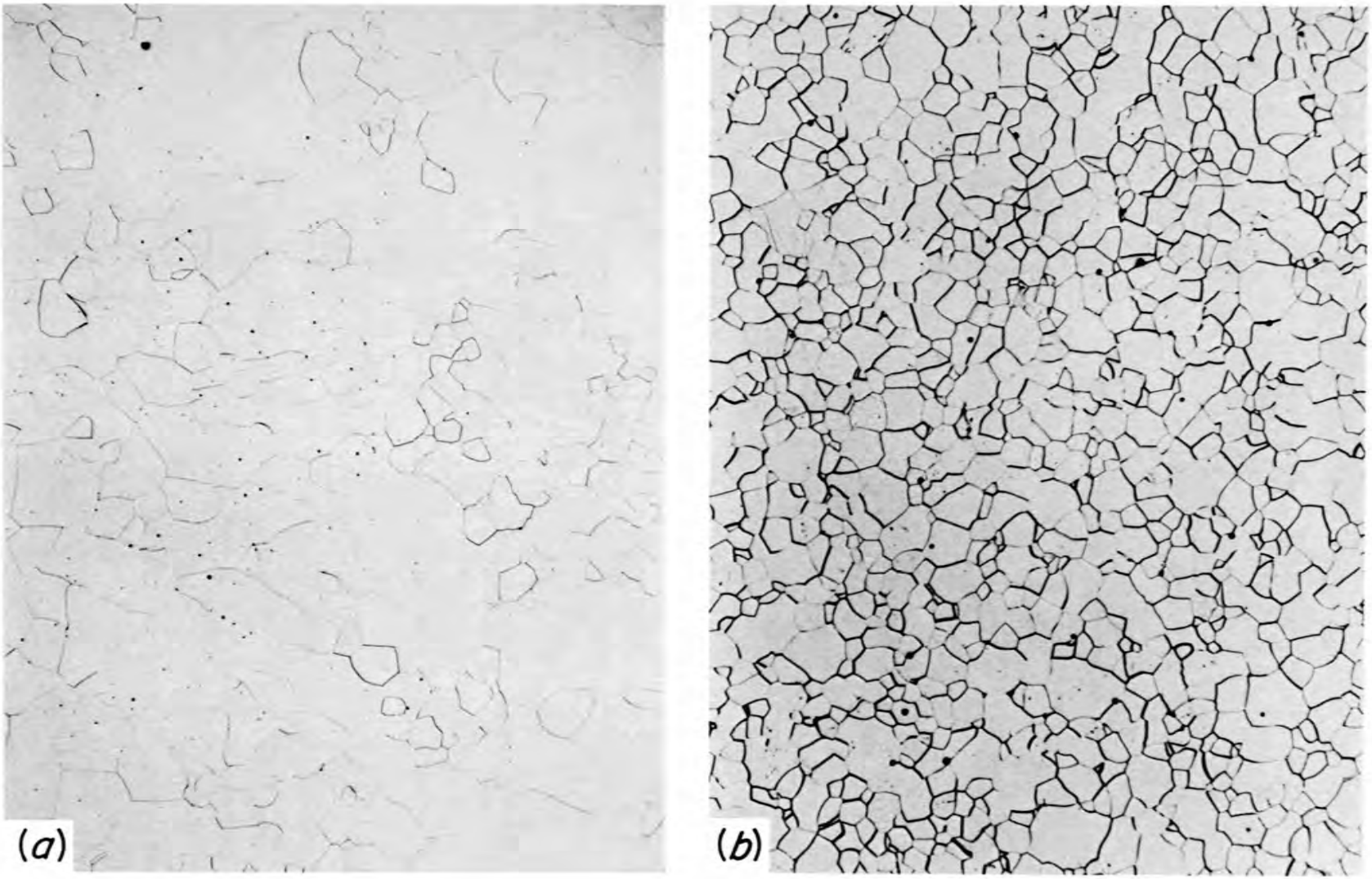

Fig. 6.6. Grain Structure of (a) Coarse-Grain, 50X and (b) Fine Grain, 250X Samples of Ferrovac-E Iron. Etchant: 2% nital.

Table 6.2. Chemical Analysis of Ferrovac-E Iron Tensile Specimens

Element	Original Mill Analysis (ppm)	Concentration after anneal at 885°C for 2 hrs (ppm)				Concentration after anneal at 815°C for 2 hrs (ppm)	Concentration after anneal at 705°C for 2 hrs (ppm)
		Batch 1	Batch 2	Batch 3	Batch 4		
Fe	base metal	---	---	---	---	---	---
C	40	40	40	40	30	40	30
O	65	74	71	66	72	80	68
N	1	9	9	12	13	12	6
H	0.3	< 1	< 1	< 1	< 1	< 1	< 1
S	70	10	10	20	10	21	10
P	50	7	10	10	5	7	5
B		20	10	10	20	10	20
Co	70	20	30	20	20	20	20
Cr	100	10	30	10	30	30	10
Cu	50	20	20	20	20	40	40
Mo	100	10	10	10	10	10	10
Ni	350	400	400	400	400	400	400
Si	60	200	700	100	100	200	100
Mn	10	10	10	10	10	10	10
V	40	1	1	1	1	1	1

At this writing, samples from five of the six irradiation assemblies have been tested. These were irradiated at dose-rates ranging from 4×10^{11} to 3×10^{13} neutrons/cm^2 sec ($E > 1$ Mev). For a portion of the samples, the attempt was made to vary the irradiation time so as to provide a constant dose of about 4.6×10^{18} neutrons/cm^2 ($E > 1$ Mev). This was achieved to within only about ± 25% and, therefore, corrections were applied in order to correct the measured yield stresses to a constant dose. In addition, corrections for variations in the test temperature in the hot cells between 19°C and 30°C were necessary. These variations were due mainly to changes in the cell ventilation inlet air temperature which is affected by the outside ambient air temperature. The cell temperature is now being controlled, which should eliminate the need for test temperature corrections in the future. Our measurements of the effect of test temperature indicate that the yield stress is about 1500 psi greater at 19°C than at 30°C for the coarse-grain samples, and about 2000 psi for the fine-grain samples. These dependences on test temperature near room temperature agree with those of Hutchinson[10] and of Pugh and Chang.[11]

In order to correct for the variations in dose, the yield stress, corrected as indicated above to a test temperature of 30°C, was plotted as a function of neutron dose without regard to dose rate. The results for the 130μ and 17μ grain-size samples are shown in Fig. 6.7. We note that our results agree well with those of Chow, McRickard, and Gurinsky[12] for the coarse-grain samples. However, the slopes of the lines in Fig. 6.7 are only about 0.10 to 0.15, values that are considerably smaller than

---

[10]M. M. Hutchinson, "The Temperature Dependence of the Yield Stress of Polycrystalline Iron," Phil. Mag. 8, 121 (1963).

[11]H. Ll. D. Pugh and S. S. Chang, "Tensile Properties of a High-Purity Iron from −196°C to 200°C at Two Rates of Strain," Phil. Mag. 8, 753 (1963).

[12]J. G. Y. Chow, S. B. McRickard, D. H. Gurinsky, "Mechanical Properties of Irradiated Iron and Iron Alloys," Symposium on Radiation Effects on Metals and Neutron Dosimetry, ASTM-STP-341, p. 46, 1963.

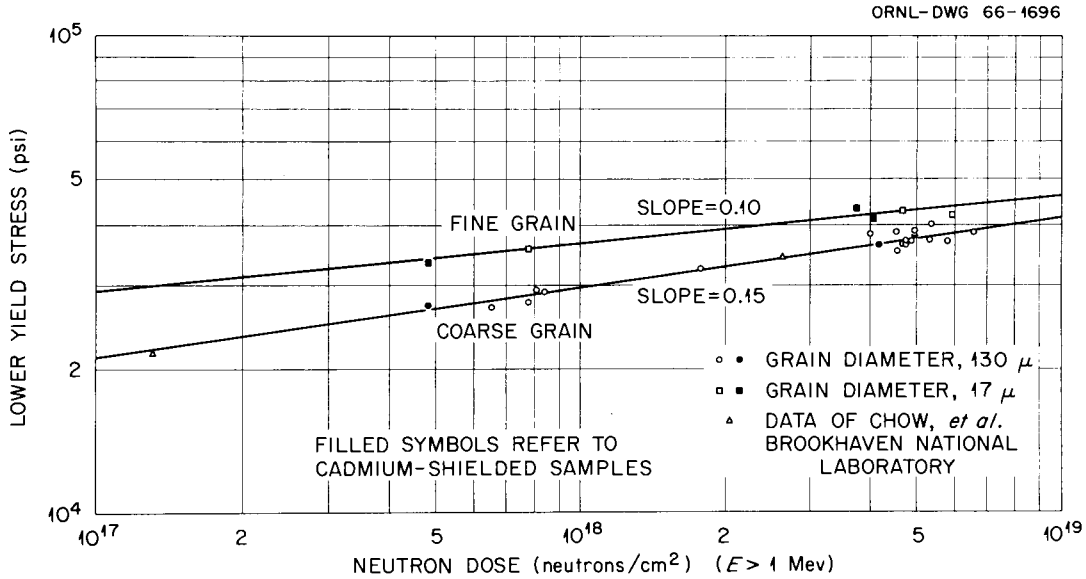

Fig. 6.7. Lower Yield Stress vs Neutron Dose for Ferrovac-E Iron of Two Grain Sizes After Correction to a Test Temperature of 30°C.

the value of about one-third observed for a similar plot of radiation-hardening in high-purity copper.[13] However, as has been discussed for copper recently,[13-14] some investigators maintain that a more fundamental measure of the dose dependence is obtained by plotting the logarithmic increase in yield stress versus dose. This is done in Fig. 6.8 using values of 12,500 psi and 27,000 psi for the unirradiated coarse-grain and fine-grain samples, respectively, and we find now that slopes close to one-third are obtained. In a similar analysis for radiation-hardening in a low-carbon steel, Nichols and Harries[15] found the slope

---

[13]T. H. Blewitt and T. J. Koppenaal, "Irradiation-Hardening in Face-Centered Cubic Metals," AIME Symposium on Radiation Effects, Asheville, N. C., September 8-10, 1965, to be published.

[14]M. J. Makin, "Radiation Damage in Face Centered Cubic Metals and Alloys," AIME Symposium on Radiation Effects, Asheville, N.C., September 8-10, 1965, to be published.

[15]R. W. Nichols and D. R. Harries, "Brittle Fracture and Irradiation Effects in Ferritic Pressure Vessel Steels, p. 162 in Symposium on Radia-Effects on Metals and Neutron Dosimetry, ASTM-STP 341, American Society for Testing and Materials, Phila., Pa., 1963.

[redacted]

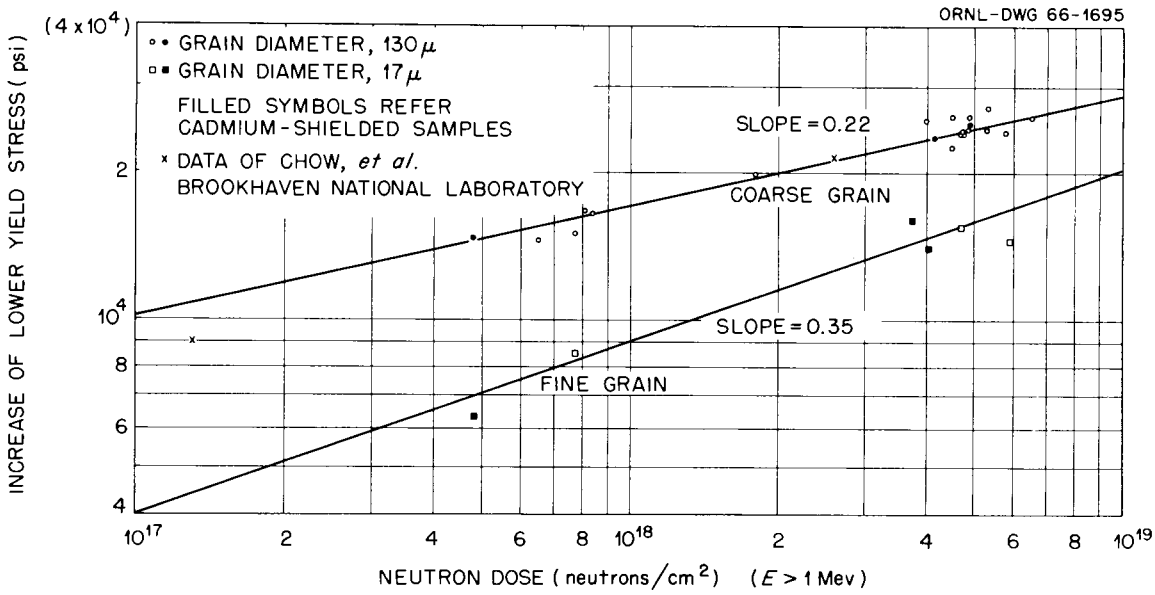

Fig. 6.8. The Radiation-Induced Increase of Lower Yield Stress vs Neutron Dose for Ferrovac-E Iron of Two Grain Sizes After Correction to a Test Temperature of 30°C.

to be close to 0.5. As concerns the magnitude of the corrections for variations in dose, it may be seen from Figs. 6.7 and 6.8 that for the samples irradiated to a nominal dose of 4.6×10^{18} neutrons/cm^2 (E > 1 Mev) the corrections in yield stress are within ±2000 psi.

In Fig. 6.9 the results of the dose-rate experiment are shown, with the yield stresses corrected to 4.6×10^{18} neutrons/cm^2 (E > 1 Mev) for variations in dose and to 30°C for variations in test temperature. A slight trend is noted toward a greater increase in yield stress upon irradiation to a constant dose at lower dose-rates, but this increase is barely outside the deviation in yield stresses for the unirradiated material due to variations in grain size. A better assessment as to whether or not a dose-rate effect exists should be possible when the samples from the sixth irradiation assembly are tested. These samples were irradiated at a dose-rate of about 2×10^{11} neutrons/cm^2 sec (E > 1 Mev), which is a factor of two smaller than for the lowest dose-rate points shown in Fig. 6.9.

[redacted]

[redacted]

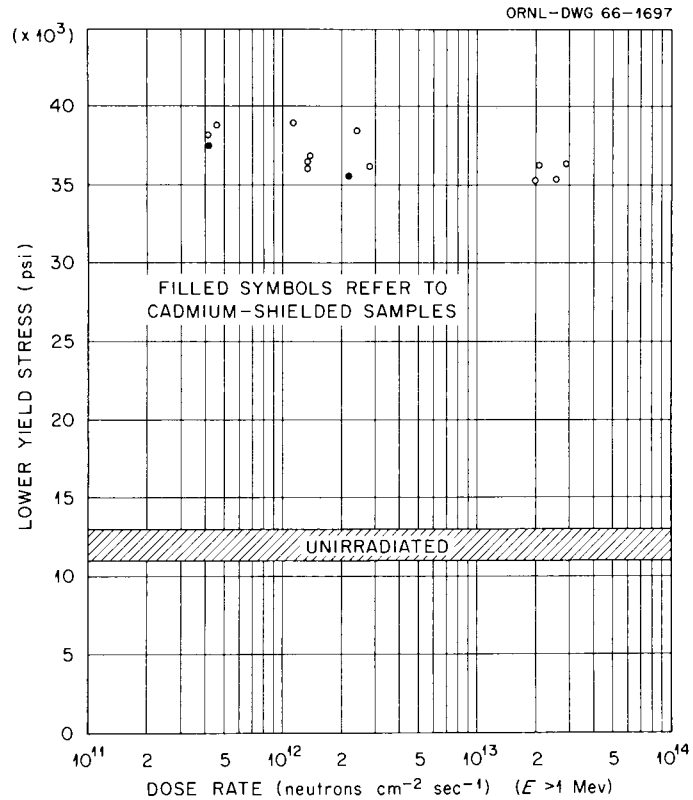

Fig. 6.9. The Lower Yield Stress, Corrected to a 30°C Test Temperature and a Neutron Dose of 4.6×10^{18} Neutrons cm^{-2} (E > 1 Mev), as a Function of the Dose-Rate Between 4×10^{11} and 3×10^{13} Neutrons cm^{-2} sec^{-1} (E > 1 Mev) for Ferrovac-E Iron of 130μ Grain Size. Irradiation Temperature: 95°C.

The dependence of yield stress, σ_{LY}, on grain size is often represented by the relation[16]

$$\sigma_{LY} = \sigma_i + k_y d^{-1/2}$$

where d is the grain radius. The effect of radiation on the parameters

[16]N. J. Petch, "The Clevage Strength of Polycrystals," J. Iron and Steel Inst. (London), vol. 174, p. 25, 1964.

[redacted]

σ_i and K_y has been discussed in the literature.[17-19] The parameter σ_i is generally observed to increase upon irradiation, but K_y for iron and steel has been found to remain constant upon irradiation[20-22] or to decrease.[23] Our experiments suggest that σ_i is increased and K_y decreased upon irradiation, as can be seen in Fig. 6.10. However, since results on only two grain sizes are available, only two points can be plotted for each curve. The decrease in K_y suggests that the irradiation produces a microstructural feature that pre-empts the role of the grain boundaries as the major barrier to macroscopic motion of dislocations.

The body-centered cubic metals are known to exhibit large temperature and strain-rate dependences for yielding and plastic flow. Furthermore, for high-purity copper, irradiation causes an increase in the temperature dependence of the critical shear stress.[13] Therefore, it is of interest to determine the effect of radiation on the thermally activated aspects of plastic deformation in iron. We have previously reported[6-7] on the strain-rate dependence of the yield stress in unirradiated iron of grain size 130μ. Some preliminary measurements of yield stress as a function of strain rate for this grain size have now been carried out for samples irradiated to 6×10^{17} and 5×10^{18} neutrons/cm^2 ($E > 1$ Mev).

---

[17] A. A. Johnson, N. Milasin, and F. N. Zein, p. 259 in Radiation Damage in Solids, Vol. I, International Atomic Energy Agency, Vienna, 1962.

[18] M. S. Wechsler, "Radiation-Embrittlement of Metals and Alloys," p. 296 in The Interaction of Radiation with Solids, North-Holland Publishing Company, Amsterdam, 1964.

[19] J. Moteff, "Radiation Damage in Body-Centered Cubic Metals and Alloys," AIME Symposium on Radiation Effects, Asheville, N. C., Sept. 8-10, 1965, to be published.

[20] D. Hull and I. L. Mogford, Phil. Mag. 3, 1213 (1958).

[21] D. Hull, Acta Met. 9, 191 (1961).

[22] I. L. Mogford and D. Hull, J. Iron Steel Inst. 201, 55 (1963).

[23] J. D. Campbell and J. Harding, "The Effect of Grain Size, Rate of Strain, and Neutron Irradiation on the Tensile Strength of Alpha Iron," p. 51 in Response of Metals to High Velocity Deformation, Interscience, New York, 1961.

[redacted]

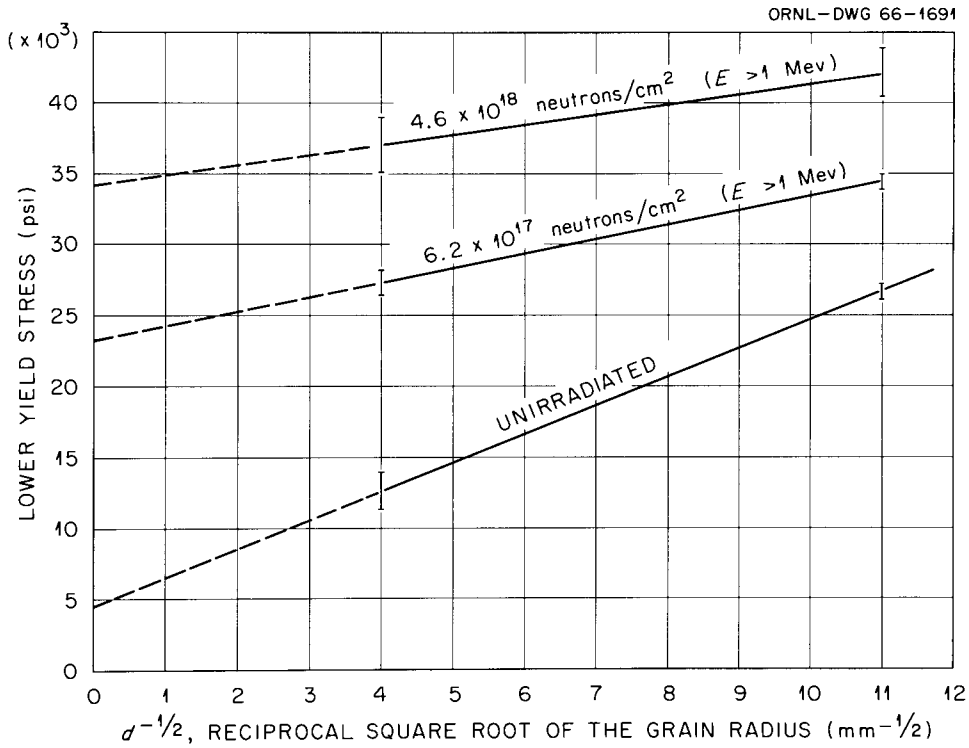

Fig. 6.10. The Lower Yield Stress Corrected to a Test Temperature of 30°C and to Indicated Neutron Doses as a Function of the Reciprocal Square Root of the Grain Radius ($d^{-1/2}$).

The results over a limited range of strain rates are shown in Fig. 6.11. The inverse strain-rate sensitivity is expressed as

$$m' = \frac{d\ln\dot{\epsilon}}{d\ln\sigma_{LY}}$$

and it is seen that over the range 0.002 to 0.2 min^{-1} in strain rates there appears to be no significant variation in the values of m'.

In the previous reports[6-7] we have also commented on the fact that stress relaxation methods as used by Ohr[9,24] enable a determination of a threshold stress, a stress which must be exceeded before macroscopic

[24]S. M. Ohr, this report.

[redacted]

[redacted]

ORNL-DWG 66-1693

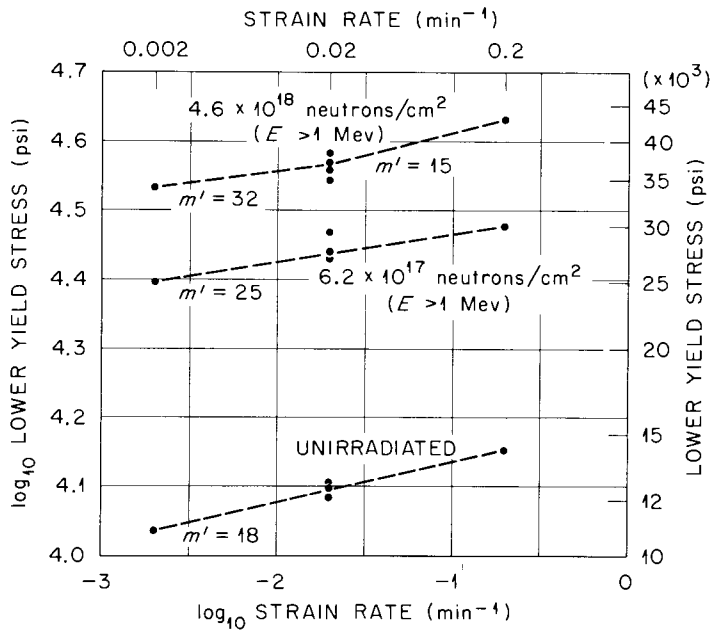

Fig. 6.11. Log Lower Yield Stress vs Log Strain Rate for Unirradiated Ferrovac-E Iron of 130μ Grain Size and for Two Irradiation Doses.

dislocation motion will take place. Furthermore, it was shown that the lower yield stress approaches the threshold stress in the limit as the strain rate approaches zero. Threshold stress measurements have now been carried out on irradiated samples with the coarse-grain (130μ) and fine-grain (17μ) structures. It is of interest to plot these stresses versus $d^{-1/2}$ in the same manner as in Fig. 6.10 for the total yield stress. The results are shown in Fig. 6.12 and it is again seen that there is a reduced dependence on the grain size for the irradiated material.

Post-irradiation annealing studies are being performed in order to gain further insight into the mechanism of radiation hardening. Also, typical operating temperatures of reactor pressure vessels are about 300°C, which is considerably above the irradiation temperatures near 100°C employed in these experiments. As is seen in Figs. 6.5 and 6.13, 300°C lies close to the temperature range at which annealing takes place in pressure-vessel steels and high-purity iron. For the iron, Fig. 6.13 shows the effect of two-hour anneals on the recovery of the yield stress of samples irradiated at 94°C to 1.7×10^{18} neutrons/cm^2 (E > 1 Mev) at

[redacted]

[redacted]

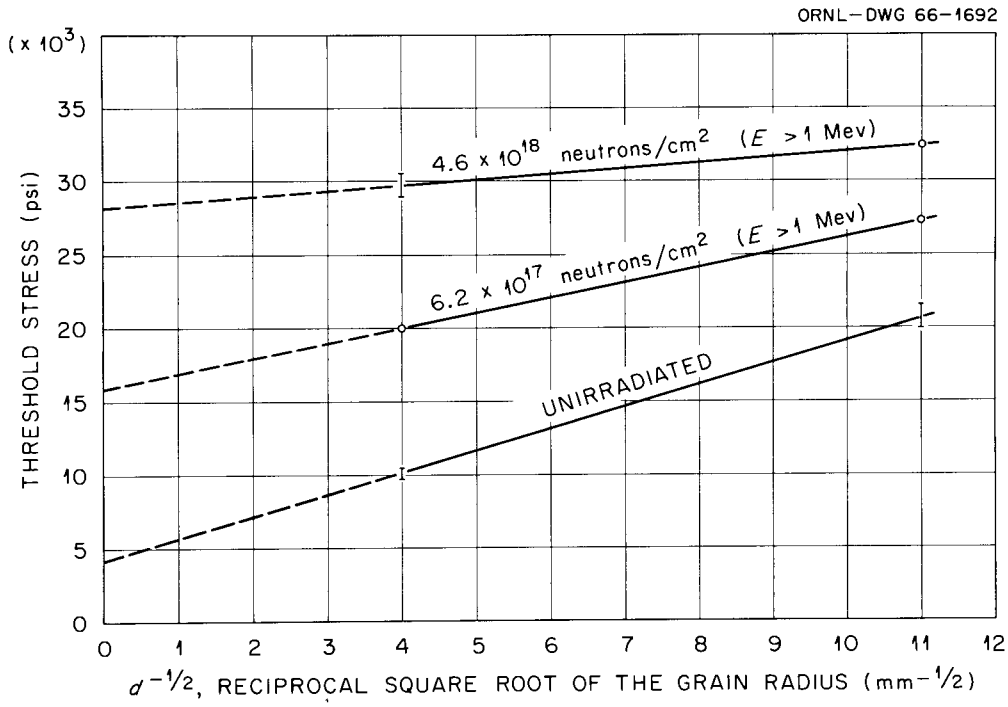

Fig. 6.12. The Threshold Stress at Given Neutron Doses vs the Reciprocal Square Root of the Grain Radius ($d^{-1/2}$).

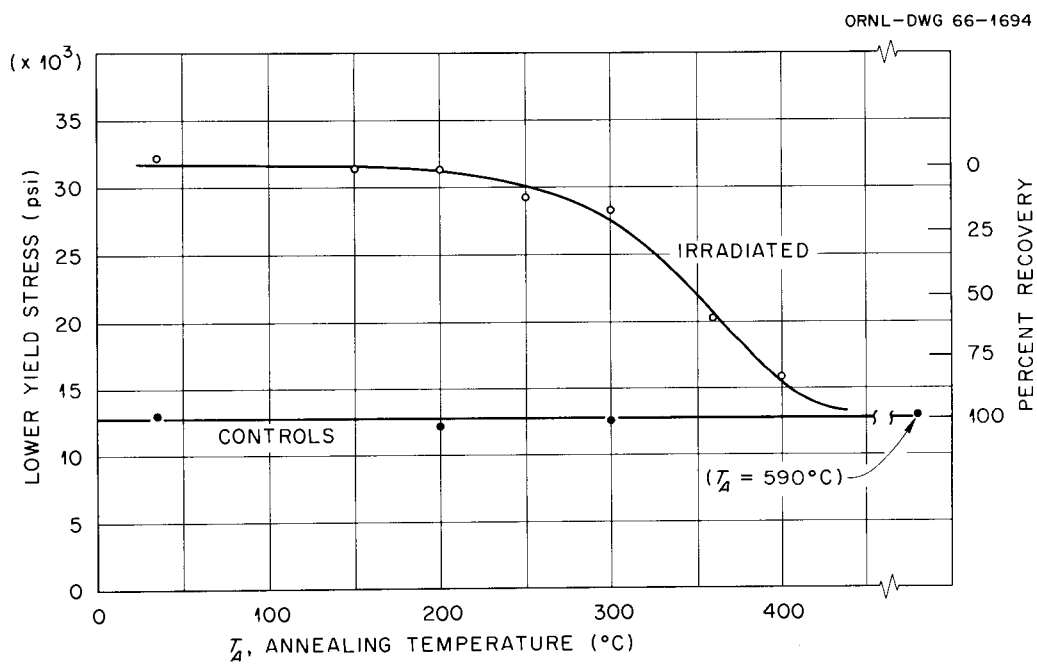

Fig. 6.13. Effect of 2-hr Anneals at Indicated Annealing Temperatures on the Yield Stress of Irradiated Ferrovac-E Iron Tensile Samples of 130μ Grain Size. Irradiation Temperature: 94°C. Irradiation Dose 1.7 $\times 10^{18}$ n/cm^2 (E > 1 Mev). Dose Rate: 8 $\times 10^{12}$ n/cm^2 sec (E > 1 Mev). Test Temperature: 30°C.

[redacted]

a flux of 8×10^{12} neutrons/cm^2 sec (E > 1 Mev). Each point represents a separate sample. For the unirradiated samples, it is seen that two-hour anneals up to 590°C have no effect on the yield stress. For the irradiated samples, 50% recovery occurs after a two-hour anneal at about 360°C and at 400°C about 85% recovery is realized. At 360°C, anneals were also performed for 15 min and 1000 min and the results of all anneals are shown in Fig. 6.14 as a function of isothermal annealing time. Earlier annealing studies on pressure-vessel steels by Nichols and Harries[25] indicated a constant activation energy over a range of annealing time and temperatures. Although our annealing data are incomplete at this time,

---

[25]R. W. Nichols and D. R. Harries, "Brittle Fracture and Irradiation Effects in Ferritic Pressure Vessel Steels," Symposium on Radiation Effects on Metals and Neutron Dosimetry, ASTM-STP 341, p. 162, 1963.

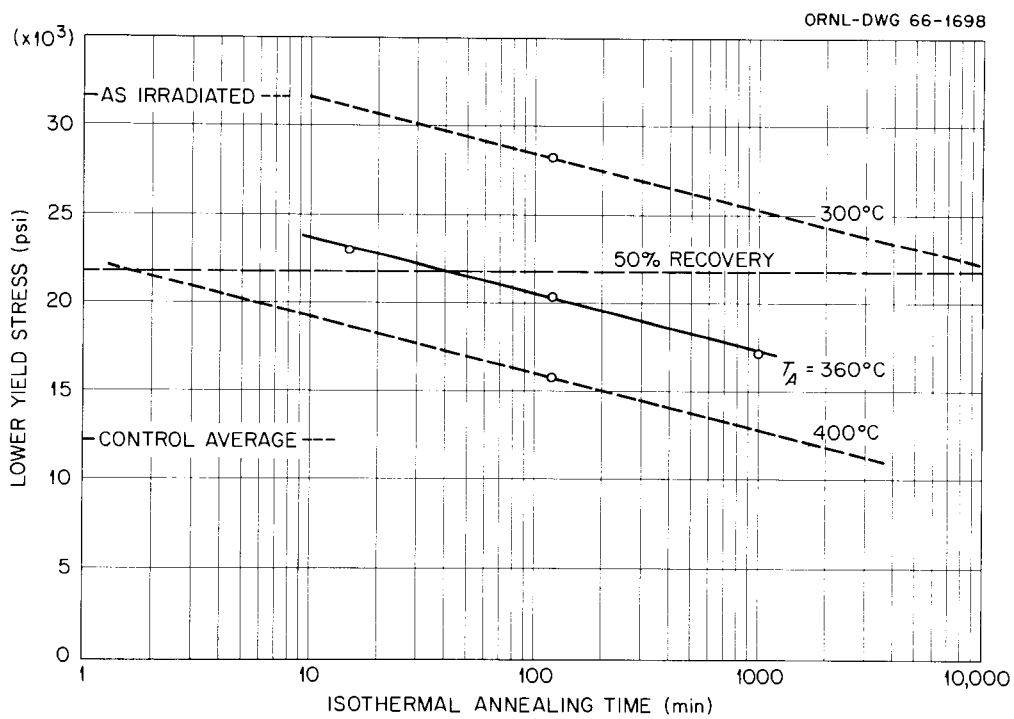

Fig. 6.14. Lower Yield Stress vs Isothermal Annealing Time for Ferrovac-E Iron Samples of 130μ Grain Size Irradiated at 94°C to 1.7×10^{18} Neutrons/cm^2 at 8×10^{12} Neutrons/cm^2 sec, (E > 1 Mev). Test Temperature: 30°C.

we may use the constancy of activation energy to make a preliminary analysis of the kinetics of the annealing. Therefore, in Fig. 6.14 the curves for 300°C and 400°C are drawn with dashed lines parallel to the curve determined for 360°C.

The assumption of a constant activation energy presupposes that a characteristic time τ exists such that the fractional recovery, f, is given by $f = f(t/\tau)$. Thus, the equation may be inverted to give

$$\frac{t}{\tau} = g(f)$$

$$\ln t - \ln \tau = \ln g(f)$$

If τ is set equal to

$$\tau = \tau_0 \exp (H/kT)$$

where τ_0 is a constant, we obtain

$$\ln t - \frac{H}{kT} = \ln g(f) + \ln \tau_0$$

Hence by plotting the time (on a log scale) for a given fractional amount of annealing, f, against 1/T, a straight line should result whose slope gives H. This was done in Fig. 6.15 and the activation energy for iron turns out to be about 3 ev. This agrees roughly with the activation energy, Q, for self diffusion of about 2.5 ev measured by Borg and Birchenall[26] and Lai and Borg[27] for alpha iron above the Curie point.

---

[26]R. J. Borg and C. E. Birchenall, Trans. Met. Soc. AIME 218, 980 (1960).

[27]D. Y. F. Lai and R. J. Borg, Trans. Met. Soc. AIME 233, 1973 (1965).

[redacted]

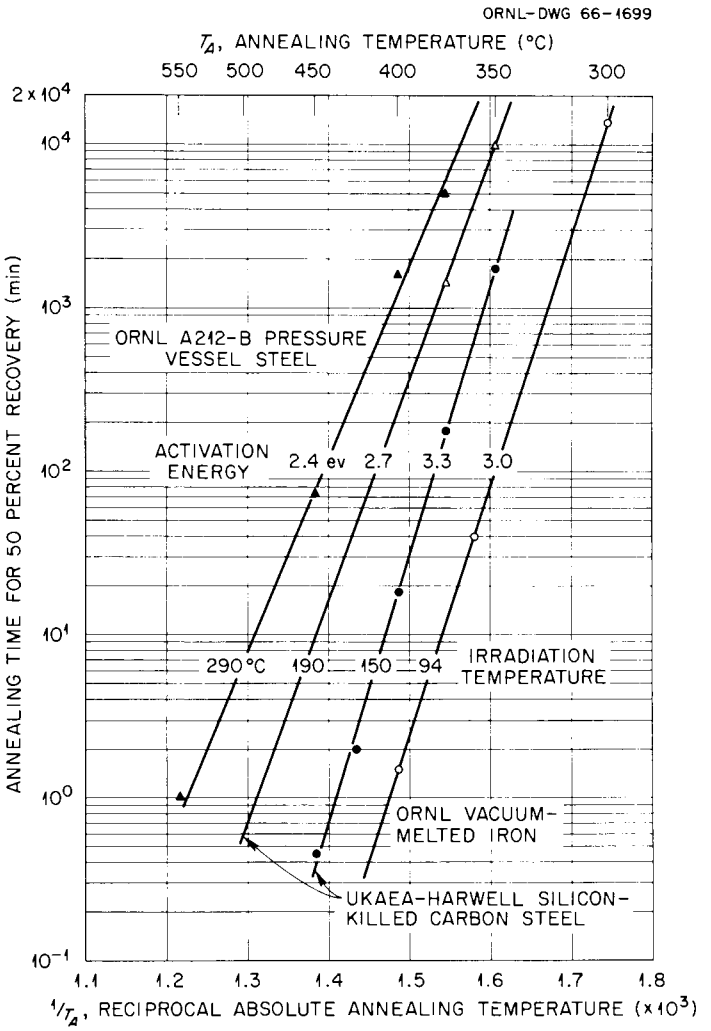

Fig. 6.15. Annealing Time for 50% Recovery of the Yield Stress for Irradiated Iron and Steel.

As was pointed out,[18] if we assume that the yield stress annealing is governed by the annealing of lattice vacancies in thermal equilibrium at the annealing temperature, the jump rate per atom is given by

$$\Gamma = AZ\nu_0 \exp(-Q/kT)$$

and at 370°C for Q = 3 ev and the values of the constants given in Ref. 18 we find $\Gamma = 4 \times 10^{-9}$ jumps/sec. From Fig. 6.15, the time to reach half-annealing is 10 min for iron at 370°C. Therefore, the number of atom jumps in this time is only about 2×10^{-6} per atom. This number of jumps

[redacted]

is much too small to be reasonable, as was also the case for the steels.[18,25]

A suggestion has recently been made by F. A. Nichols[28] that the radiation hardening is due largely to vacancy clusters or pores produced by the irradiation and that the annealing is due to the migration and coelescence of the vacancy pores. In this case, the kinetics of the radiation annealing are governed not by volume self-duffusion, but by surface diffusion at the inside wall of vacancy pores. The effective diffusivity for the pore is given by[28,29]

$$D_p = \frac{D_s}{8\pi}\left(\frac{a_o}{r}\right)^4 \qquad (1)$$

where D_s is the surface self-diffusion coefficient, r is the radius of the pore, and a_o is the lattice parameter. Since r is not expected to vary greatly with temperature over the small interval (300 - 400°C) covered in our experiments, the effective activation energy for the diffusion of the pore will be equal to that for surface self-diffusion. The value obtained by Blakely and Mykura[30] from scratch-smoothing experiments on alpha iron was 2.5 ev, which is essentially equal to the 3 ev shown in Fig. 6.15 for the annealing of radiation hardening. Also, as pointed out by Nichols,[28] the half-annealing time may be correlated roughly with the time necessary for the pores to move a distance equal to the distance between the pores. If this distance is denoted by R

$$t = \frac{\overline{R^2}}{6D_p} = \frac{4\pi\overline{R^2}r^4}{3D_s a_o^4} \qquad (2)$$

---

[28]F. A. Nichols, Theory of Radiation Embrittlement and Recovery of Radiation Damage in Ferritic Steels, WAPD-T-1865, October 1965.

[29]R. S. Barnes, "Mechanisms of Radiation-Induced Mechanical Property Changes," p. 40 in Flow and Fracture of Metals in Nuclear Environments, ASTM-STP-380, American Society for Testing and Materials, Phila., Pa., 1965.

[30]J. M. Blakely and H. Mykura, "Studies of Vacuum Annealed Iron Surfaces," Acta Met. 11, 399 (1963).

from Eq. (1). For our irradiation the dose was about $\Phi = 2 \times 10^{18}$ neutrons/cm^2 for which the pore density is estimated to be[28] $N = \Sigma\Phi = 0.5\text{cm}^{-1} \times 2 \times 10^{18}\ \text{cm}^{-2} = 10^{18}$ pores/cm^3 and therefore $R = N^{-1/3} = 10^{-6}$ cm. Also from the results of Blakely and Mykura[28,30] $D_s = 4 \times 10^{-15}\ \text{cm}^2\ \text{sec}^{-1}$ at 370°C. Hence, we find that for the observed 10 min half-annealing time at 370°C (Fig. 6.15) Eq. (2) predicts a pore size of $r/a_o \cong 1$.

Figure 6.15 also shows annealing results for tensile tests on irradiated steels taken from the work of Nichols and Harries[25] and Berggren et al.[31] The curves show that the half-annealing times for a given annealing temperature increase with increasing irradiation temperature. This may be understood in terms of the pore-migration mechanism by suggesting that the pore size, r, and the inter-pore distance, R, increase with increasing irradiation temperature giving rise to longer annealing times according to Eq. (2).

In the experiments described below certain fine-and coarse-grain specimens were wrapped in cadmium foil to shield them from thermal neutrons and thus to determine whether thermal neutron effects, such as transmutation reactions or (n,γ) recoil events play a part in the radiation hardening. The results shown in Figs. 6.7 and 8 indicate no significant difference in the radiation hardening of samples shielded from thermal neutrons as compared to the unshielded samples for which the thermal neutron flux was approximately five times the integral fast neutron flux above 1 Mev (see Fig. 6.14, Ref. 6).

All of the previous discussion was concerned with measurements at the onset of yielding in the irradiated iron. Some mention should also be made of deformation at and near the tensile fractures. Fig. 6.16 shows the appearance of the necked region for an unirradiated sample and for a sample irradiated to a dose of 4.6×10^{18} neutrons/cm^2 ($E > 1$ Mev). Both samples were fine grained and were deformed at room temperature at

---

[31] R. G. Berggren, W. J. Stelzman, and T. N. Jones, this report.

PHOTO 82994

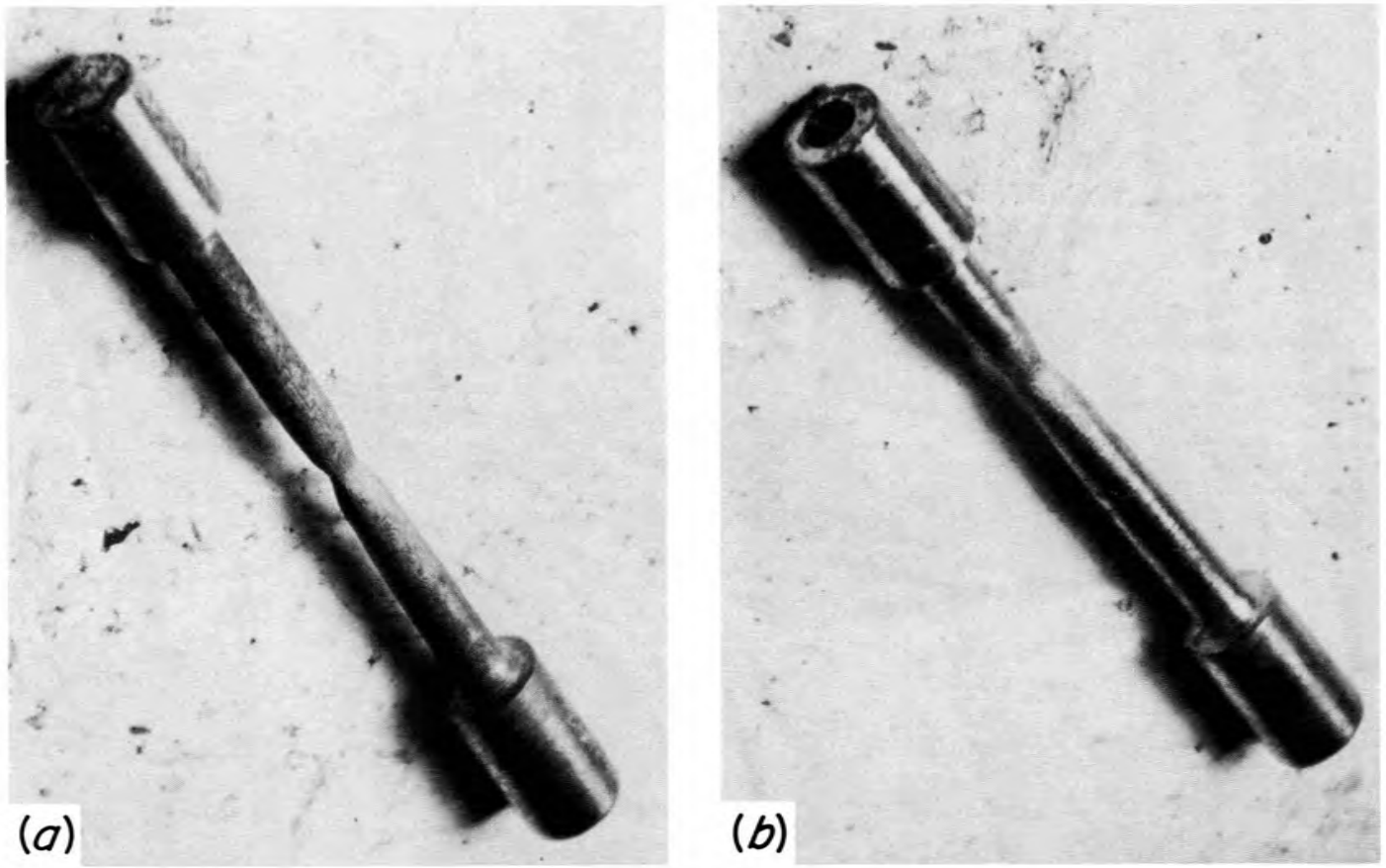

Fig. 6.16. Photographs of (a) Unirradiated, and (b) Irradiated, Tensile Specimens of Fine-Grain Ferrovac-E Iron Strained Beyond the Uniform Elongation. The neutron dose of the irradiated sample was 6×10^{18} neutrons/cm^2 ($E > 1$ Mev). The strains at which the tensile loads began to decrease were 31 and 16 percent for (a) and (b), respectively.

a nominal strain rate of 0.02 min^{-1}. The irradiated sample is seen to exhibit considerable reduction of area at room temperature and no cleavage fracture was noted. However, because of reduced rates of work hardening in the irradiated material, the uniform strain was substantially reduced. A remotely-operated extensometer of 1/2-inch gage length was used, which provided more reliable strain values than from the crosshead motion alone. The extensive deformation in the necked region for the irradiated iron is also seen in the photomicrographs of Fig. 6.17, which show the elongated grain structure in a longitudinal section at the neck.

Dislocation Dynamics in Irradiated Iron

S. M. Ohr

We have reported previously[32] a study of dislocation dynamics in irradiated and unirradiated iron samples by applying a stress relaxation technique. The study has yielded such information as the stress dependence of dislocation velocity, the density of mobile dislocations and the threshold stress at which the dislocations move on a macroscopic scale. It was found that the threshold stress was significantly high from the onset of plastic deformation. To establish a true stress dependence of the dislocation velocity, the threshold stress was subtracted from the applied stress for both unstrained and strained crystals. When this was done, a new stress dependence of the velocity that was independent of purity, strain and strain rate was obtained. Also, the plastic strain rate could be separated into two contributions due to the motion of two species of dislocations with the indices, m, of approximately 7 and 2.5. It was proposed that the two species represented the edge and screw dislocation segments, respectively.

It was also found that the radiation hardening as reflected by the lower yield stress could be attributed to two causes: (1) an increase

---

[32]S. M. Ohr, "A Study of Radiation Hardening in Iron by Stress Relaxation Techniques," Radiation Metallurgy Section Solid State Division Progr. Rept. Aug., 1965, ORNL-3878, p. 16.

PHOTO 82993

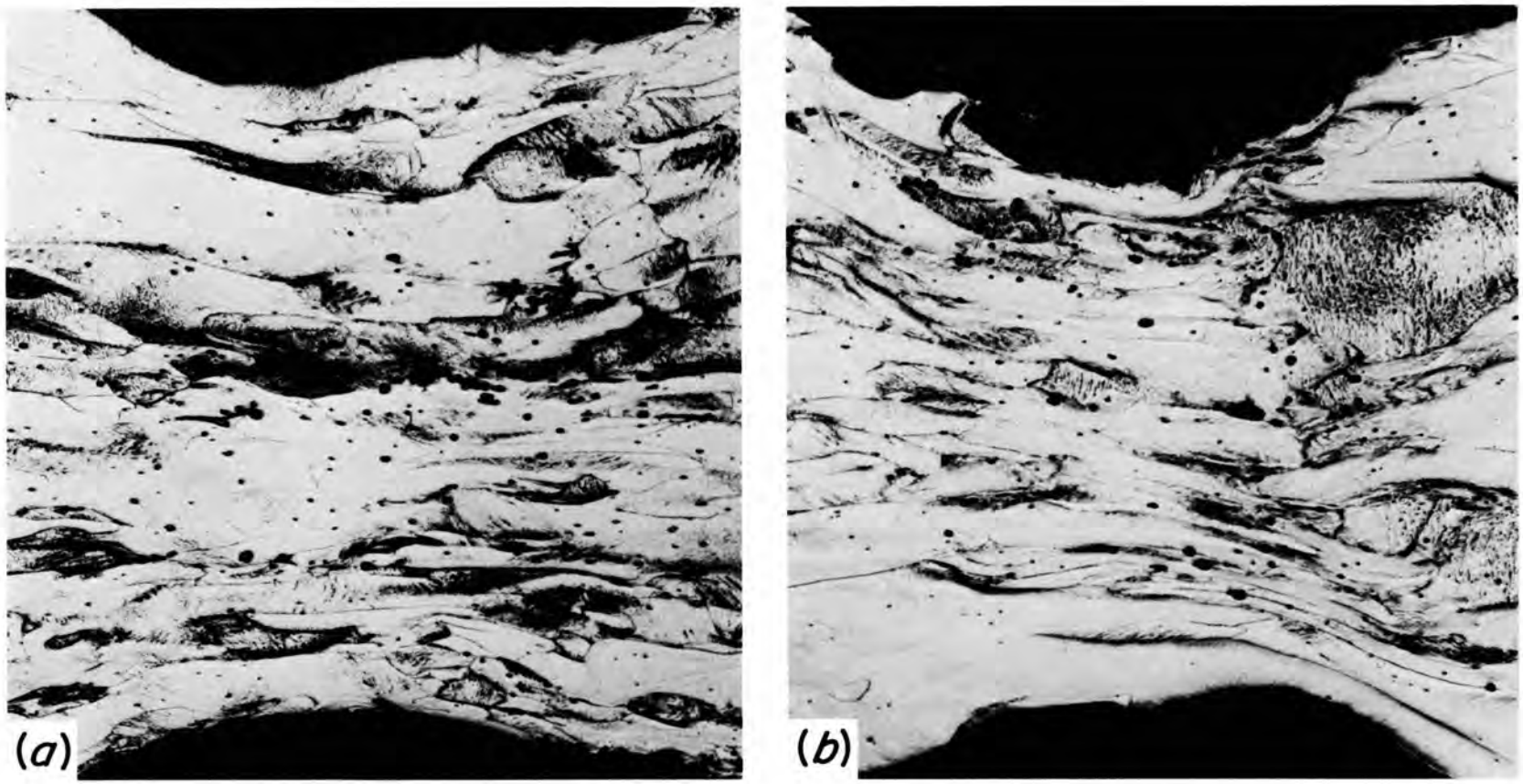

Fig. 6.17. Photomicrographs of Longitudinal Sections of Highly Strained Necked Regions of (a) Unirradiated and (b) Irradiated Tensile Specimens of Coarse-Grain Ferrovac-E Iron. The irradiated sample received a neutron dose of 4.5×10^{18} neutrons/cm^2 ($E > 1$ Mev). Etchant, 2% nital.

in the dynamical resistance of the lattice to dislocation motion, and (2) the difficulty in the generation and multiplication of dislocations. The measurements indicated that, while the density of mobile dislocations was lowered by as much as 2 orders of magnitude upon irradiation, the major cause of the radiation hardening was the increase in the dynamical resistance of the lattice to dislocation motion.

We have extended the study of dislocation dynamics to determine the activation volume in both irradiated and unirradiated iron samples. The activation volume, v^*, is defined as[33]

$$v^* = b\,l\,d$$

where b is the Burgers vector, l is the length of the dislocation segment involved in the thermal activation and hence is equal to the average spacing between the obstacles that are impeding the dislocation motion, and d is the effective size of the obstacles. The activation volume, therefore, yields the information regarding the interaction between the moving dislocations and the radiation-induced defects. It has been shown[33] that the activation volume v^* can be experimentally determined by the relationship

$$v^* = kT \left(\frac{\partial \ln \dot{\epsilon}_p}{\partial \tau} \right)_T \qquad (3)$$

where k is Boltzmann's constant, T is the absolute temperature, $\dot{\epsilon}_p$ is the plastic strain rate, and τ is the applied shear stress. The shear stress τ is taken as one-half of the tensile stress.

In the stress relaxation experiment, the plastic strain rate $\dot{\epsilon}_p$ is determined from the slope of the stress relaxation curve as a function of

---

[33]H. Conrad, "On the Mechanism of Yielding and Flow in Iron," J. Iron Steel Inst. 198, 364 (1961).

stress through the following equation

$$\dot{\epsilon}_p = -\frac{1}{E}\frac{d\tau}{dt}$$

where E is the combined elastic modulus of the specimen and the machine. Thus the activation volume can be determined from the slope of the semi-logarithmic plot of the plastic strain rate vs the shear stress.

When the activation volume is evaluated in this way, it is found to increase very rapidly with decreasing stress. As the stress relaxes towards its asymptotic value the activation volume eventually reaches the value of 1000 b^3. According to a current theory of thermally activated motion of dislocations,[34] the stress dependence of the activation volume may be expressed as

$$v^* = \frac{H_o}{\tau_o}\left[\left(\frac{\tau_o}{\tau^*}\right)^{1/2} - 1\right]$$

where H_o is the activation energy at zero effective stress, τ_o is the flow stress at absolute zero temperature and τ^* is the effective stress or the thermal component of the stress. The effective stress is defined as

$$\tau^* = \tau - \tau_i$$

where τ is the applied stress and τ_i is the long range internal stress. Equation (3) has been tested[35] for irradiated Cu and has been found to be in good agreement with the experimental data.

---

[34] R. L. Fleischer, "Rapid Solution Hardening, Dislocation Mobility, and the Flow Stress of Crystals," J. Appl. Phys. 33, 3504 (1962).

[35] T. J. Koppenaal, "Neutron Irradiation Strengthening in Copper Single Crystals," Phil. Mag. 11, 1257 (1965).

In iron the magnitudes of H_o and τ_o are estimated as[36]

$$H_o = 0.5 \text{ ev}$$

$$\tau_o = 60 \text{ kg/mm}^2.$$

When these values and $v^* = 1000b^3$ are substituted into Eq. (3), it follows that the effective stress at the end of the stress relaxation is given by

$$\tau^* = 5 \times 10^{-3} \text{ kg/mm}^2.$$

Since this value is so small, it is concluded that the asymptotic value of the stress, originally defined as the threshold stress, is equal to the internal stress within the accuracy of the test.

Figure 6.18 shows a plot of the activation volume against the effective shear stress obtained from a Ferrovac-E iron sample irradiated to a dose of 4×10^{18} neutrons/cm^2 ($E > 1$ Mev). The data from the unirradiated sample are also plotted for comparison. The effective shear stress in this plot is the difference between the applied shear stress and the internal stress as measured by the stress relaxation technique. As was pointed out earlier, the activation volume increases quite rapidly with decreasing effective stress. The striking fact is that, for the range of the effective stress normally encountered in room temperature tests, the magnitude as well as the stress dependence of the activation volume is not affected by the irradiation. This result may be compared with that of a recent work on Ferrovac-E iron[37] in which a decrease in

---

[36]H. Conrad, "Yielding and Flow of the b.c.c. Metals at Low Temperatures," p. 476 in The Relation Between the Structure and Mechanical Properties of Metals, Her Majesty's Stationary Office, London, 1963.

[37]F. A. Smidt, "Effects of Irradiation on Thermally Activated Flow in Iron," J. Appl. Phys. 36, 2317 (1965).

[redacted]

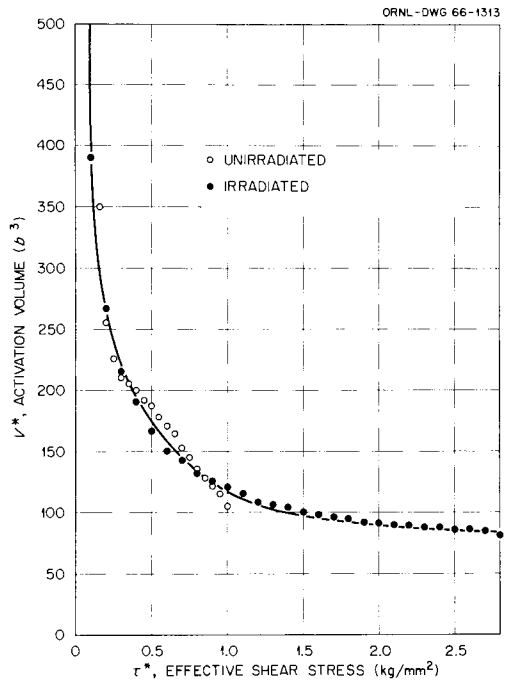

Fig. 6.18. Plot of the Activation Volume vs the Effective Shear Stress in Neutron Irradiated and Unirradiated Ferrovac-E Iron.

the activation volume is observed after neutron irradiation. In a study such as this, the activation volumes are measured at the stress levels corresponding to yield or flow stress. We have found in Ferrovac-E iron that the effective shear stress for yielding in the irradiated sample is greater (by approximately 2 kg/mm^2) than that of the unirradiated sample. This difference in the effective stress can be explained in terms of the difference in the density of mobile dislocations which was reported previously.[32] Since the activation volume decreases rapidly with increasing effective stress, it is expected that the measured activation volume for the irradiated sample would be lower than the unirradiated value. It is to be emphasized that the comparison of the activation volumes should be made at the constant effective stress, and when this is done no difference is found in the activation volumes between the irradiated and unirradiated samples.

To test the validity of the stress relaxation technique, we have performed tensile tests involving a number of samples in which the applied strain rate is held constant for each sample but is varied from

[redacted]

sample to sample. In these tests the strain rate is controlled externally and the corresponding yield stress is measured. In the stress relaxation technique, on the other hand, the strain rate is measured indirectly from the rate of stress relaxation. After measuring the lower yield stress at each level of the applied strain rate, the tensile test is interrupted so as to measure the internal stress, and hence the effective yield stress, by the stress relaxation technique. Figure 6.19 shows a plot of the applied strain rate against the effective lower yield stress obtained from such a series of tests in Ferrovac-E iron. It is noted that the curve can be separated into two straight lines and the slopes m_1 and m_2, as well as the intercept $\rho\mu$, are in good agreement with the corresponding values from the stress relaxation analysis. It may be concluded, therefore, the stress relaxation phenomenon is a true manifestation of the deformation process.

In Fig. 6.20 we have plotted the dependence of the internal stress on the grain size in silicon-iron samples (3.2 wt % Si). The internal stress is measured by the stress relaxation technique, and it refers to the value at zero plastic strain. In the range of grain size studied, the dependence can be adequately described in terms of the $d^{-1/2}$- law.

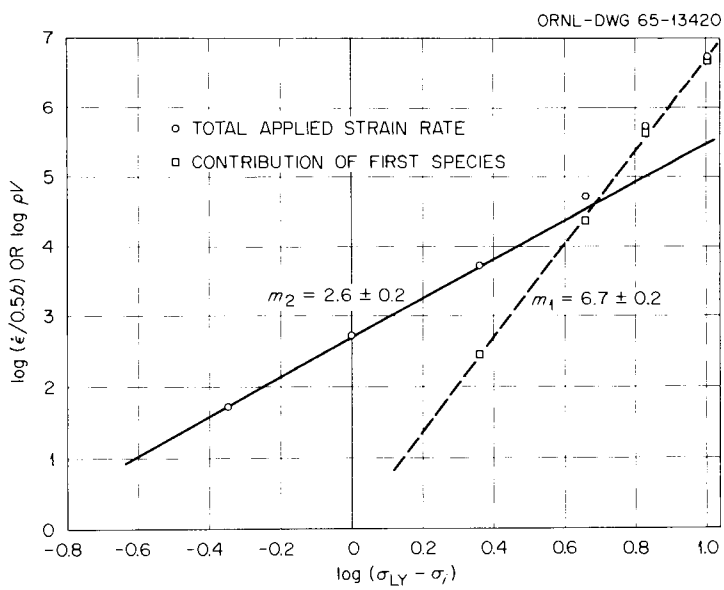

Fig. 6.19. Plot of the Applied Strain Rate vs the Effective Lower Yield Stress for Ferrovac-E Iron.

[redacted]

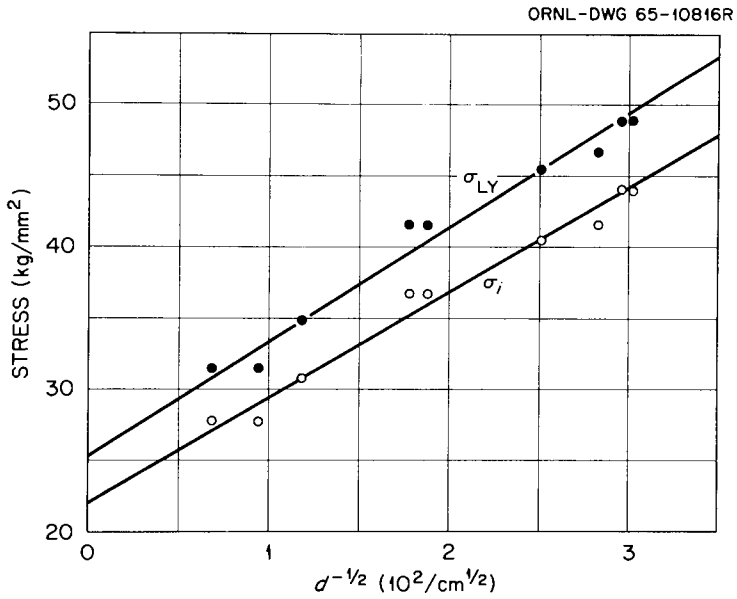

Fig. 6.20. Internal Stress and Lower Yield Stress vs Grain Size in Silicon Iron.

From the intercept of the line through the data points, the internal stress of the unstrained single crystal of silicon-iron is predicted as 22 kg/mm^2.

With this value of the internal stress, we have re-examined the mobility data of Stein and Low[38] on edge dislocations in single crystals of silicon-iron. In Fig. 6.21 we have plotted the velocity of edge dislocations as a function of the effective stress. The effective stress was evaluated by subtracting the internal stress of 22 kg/mm^2 from the applied stress. When the effective stress is plotted in place of the applied stress, the stress dependence of the velocity, m, for edge dislocation is reduced from their value of 35 to approximately 8. This value of m for the edge dislocations agrees quite well with our value of m_1. From Fig. 6.21, the mobility μ for the edge dislocations is found to be

---

[38]D. F. Stein and J. R. Low, Jr., "Mobility of Edge Dislocations in Silicon-Iron Crystals," J. Appl. Phys. 31, 362 (1960).

[39]H. Conrad, "Yielding and Flow of Iron," p. 315 in Iron and its Dilute Solid Solutions, Interscience Publishers, New York, 1963.

[redacted]

[redacted]

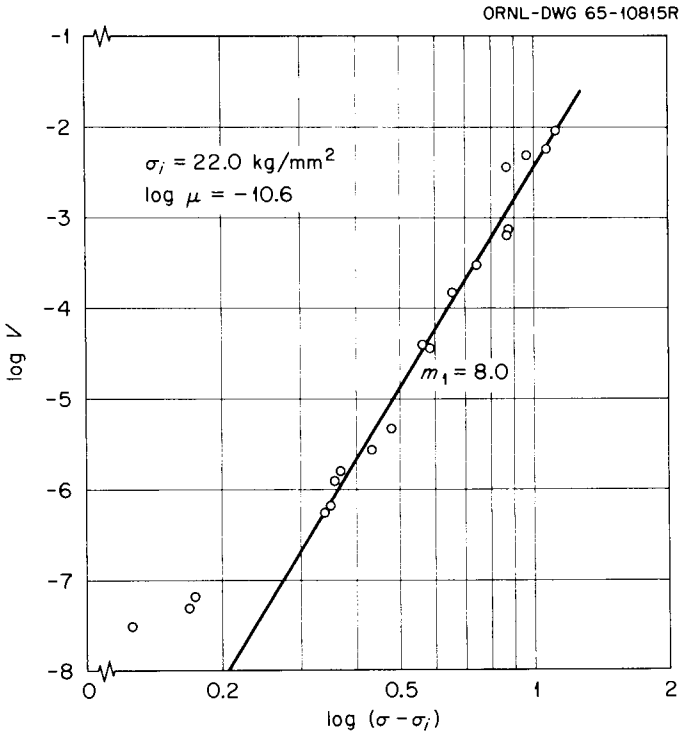

Fig. 6.21. Dislocation Velocity vs Effective Stress in Silicon-Iron at Room Temperature, Obtained From the Etch-Pit Data of Stein and Low.[38]

2.5×10^{-11}. We have found previously in silicon-iron that $\rho\mu = 1.3 \times 10^{-1}$ for the edge dislocations. Therefore, the density of mobile edge dislocations ρ is estimated as

$$\rho = 5.2 \times 10^{9} \text{ cm}^{-2},$$

for the early stage of deformation.

In the present work, a question may be raised as to whether the internal stress would vary appreciably during the relaxation and thus affect the outcome of the analysis. The increase in the plastic strain during a relaxation run was measured with an extensometer and it was found to be less than 5×10^{-4}. This change in strain is expected to have a negligible effect on the dislocation density and the internal stress. From the measured value of the density of mobile dislocations, the average distance traveled by the dislocations during the stress

[redacted]

relaxation is of the order of 400A. This is nearly two orders of magnitude smaller than the size of a cell, which may be taken as the average distance traveled by the dislocations during plastic deformation.

As to the origin of the internal stress, the dislocations that lie nearly parallel to the moving dislocations, as well as the interstitial impurities and their precipitates, are considered to be some of the possible sources.[39] This stress will vary from point to point in the crystal with an average value of zero. The wavelength of its variation is so long that the thermal agitation can not assist the moving dislocations to overcome the stress barriers. The internal stress in the irradiated crystal may be attributed to the presence of the point defects and defect clusters produced by the irradiation. The increase in the internal stress is the major cause of the radiation hardening in iron.

The Preparation and Purification of Single Crystals of Niobium

R. E. Reed*

High Vacuum Electron Beam Floating Zone Refiner

A 5 kilowatt electron beam floating zone refiner which was designed to obtain 1×10^{-10} torr vacuum was recently placed into operation in the Solid State Division of Oak Ridge National Laboratory. The electron beam scanner and power supply was from the EBZ 94 unit of Materials Research Corporation. The specimen chamber and accessory feed-through components are bakeable to 450°C. A fractionating oil diffusion pumping system is used. A more detailed description of the electron beam scanner and the vacuum system is given in the next sections.

A. Vacuum System. The electron beam scanner is contained in a stainless steel bell jar 18 inches in diameter and 20 inches high. Water cooling coils are welded to the outside of the bell jar. A bakeable 4-inch diameter viewing port is positioned about 8 inches above the bottom. The bell jar is mated to a receiver section with a 18 inch diameter Wheeler flange with a copper crush gasket.

---

*Work performed under the Research Materials Program.

The receiver section has ten feed-through ports. Nine of these are equipped with 2-3/4-inch o.d. "conflat" stainless steel flanges. The other port has a 4-1/2-inch o.d. flange of the same design. All feed-through accessories are mounted on the same type of flange and are sealed to the receiver with copper gaskets. All mechanical motion feed-through accessories are of the magnetic rotary type. All electrical feed-through accessories are of the bonded ceramic type. The pressure is measured with a nude, flanged, Bayard-Alpert type ionization gauge inserted into one of the feed-through ports on the receiver.

The receiver is fastened to a 10-inch-diameter Chevron liquid nitrogen baffle using a copper gasket. A 10-inch-diameter stainless steel oil diffusion pump with a conducting cold cap is used in conjunction with this baffle to evacuate the specimen chamber. The pumping speed at the entrance to the receiver section is 1750 liters/sec.

A 4-inch-diameter oil diffusion pump with a conducting cold cap and liquid-nitrogen-cooled baffle is used to back up the larger diffusion pump. The system is roughed with a 425 liters/min. mechanical pump.

A typical operating sequence starts with roughing the system down to about 20 microns pressure using a roughing line that by-passes the 4-inch diffusion pump. After valving out the roughing line, the cooling baffle on the 4-inch diffusion pump is filled with liquid nitrogen. This pump is then turned on and the entire system is pumped down to about 3×10^{-4} torr pressure. The cooling baffle on the 10-inch diffusion pump is then filled. At this stage, the ionization gauge in the specimen chamber reads about 3×10^{-5} torr pressure. The 10-inch diffusion pump is turned on using heating pulses until the pump oil is outgassed, during which the specimen chamber pressure is never allowed to rise above $8\text{-}9 \times 10^{-5}$ torr. The system is then pumped down rapidly to about 8×10^{-8} torr. The total elapsed time at this stage is about 2 1/2 hours. A bake-out oven is then placed over the bell jar and the receiver section. It is baked at 400°C for 16 hours. After cooling to room temperature the pressure in the specimen chamber is about 5×10^{-9} torr.

Using the above procedure and a water-cooled bell jar, we electron-beam floating-zone refined a 4.8mm-diameter niobium rod at about

5-10 $\times 10^{-8}$ torr. It was noticed that after zoning and cooling the rod, the pressure of the specimen chamber dropped to about 2×10^{-9} torr. This suggests that even lower pressures could be attained by zoning the rod many times. This is probably due to lower outgassing rates from the specimen and the electron beam scanner after making a zoning pass.

B. Electron Beam Scanner. The scanner consists of a stationary specimen holder and an electron-beam gun mounted on a traveling stage that moves the gun parallel to the specimen rod axis. Scanning speeds from 2.5 to 46 cm/hr are possible. The total scanning distance is 38cm. The traverse mechanism consists of two ball screws which required no lubrication and have a low degassing rate. The position of the bottom specimen holder is adjusted by one of the magnetic rotary feed-through accessories. The desired zone length can be preset using a limit switch which turns off the electron beam gun and the scanning mechanism at the end of a pass.

The electron beam gun is a work accelerated type with an annular wire filament as the electron source. The gun design consists of grounded tantalum focusing plates 8mm apart, a plate aperture diameter of 14.5mm, and a 23mm-diameter annular filament of 0.51mm diameter tungsten wire.

The power supply consists of two parts, a DC high voltage supply and a filament power supply. The high voltage DC power supply had an output of up to 5kw with voltage variable to 10kv and current to 500ma. The filament power supply was adjustable to supply any combination of voltage and current up to 10 volts and 30 amperes. The emission current in the electron gun is maintained at a preset constant value by controlling the filament power. This unit was designed to be capable of zone-refining specimens with diameters as large as 12.7mm and melting points as high as 3400°C.

C. Initial Results. Initial tests were made using 12.7mm diameter niobium rod obtained from Wah Chang Corporation. About 45cm of one pass zone-refined rod was produced in three trials. Approximately 25cm of this material was single crystal rod. The scanning speeds were about

10cm/hr. The vacuum during zoning was only 1-4 $\times 10^{-7}$ torr due to the large size specimen. The beam voltage used was 7200 volts with an emission current of 235ma. The molten zone length under these conditions was about 10mm. This material was loaned to R. E. Pawel, Metals and Ceramics Division, Oak Ridge National Laboratory, for thin film oxidation studies.

A Ta-15 wt % tungsten alloy was made and zone-leveled using this apparatus. A 6.3mm diameter pure tantalum rod obtained from Materials Research Corporation was slotted with a milling cutter. Pure pyrolytic tungsten sheet of the correct amount to form 15 wt % alloy was placed in the slot. After outgassing the rod by moving the electron beam gun up the rod at a lower power level, the composite specimen was zone leveled at a beam voltage of 6000 volts and a beam current of 150ma. The molten zone was twice moved up and down the rod. The vacuum during the zone-leveling was in the 2-8 $\times 10^{-8}$ torr range. A Ta-15 wt % W alloy single crystal rod about 25cm long resulted from this method. The material was loaned to R. J. Arsenault, Metals and Ceramics Division, Oak Ridge National Laboratory, for basic studies in the plastic deformation of body-centered-cubic metals.

This system is now being used to zone-refine 4.8mm diameter niobium rod obtained from two different material sources. The material obtained will be compared to the same source material zone-refined in a smaller electron beam floating zone refiner at higher pressures.

Purification of Niobium by Electron Beam Floating Zone Refining

Niobium metal obtained from Wah Chang Corporation was refined in an electron beam floating zone module (Model No. 4-EBZ-6000) purchased from Materials Research Corporation. The composition of the starting material has been reported previously.[40] Extensive chemical analyses

---

[40]R. E. Reed and M. S. Wechsler, Radiation Metallurgy Section Solid State Division Progr. Rept. Aug., 1965, ORNL-3878, p. 38.

were conducted in order to follow the purification of the metal during this treatment. This section will describe the zone refining procedure, the sampling sequence, and the results obtained from various types of chemical analyses.

A. Zone Refining Procedure. Cold swaged (4.8mm diameter) niobium rod was electron beam floating zone refined at a zoning speed of about 10cm/hr. Rods from the same starting material were given from one to twelve zone passes. The specimen chamber consisted of a glass bell jar and aluminum receiver section resting on a stainless steel base plate. Viton O-rings and gaskets were used in all the vacuum seals. A 4-inch oil diffusion pump with a water baffle and liquid nitrogen cold trap gave a pumping speed of about 150 liters/sec at the entrance to the specimen chamber. The base pressure obtained in the bell jar was usually 2×10^{-7} torr. The pressure during zoning ranged from $1\text{-}2 \times 10^{-6}$ torr for the first zoning pass to about $3\text{-}5 \times 10^{-7}$ torr after about the fourth pass. This was attributed to decreasing amount of outgassing from the specimen, scanner, and specimen chamber as the zone refining progressed. The electron gun design was essentially the same as that used in the high vacuum electron beam zone refiner described earlier. With this configuration, the molten zone was about 3.5mm long at a power level of 280 watts.

B. Sampling Sequence. The as-zoned rods were first prepared for resistance ratio measurements along the zoned length. Lengths of 0.51mm diameter platinum wire about 3cm long were beaded on one end by melting it in a small gas torch flame. The beaded end of these wires were then spot welded to the zoned rod using a very light contact pressure. Copper wire current and voltage leads were then soft soldered to the platinum taps. The position of these taps is shown in Fig. 6.22 which is a schematic drawing of a typical as-zoned rod. Since niobium has a superconducting transition temperature of 9.2°K, the low temperature resistance measurements were made in a liquid hydrogen bath (20.2°K). The high temperature resistance measurements were made in a mineral oil bath at room temperature (296°K). The resulting resistance ratios taken along

[redacted]

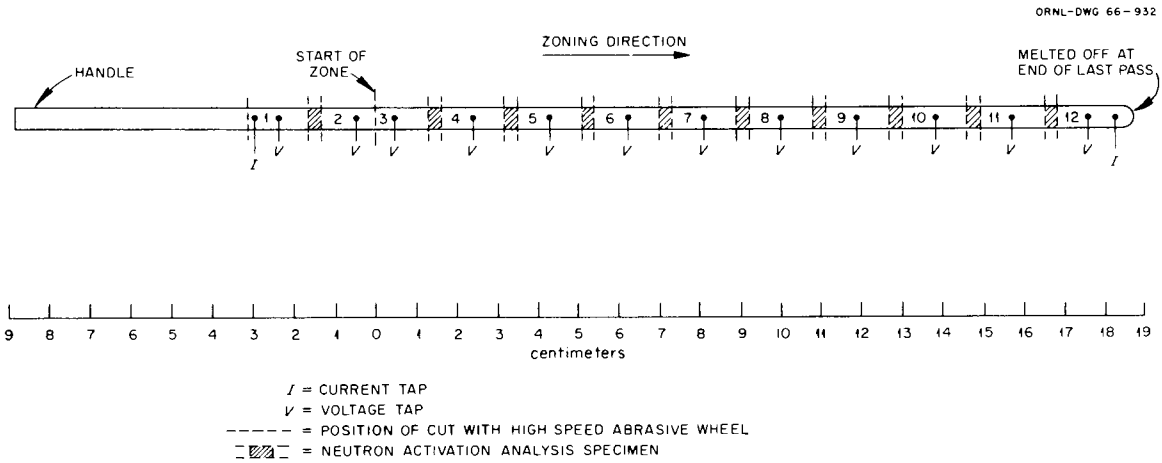

Fig. 6.22. Schematic of a Typical Zone Refined Niobium Rod Showing Sampling Procedure for Chemical Analysis. Note: Spark source mass spectrometric, Leco conductometric, and vacuum fusion analyses were made on the numbered sections as described in the text.

the zoned length on 1, 2, 4, 6, and 12 pass rods have been reported previously.[41]

The rod was next cut into sections as shown in Fig. 6.22. The cuts were made using a high speed abrasive cut-off wheel with water coolant. Small discs 3mm long, 4.8mm in diameter, were cut from the center of each section which had a resistance ratio measurement. Each remaining section (numbered in sequence in Fig. 6.22) was beveled on the end toward the top of the rod where it had been melted off at the end of the last pass. All of the sections were then given a deep chemical polish in a solution of nitric acid (70%) and hydrofluoric acid (48%) mixed in the proportions of 3:2.

The discs were used for neutron activation analyses for Ta and W impurity. The other sections were first used to get spectrographic analyses for all metallic impurities using a spark source mass spectrometer (Associated Electrical Industries Model MS7). These analyses were

---

[41]R. E. Reed and M. S. Wechsler, Radiation Metallurgy Section Solid State Division Progr. Rept. Aug., 1965, ORNL-3878, p. 39.

[redacted]

taken by striking an arc between adjoining sections taken from the rod. Thus mass spectrographic analyses were taken at essentially the same position as the neutron activation analyses. Next, each section was again chemically polished and approximately two-thirds of each section used for a carbon analysis and the other third for oxygen, nitrogen, and hydrogen analyses. Carbon content was measured by the Leco conductometric method. Oxygen, nitrogen, and hydrogen contents were determined using the vacuum fusion technique with a platinum bath at 2000°C.

C. Results of the Chemical Analyses.

(1) Metallic Impurities

Neutron activation analyses for Ta and W gave the results tabulated in Table 6.3. For all rods tested, there was no significant variation of

Table 6.3. Neutron Activation Analyses for Ta and W in Niobium (Weight ppm)

	1 Pass		6 Pass		12 Pass	
Distance from start of zone (cm)	Ta	W	Ta	W	Ta	W
Handle	363	224	364	216	358	232
1.5	369	231	384	243	377	260
3.4	365	221	360	216	369	244
5.3	372	230	370	225	359	238
7.2	366	224	365	220	369	242
9.1	374	230	373	267	362	240
11.0	367	227	367	227	363	239
12.9	368	228	362	317	367	235
14.8	357	221	382	232	365	238
16.7	372	230	366	223	378	250
Mean ($\bar{X}$)	367	227	369	229	367	242
Std. Dev. (σ)	4.7	3.7	7.7	15.1	6.5	7.7

the tantalum or tungsten content along the zone length. In addition, there was no difference in tantalum content as a function of number of passes. The arithmetic mean ($\bar{X}$) of the tantalum contents reported for all discs from each rod was 367, 369, and 367 wt ppm for 1, 6, and 12 pass rods respectively. However, there is some indication of a slight tungsten impurity increase as a function of number of passes possibly due to contamination from the electron gun tungsten filament. For this case, the arithmetic mean ($\bar{X}$) for tungsten content was 227, 229, and 242 wt ppm for 1, 6, and 12 pass material respectively. Thus there was about a 6% increase in the amount of tungsten in the zoned refined rod after 12 passes.

The data obtained by visual reading of the plates from the spark source mass spectrometer did not show a significant variation in the amount of any metallic impurity along the zoned length. However, some of these impurities did decrease with increasing number of passes. The results are summarized in Table 6.4. The weight parts per million figures that are listed in this table were obtained by taking a mean value by visual examination of all the plates taken on a particular zoned rod. The amounts of cobalt, nickel, copper, and zirconium impurity have decreased as a result of zone refining. It is important to note that most metallic impurities other than Ta and W were under 5 wt ppm after zone refining the rod one pass.

These results indicated that most of the removal of metallic impurities was by evaporation since there was no significant variation of metallic impurity content along the zoned length. However, the metallic impurity content did decrease with increasing number of passes. Tantalum and tungsten were exceptions to this. The amount of these two metallic impurities did not vary along the zoned length and tantalum did not decrease with increasing number of passes. In addition, tungsten increased slightly as the number of passes increased probably due to contamination from the tungsten filament in the electron gun. Thus, it is important to obtain niobium starting material with low Ta and W contents for electron beam floating zone refining.

[redacted]

Table 6.4. Metallic Impurities in Niobium as Determined by Spark Source Mass Spectrometry (Weight ppm)

Element	Starting Material	Zone Refined Niobium		
		1 pass	6 pass	12 pass
Al	15	0.3	1	3
Au	< 0.1			
B	0.1	0.1	0.1	0.1
Ca	< 1	0.4	< 1	< 1
Cd	< 2			
Co	1	0.06	0.02	0.05
Cr	3	0.7	1	0.7
Cu	30	0.1	0.1	1
Fe	10	1	2	6
Hf	15	5	5	4
Mg	5			
Mn	1	0.2	0.2	0.5
Mo	3	6	3	1
Ni	5	0.3	0.4	0.3
Pb	< 10			
Sn	< 5			
Ta	400	400	400	400
Ti	30			
V	< 1			
W	300	300	300	300
Zr	140	20	10	4

[redacted]

(2) Interstitial Impurities

The carbon analyses made by the Leco conductometric method showed that there was no significant variation of carbon content along the zone refined rods. Table 5 lists these results. However, as the number of zoning passes increased the carbon content increased. The arithmetic mean of the carbon content in the zoned section of the 1, 6, and 12 pass rod was 11, 15, and 45 wt ppm respectively. This indicated that the gaseous environment in the specimen chamber probably contained appreciable partial pressures of H_2, H_2O, CO_2, and CH_4. These gases have been reported by Inouye[42] to be the major components of the residual gas in vacua between 10^{-6} and 10^{-8} torr in a system pumped with oil diffusion and mechanical pumps. A proper ratio of these gases could result in a carburization reaction which would increase the carbon content during zone refining. Possible sources of these gases in the zone refiner are: (a) outgassing of viton O-rings in system, (b) backstreaming gases from pumping system and (c) formation during zoning by reaction of hydrogen and/or oxygen with organic contaminants.

The vacuum fusion analyses for hydrogen showed no significant variation of hydrogen content either along the zoned length of individual rods or among zoned rods which were zone refined 1, 6, or 12 passes. The arithmetic mean ($\bar{X}$) for all analyses was 4.0 wt ppm with a standard deviation of 1.1 wt ppm.

The vacuum fusion results for oxygen and nitrogen contents in the zone refined niobium rods are best summarized in Figs. 6.23 and 24. Figure 6.23 is a plot of the oxygen content in wt ppm as a function of distance along the rod for 1, 6, and 12 pass material. There was a marked drop of oxygen content from $\bar{X}$ = 116 wt ppm in the handle to a level of $\bar{X}$ = 30 wt ppm for the one pass rod. The arithmetic mean ($\bar{X}$) of the oxygen contents in the zoned region of the 6 and 12 pass rods were 25

---

[42]H. Inouye, Contamination of Refractory Metals by Residual Gases in Vacuums Below 10^{-6} torr, ORNL-3674, September 1964.

[redacted]

Table 6.5. Leco Conductometric Analyses for Carbon in Niobium (Weight ppm)

Distance from start of zone (cm)	1 pass	6 pass	12 pass
	11	21	29
Handle	9	14	57
0.7	8	19	26
2.5	10	40	45
4.3	8	11	42
6.2	9	16	53
8.1	19	9	54
10.0	9	9	52
11.9	10	14	38
13.8	9	15	48
15.7	13	9	44
17.6	11	12	
Arithmetic Mean of carbon contents in the zoned region	11	15	45
Std. Dev.	3.2	8.8	8.3

[redacted]

[redacted]

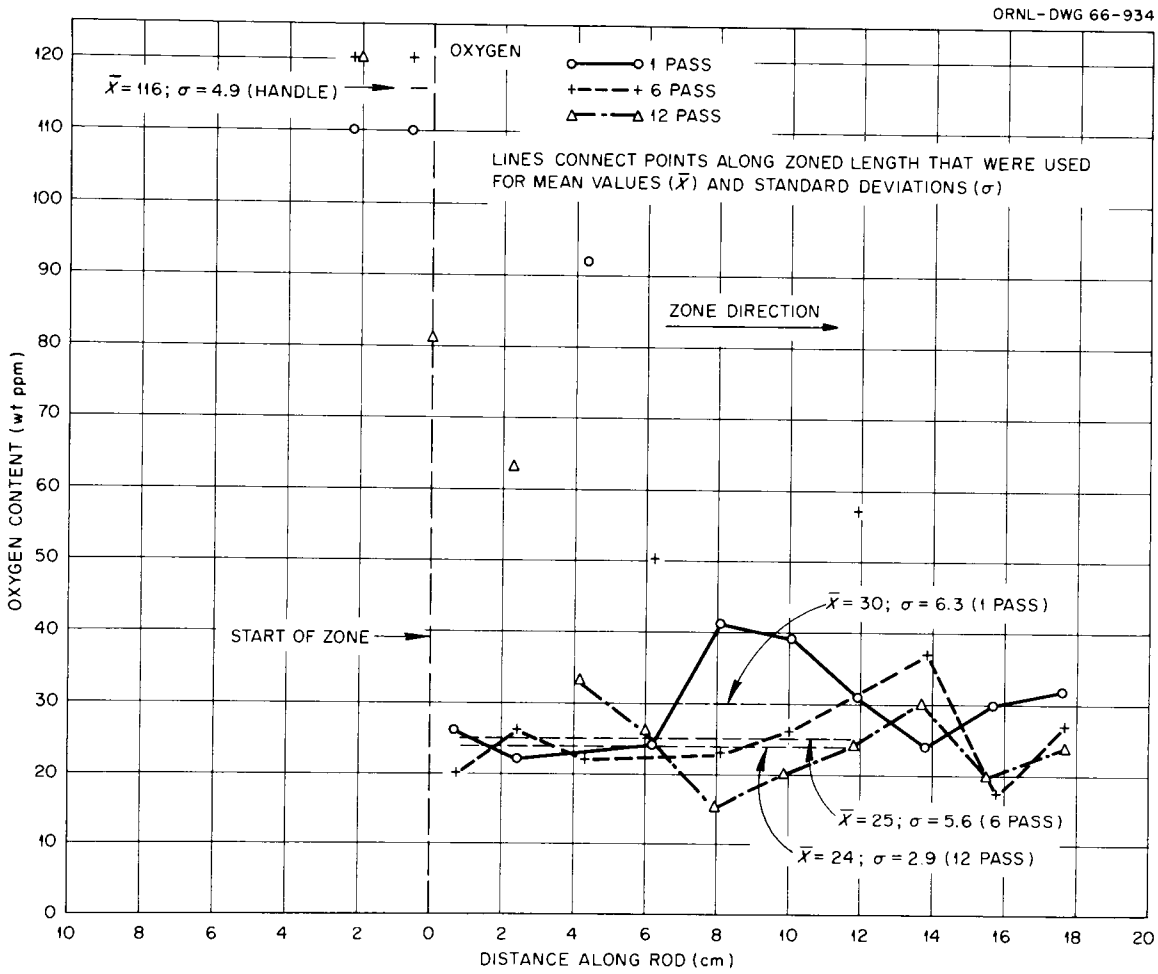

Fig. 6.23. Oxygen Content in Weight ppm as a Function of Distance Along the Zoned Rod for 1, 6, and 12 Pass Material.

[redacted]

[redacted]

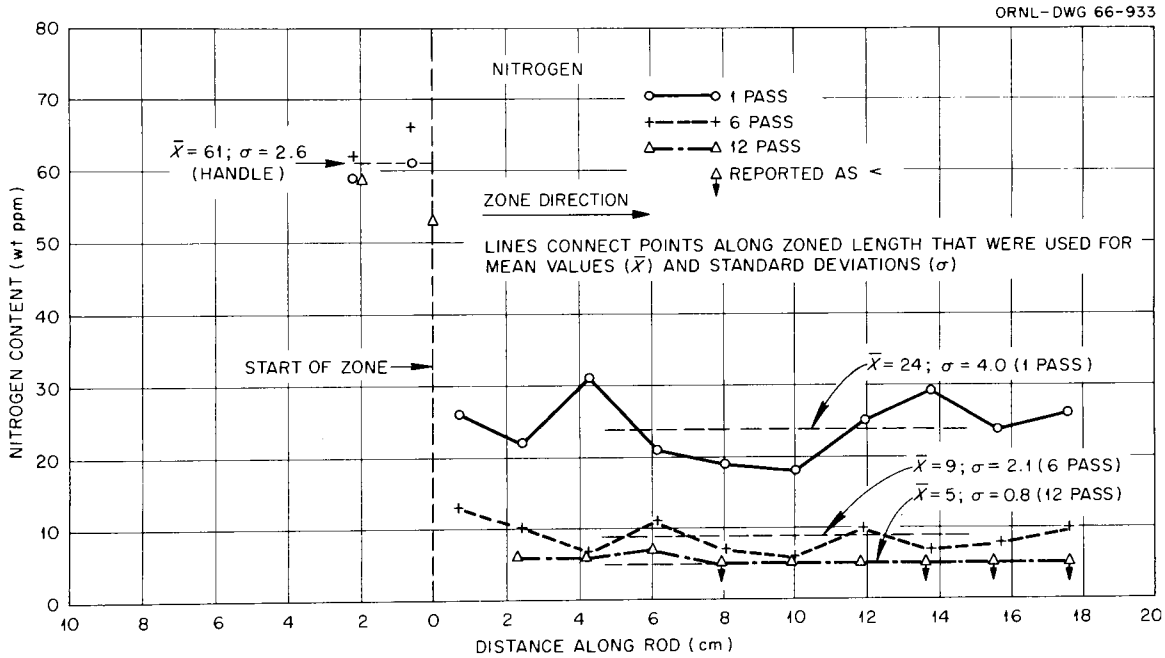

Fig. 6.24. Nitrogen Content in Weight ppm as a Function of Distance Along the Zoned Rod for 1, 6, and 12 Pass Material.

and 24 wt ppm respectively. There was such scatter in the results that no variation in oxygen content along the zone length could be found. In fact, some of the oxygen analyses were not used in calculating the arithmetic means since they were so far from the general trend of the curves. However, there was the indication that the first pass greatly reduced the oxygen content and subsequent zoning passes reduced this oxygen level only slightly.

The nitrogen content analyses are shown in Fig. 6.24. In this figure, the nitrogen content in wt ppm is plotted versus distance along the zoned rod for 1, 6, and 12 pass material. This impurity behaved in a manner similar to that of oxygen. The first zoning pass decreased the nitrogen content from $\bar{X}$ = 61 wt ppm in the handle to $\bar{X}$ = 24 wt ppm. Increasing the number of passes to 6 and 12 decreased the nitrogen content to $\bar{X}$ = 9 and 5 wt ppm respectively. In this case, increasing the number of passes decreased the nitrogen content quite clearly although the

[redacted]

[redacted]

scatter still prevented assigning a significant variation of nitrogen along the zone length.

Pasternak[43] has extensively studied the oxidation and nitridation of niobium in vacua in the 10^{-6} to 10^{-9} torr range. For the case of nitrogen, he proposed that adsorption and desorption are the slowest steps in the overall sorption mechanism and thus determine the observed kinetics. The proposed reaction steps were:

$$\frac{1}{2} N_2 \text{ (gas)} + \triangle = N\triangle$$

$$N\triangle + \square = N\square + \triangle$$

$$\frac{1}{2} N_2 + \square = N\square$$

The symbols $\triangle$ and $\square$ represent surface and interstitial sites respectively in the niobium. At equilibrium the following relationship holds:

$$C_e = \alpha P^{1/2} \exp\left[\Delta H_{soln}/RT\right]$$

where C_e = equilibrium concentration of nitrogen in niobium (atom %)

P = partial pressure of nitrogen in equilibrium with metal (torr)

ΔH_{soln} = heat of solution

α = entropy factor ($torr^{-1/2} \cdot$ atom %)

R = gas constant

T = temperature

---

[43] R. A. Pasternak, High Temperature Oxidation and Nitridation of Niobium in Ultra High Vacuum, Stanford Research Institute Report SRIA 132, Nov., 1964.

[redacted]

From the experimental kinetics of adsorption and desorption and assuming the above reaction stops, Pasternak was able to obtain values of α and ΔH that agreed well with the values obtained under equilibrium conditions. These values were: $\alpha = 1.2 \times 10^{-5}$ torr$^{-1/2}$ · atom %; ΔH = 53,500 calories.

If adsorption and desorption is the rate controlling step in determining the nitrogen content in zone refined niobium, the above equation shows that it is important to have a low partial pressure of nitrogen in the system. Also, if the partial pressure of nitrogen is expected to have higher levels in local regions e.g. within the electron gun enclosure, then it would be best to keep the niobium in this region at as high a temperature as practicable.

In the oxygen-niobium system, Pasternak also found the same general sticking probabilities for oxygen on niobium below 1000°C as for nitrogen. However, at higher temperatures in addition to adsorption and desorption, two additional processes apparently occur which result in high "apparent sticking probabilities." The first reaction is the dissociation of the oxygen molecule on the hot surface followed by irreversible sorption of the oxygen atoms on a cold surface in the system. The second reaction is the formation of NbO at the hot niobium surface followed by the evaporation of the NbO molecule from the surface to a wall of the system.

Again it is apparent that a low partial pressure of oxygen in the system is very important. However, the presence of the competing reactions in addition to the sorption process for the case of oxygen suggests a method of purification. This method would consist of heating niobium at very high temperatures in a good dynamic vacuum with low partial pressures of nitrogen and oxygen. This would reduce the equilibrium concentration (C_e) of both impurities to the lowest practical value. In addition, do this in a cold wall system such that the hot specimen can "see" the wall. Thus the competing reactions for oxygen would result in the deposition of oxygen atoms and NbO molecules irreversibly on the cold

wall. Taylor and Christian[44] used essentially this treatment by resistance heating a 3mm diameter zoned refined niobium rod ~ 2400°C in ~ 1 × 10^{-8} torr vacuum. This treatment improved the resistance ratio (R_{300}/R_{20}) of the as-zoned rod from ~ 100:1 to ~ 2000:1. It is suggested here that this improvement was due largely to the removal of oxygen by the mechanism above. This type of experimental technique will also be investigated in the Research Materials Program at ORNL.

The chemical analyses reported here on the zone refined niobium rod indicate that very little purification was due to movement of impurities by the zone refining action. Instead, most metallic impurities were reduced by evaporation. Tantalum and tungsten were exceptions to this in that there was no significant reduction in the content of either impurity. In fact, tungsten showed a 6% increase at the end of 12 passes probably due to contamination from the electron gun tungsten filament. Interstitial carbon content increased during zone refining possibly due to a carburization reaction occurring among the residual gases in the vacuum environment. The hydrogen content showed no significant change as a result of zone refining. Oxygen and nitrogen levels in the starting material were greatly lowered by the first pass made during zone refining. Subsequent zoning passes had a smaller effect but the chemical analyses did indicate a decreasing oxygen and nitrogen content with increasing number of passes. This was attributed to a lower partial pressure of oxygen and nitrogen in the vacuum environment as zone refining proceeded. The total pressure did decrease with increasing number of passes. Adsorption and desorption of nitrogen at the hot niobium surface was suggested to be the rate controlling mechanism for nitrogen purification during zone refining. For oxygen, the additional reactions of dissociation of the oxygen molecule and the formation of NbO on the hot niobium surface with subsequent deposition of oxygen atoms and NbO on cold surfaces in the system also play an important role in the purification process.

---

[44]G. Taylor and J. W. Christian, Acta Met. 13, 1216 (1965).

[redacted]

Examination of the Perfection of Niobium Single Crystals Using Borrmann Topography

R. E. Reed H. D. Guberman
T. O. Baldwin*

Preliminary studies on the perfection of single-pass niobium single crystals have shown that average dislocation densities of 10^4 to 10^5 lines/cm^2 can be produced using the electron-beam floating-zone technique. This report will describe some results obtained using anomalous x-ray transmission (Borrmann) topographs to examine the substructure of these crystals.

Niobium single crystals 4.8mm in diameter and 175mm long were grown using the electron-beam floating-zone technique described in the previous section. Most of the crystals studied thus far were single-pass rods seeded such that the rod axis was near a [011] direction. Sections 25mm long were cut from the as-grown single crystal rods by means of a high-speed abrasive cut-off wheel. Parallel flats about 1.0 - 1.5mm apart were spark cut along the [011] growth axis such that either the 110, 200, or 211 planes were perpendicular to the flats. Next, the specimen was chemically polished until the thickness was about 0.5mm. The orientation, shape, and dimensions of these specimens after chemical polishing are shown in Fig. 6.25.

Borrmann topography has recently been shown to be a powerful tool for the examination of defects in nearly perfect copper crystals.[45] These same techniques were applied to the zone refined niobium crystals. This is the first known report of anomalous x-ray transmission through niobium. Using molybdenum K_α radiation with a camera described recently,[46] Borrmann topographs were obtained using 110, 200, and 211 reflections from these crystals ranging in thickness up to 1mm ($\mu t \sim 15$). The best topographs were obtained for crystals about 0.5mm thick.

---

*Crystal Physics Section, Solid State Division, Oak Ridge National Laboratory.

[45]F. W. Young, Jr., F. A. Sherrill, and M. C. Wittels, J. Appl. Phys. 36, 2225 (1965).

[46]F. W. Young, Jr., T. O. Baldwin, A. E. Merlini, and F. A. Sherrill, Advances in X-Ray Analysis, Vol. 9, Plenum Press, New York, 1966.

[redacted]

[redacted]

ORNL-DWG 66-515

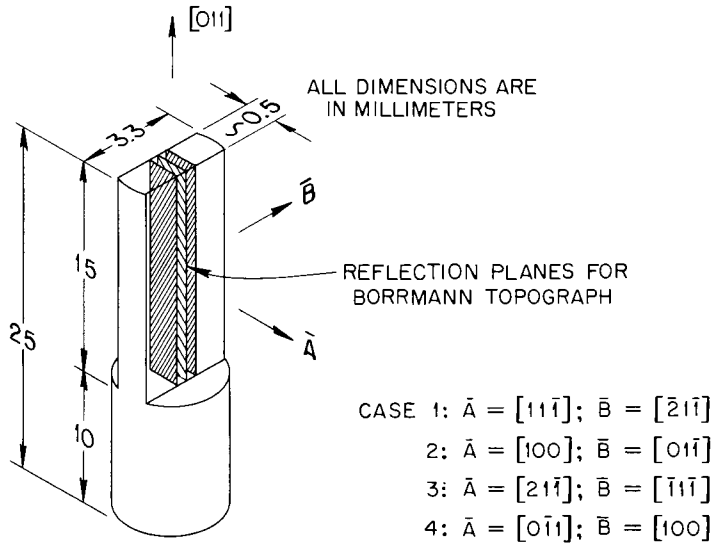

Fig. 6.25. Schematic of Niobium Single Crystal Specimen Used for Anomalous X-Ray (Borrmann) Topography After Spark Cutting and Chemical Polishing.

Anomalous x-ray transmission as it is applied to x-ray topography is best explained using Fig. 6.26 [which was borrowed from reference (46)]. Here, an x-ray beam is incident at the Bragg angle with respect to crystallographic planes which are normal to the crystal surface. For a nearly perfect crystal, two standing wave fields for each polarization direction of the incident radiation are generated inside the crystal. One wave field has nodes at the atomic planes and is transmitted almost undiminished in intensity, while the other wave field has antinodes at the atomic planes and is highly absorbed. If the crystal is thick ($\mu t \sim 10$ or greater), the net energy flow is very nearly parallel to the diffraction planes, and only the wave field with polarization perpendicular to the plane of incidence and with nodes at the atomic planes is transmitted with appreciable intensity. At the exit surface, this wave field splits into two beams of nearly equal intensity. These will be denoted as the anomalously transmitted beam T and the anomalously reflected beam H. The x-ray beam T has the same direction as the incident or direct beam D, but is displaced toward H a distance which is proportional to the crystal thickness. Whenever the lattice is disturbed from its perfect periodicity,

[redacted]

[redacted]

ORNL-DWG 65-2215R

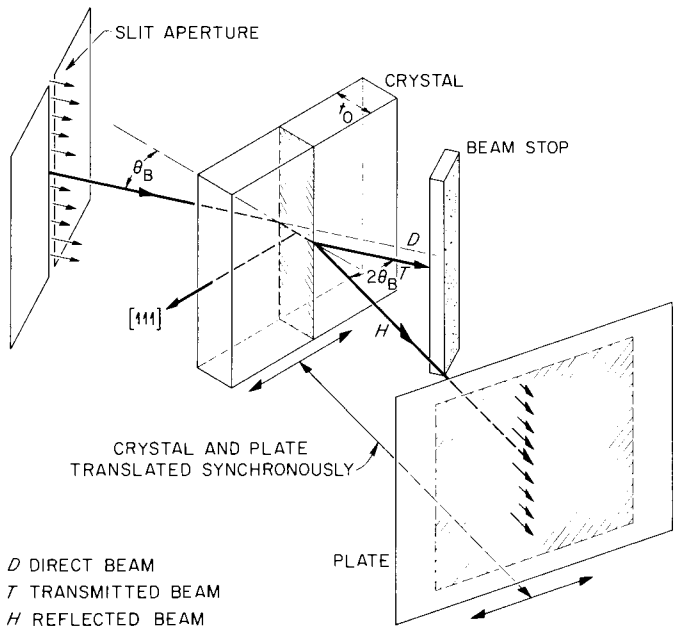

Fig. 6.26. Schematic of the Experimental Arrangement for obtaining a Borrmann Topograph. Stereo topographs are taken by rotating the crystal about the reflecting plane pole ([111] axis in this example for copper taken from reference 46).

such as is the case for dislocations and other imperfections, the intensity of both beams in Borrmann transmission is normally reduced. Regions of reduced intensity or white images of the imperfections will then appear on a photographic plate placed near the exit surface of the crystal. Examples of these topographs are given in Figs. 6.27 and 6.28.

Etch pitting observations resulted in dislocation densities of 1-4 $\times$ 10^{-4} cm^{-2}. This was near the upper limit for the occurrence of anomalous x-ray transmission. Thus, the occurrence of Borrmann transmission verified the etch pitting results. In order to attempt to reduce the dislocation density in the as-prepared Borrmann specimen, a few samples were annealed at 2000°C for 12 hours in 2-5 $\times$ 10^{-7} torr vacuum. Figure 6.27 represents one of the samples before and after annealing. The dislocation density in the annealed crystal is much more uniformly distributed and the anomalously transmitted intensity is higher in the annealed sample. The misorientation about the growth axis [011] was measured for this sample

[redacted]

[redacted]

PHOTO 83380

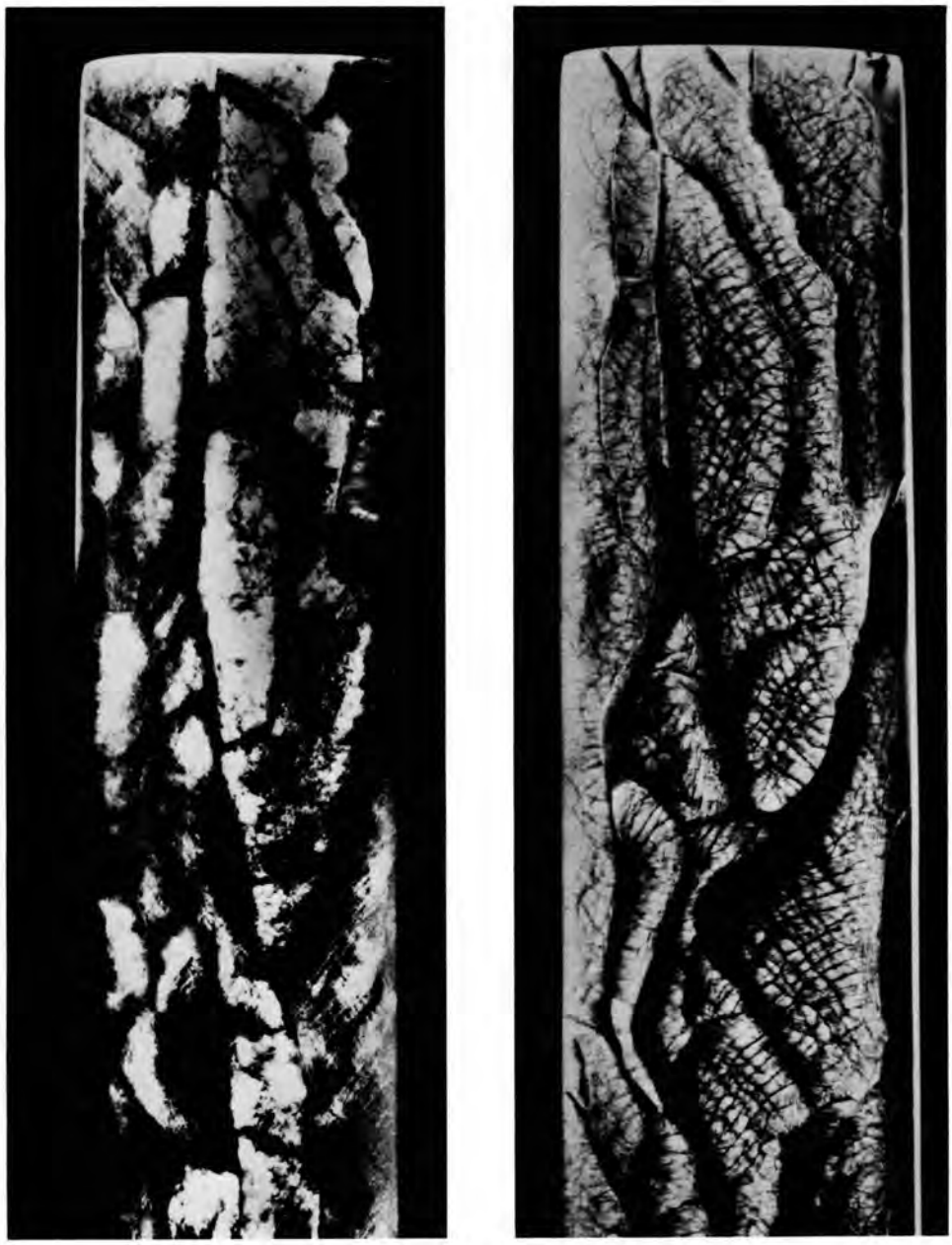

1 mm

Fig. 6.27. Borrmann Topographs of a Niobium Single Crystal Using MoK_{α} Radiation from the (200) Reflection: (a) as-grown; (b) annealed at 2000°C for 12 hr in 2–5 × 10^{-7} torr vacuum. Dark lines represent regions of reduced x-ray intensity.

[redacted]

PHOTO 83381

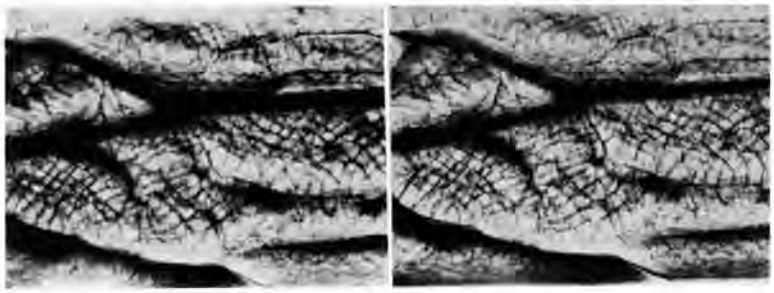

Fig. 6.28. A Stereo-Pair Borrmann Topograph of Specimen Shown in 3(b). This figure can be viewed with two converging lens separated by about 6.5cm held approximately 13cm from the page.

using a double crystal spectrometer and the largest sub-boundary misorientation is about 30 seconds of arc. The divergence of the incident beam for the x-ray topograph is about 180 seconds; thus all of the sample diffracts simultaneously in the topographs. Some of the original substructure remains in the annealed sample. The grid network in the annealed specimen has not yet been identified in this sample and is not yet known to be representative of annealing in these samples.

In order to further examine this grid network, a stereo pair of x-ray topographs was taken using the procedure described by Young et al.[46] This is shown as Fig. 6.28. Examination of this stereo pair results in the following observations.

(a) The grid network appears to lie nearer the top and bottom surfaces as opposed to being randomly distributed throughout the sample although it was difficult to determine the exact position.

(b) Single dislocations that intersected the surface were approximately perpendicular to the surface as would be expected from image force criteria.

(c) In some instances, sections of subgrain boundaries could be resolved into a grid network of dislocations. This is consistent with the double crystal spectrometer data that showed most of the subgrain misorientation to less than 30 seconds of arc.

In summary, it is possible to grow niobium single crystals of relatively high perfection using the electron beam floating zone technique. For the first time, anomalous x-ray transmission topographs have been obtained for niobium single crystals. It was shown that Borrmann topography can be a powerful method to evaluate the perfection of single crystals.

Dislocation Etch Pits in Niobium

H. D. Guberman

Utilizing the techniques and material described in the previous progress report,[47] further effort was directed toward obtaining more substantive evidence of the dislocation nature of the pits which have been observed in niobium. This has been accomplished by two methods described below.

First, generally good agreement has been found between the theoretical expression relating the dislocation densities in three intersecting tilt boundaries and observations of such boundaries. This expression has been given by Amelinckx[48] as:

$$\sum_i \rho_i/(\cos \phi_i + \sin \phi_i) = 0$$

where ρ_i are the densities of dislocations measured from the etch pit patterns and ϕ_i are the angles between the directions of the boundaries and the <110> directions. An example is shown in Fig. 6.29 which represents the intersection of three boundaries in a plane within 4° from (112) in an

---

[47]H. D. Guberman, "Dislocation Etch Pits in Niobium," Radiation Metallurgy Section Solid State Division Progr. Rept. Aug., 1965, ORNL-3878, p. 49.

[48]S. Amelinckx, p. 24 in The Direct Observation of Dislocations, (F. Seitz et al., eds.), Academic Press, New York, 1964.

PHOTO 82966

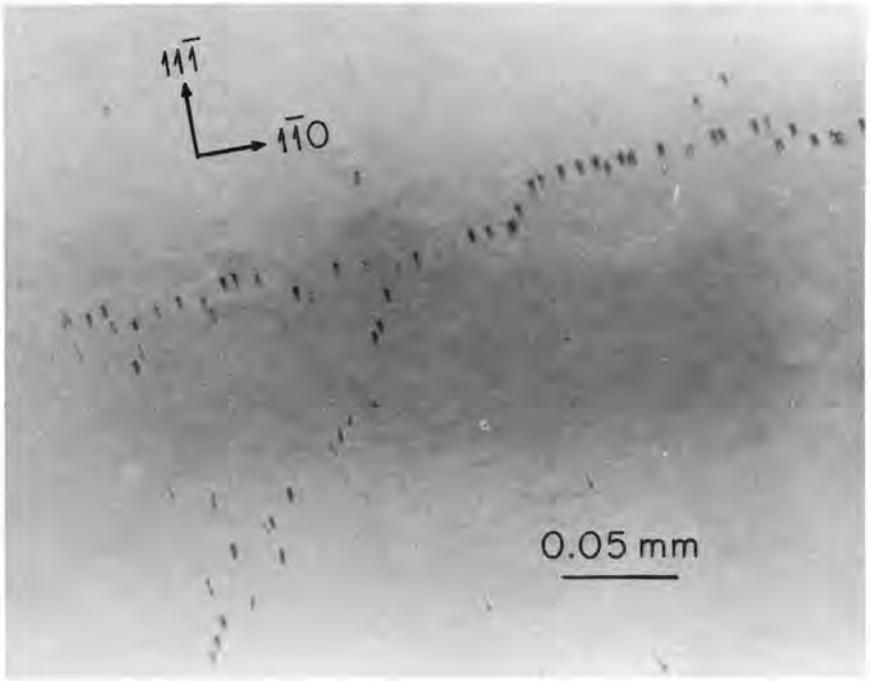

Fig. 6.29. Intersection of Three Boundaries on a Plane Near (112).

as-grown single crystal of niobium. As shown in Table 6.6, when reasonable estimates are made of the boundary directions and pit densities, close agreement with the above expression is found.

This analysis is based upon the assumption that the boundaries are tilt boundaries which, however, may not be true. The second method relies upon the direct comparison between etch pit patterns and an x-ray topograph.

The topograph was produced by the Berg-Barrett technique[49] which displayed features that could only be due to small angle boundaries on the identical surface examined by etch pits. It was possible to make a 1:1 comparison over about 85% of the extent of the sub-boundaries present. As is seen in the three pairs of photographs in Fig. 6.30, features of the etch-pit patterns can be correlated with the structure seen in the Berg-Barrett topographs.

---

[49]S. Amelinckx, p. 90 in The Direct Observation of Dislocations, (F. Seitz, et al., eds.), Academic Press, New York, 1964.

Table 6.6. Parameters Associated with Intersecting Sub-Boundaries

	ρ_i (mm^{-1})	$\cos \phi_i$	$\sin \phi_i$	ρ_i (mm^{-1}) $\cos \phi_i + \sin \phi_i$
1)	110	-1.00	0.00	-110
2)	70	-0.707	-0.707	- 49
3)	150	1.00	0.00	150
				Sum = -9

Note: The average linear densities were determined over a greater area than shown in Fig. 6.29.

From the foregoing one may conclude that the etch pits produced in the material under study by the etchant described earlier are associated with dislocations.

Since the sample material under study was fashioned into suitable shapes by a spark erosion process, it was deemed necessary to assess the degree and depth of penetration of such damage. This was accomplished utilizing the etch-pit technique. Surfaces were produced using the "Servomet Spark Machine" from Materials Research Ltd., Cambridge, England. A copper cutting tool was used with kerosene as the dielectric fluid.

In this process, material erosion occurs at a rate determined by the energy and frequency of the electrical discharge. The spark rate was 60 kc/s and the nominal maximum energy per discharge was about 1.6×10^4 ergs. However, observation of the discharges on an oscilloscope indicated that about 20% of the discharges were about 1.1×10^4 ergs each with the remainder about 3.3×10^3 ergs. Laue x-ray patterns of the eroded surface taken immediately after the spark-erosion process showed evidence of a thin disturbed layer of material. A measurement of the as-cut surface roughness by means of the Taly-Surf instrument indicated that the maximum peak-to-valley distance was about 8.5×10^{-4}cm. Furthermore, this amount represents the minimum which must be removed before it is possible to observe dislocation pits on a relatively smooth surface. Chemically polishing away

[redacted]

PHOTO 82781

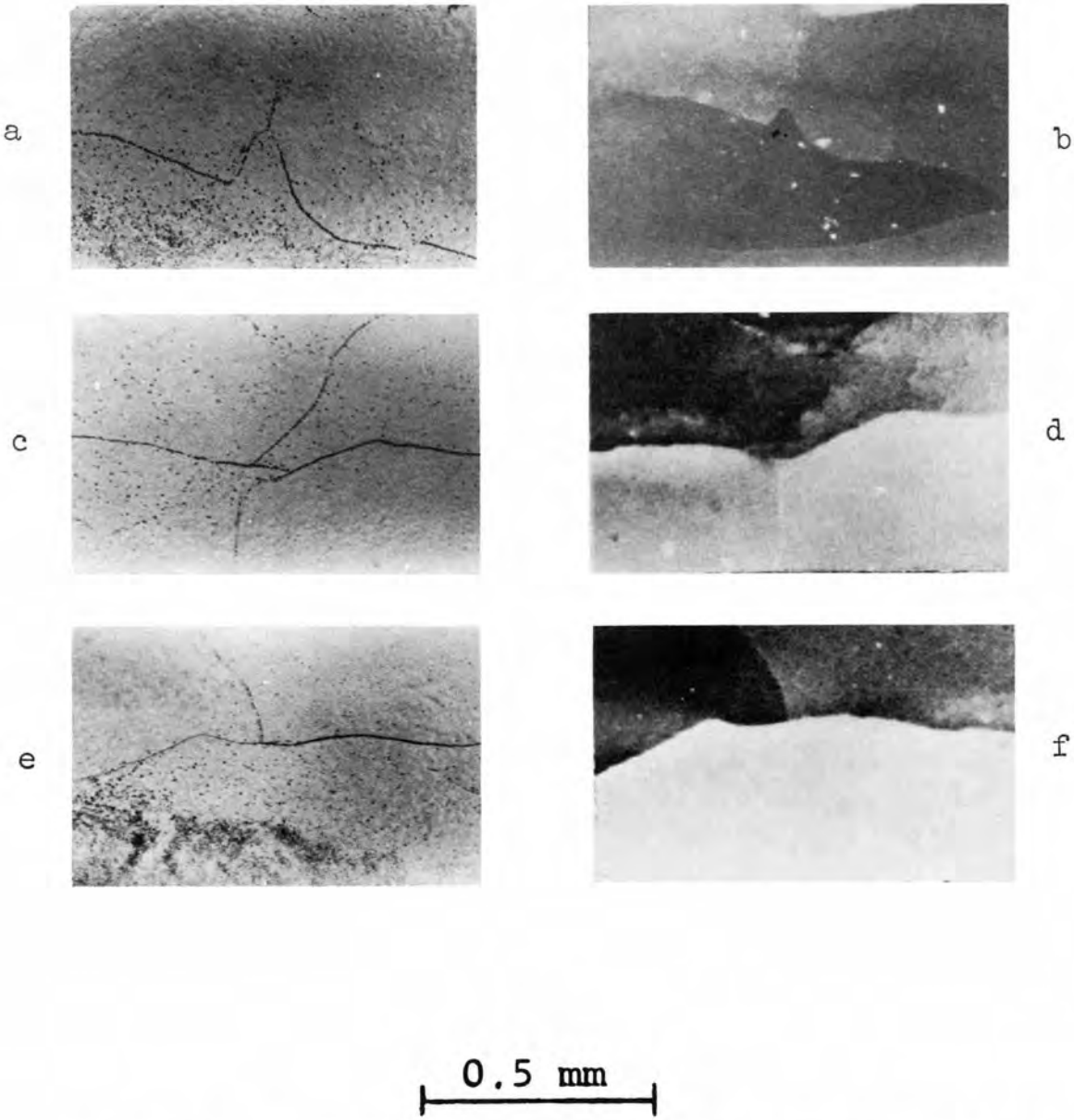

Fig. 6.30. Comparison of Etch-Pit Patterns and Berg-Barrett X-Ray Topograph. Photograph b is at a reduced magnification.

[redacted]

[redacted]

roughly 1.3×10^{-3} cm was sufficient to remove all traces of this disturbed layer.

A sample prepared as above was alternatively polished and etched, and the dislocation density within the subgrains was determined by the etch-pit count between treatments. Results are shown in Fig. 6.31. It is apparent that the density was quite low and that no significant variation existed to a depth of approximately 0.8mm below the as-cut surface. Thus one may conclude that the spark erosion process as used here does not observably alter the dislocation density. Furthermore, the estimate of a low dislocation density is borne out by the fact that these crystals can be successfully used in producing anomalous x-ray transmission topographs.[50]

Further utilizing the etch-pit method, preliminary results have been obtained in the measurement of average dislocation velocity versus resolved shear stress. The crystals are gown such that the maximum revolved shear stress acts on a {110} <111> slip system. The specimen configuration and orientation is shown in Fig. 6.32. The pits developed on the upper surface will thus be associated with edge dislocations. A source of dislocations was introduced by scribing a mark on the (112) surface using a 0.5 mil

---

[50]R. E. Reed, H. D. Guberman, and T. O. Baldwin, this report.

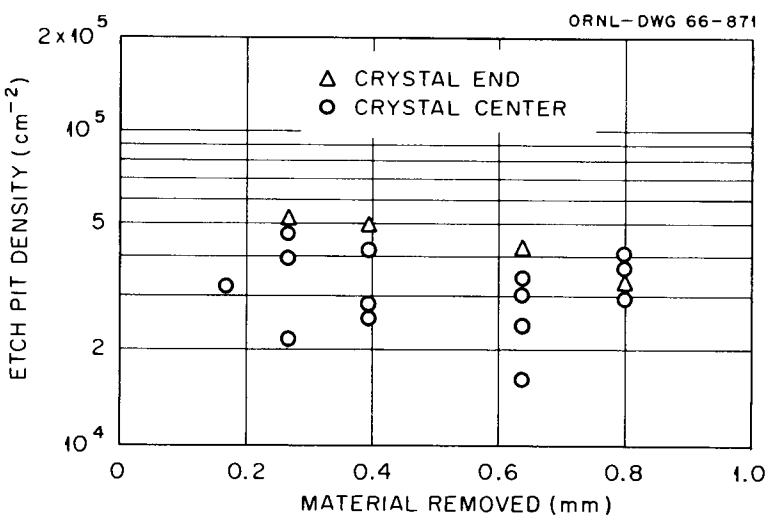

Fig. 6.31. Dislocation Density vs Depth in Spark Eroded Niobium Single Crystal.

[redacted]

ORNL-DWG 66-902

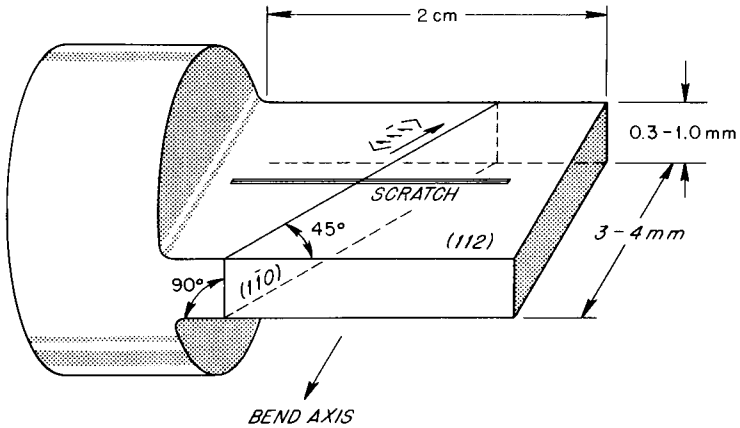

Fig. 6.32. Bend Specimen for Dislocation Velocity Studies.

diamond phonograph needle under a 1.5 gram load. The sample was stressed in a four point bending jig with the scribed surface under tension. After an appropriate period of stress application the sample is etched in the manner described earlier. Fresh dislocations propagated into the matrix were photographed, the distance moved measured from the photograph and the average velocity calculated therefrom.

Figure 6.33 represents the first results of such measurements for single-pass electron-beam purified single crystals. The samples were scribed and stressed at room temperature without having been first annealed. Comparisons were made to a sample which had been annealed at 2000°C for twelve hours and to one which had been scribed at liquid nitrogen temperature. There was found to be no measurable difference in the velocity or appearance of the dislocations in samples so treated. These effects are reasonable in as much as the dislocation density is quite low in the as-received condition to begin with. Furthermore, unlike iron, the impurities in niobium which might pin fresh dislocations do not have appreciable mobility at room temperature[51] and thus it is not necessary to introduce

[51] R. W. Powers and Margaret V. Doyle, "Diffusion of Interstitial Solutes in the Group V Transition Metals," J. Appl. Phys. 30, 514 (1959).

[redacted]

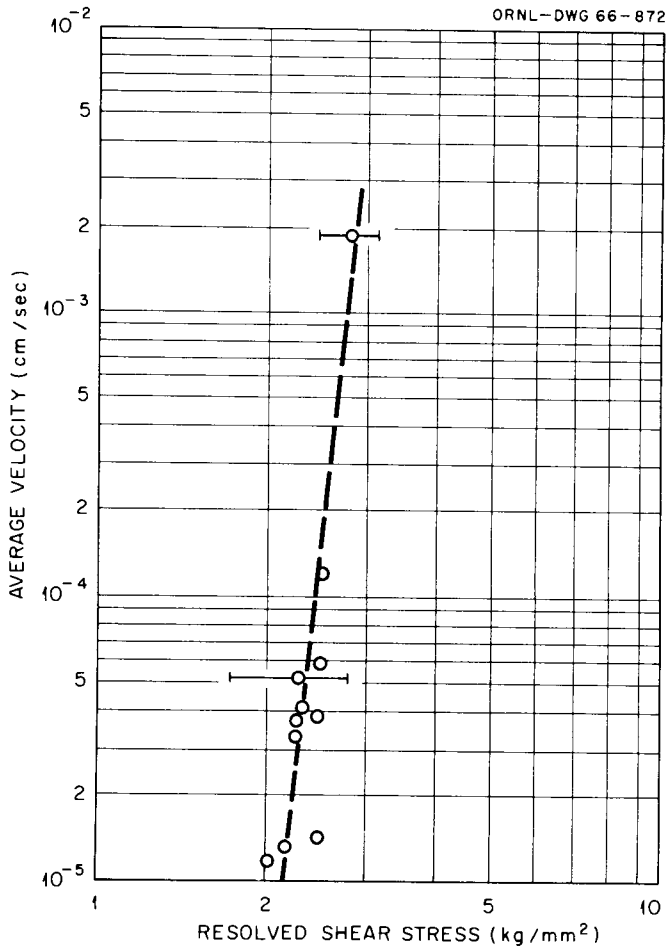

Fig. 6.33. Average Velocity vs Resolved Shear Stress Measured at Room Temperature in Single Crystal Niobium.

dislocations at lower temperatures.

The data evince considerable scatter which in the main is due to the inability to maintain a uniform geometry. The polishing and etching procedures have strong tendencies to thin the sample preferentially at the edges and after prolonged treatment to introduce other nonuniformities in the cross section which contribute to the inaccuracies of the stress measurement. In general, techniques must be improved to generate more reliable data. In particular, the efficiency of fresh, mobile dislocation production must be increased because at present it is possible to generate dislocations over only a few percent of the potential source length. As these techniques are improved and mastered the study will be broadened to observe the effects of radiation, temperature and purity.

[redacted]

Slip Line Observations on Irradiated Niobium Single Crystals

R. P. Tucker* R. E. Reed
M. S. Wechsler

Single crystals from Wah Chang Corporation starting stock were grown by a single pass, vertical zone, electron-beam treatment. The chemical analysis and discussion of crystal purity have been given previously.[52] Tensile samples were prepared from the zoned rod by centerless grinding a 0.75-in. long gage section with a 0.065-in. diameter. Twenty mils were removed from the gage diameter by chemical polishing such that all evidence of cold-work was absent from Laue back-reflection patterns. Sample irradiation was carried out in the Position Five Facility in the Bulk Shielding Reactor as previously described.[52,53] Wrapped in 20 mil thick cadmium foil, the samples were irradiated to a dose of 3.9×10^{17} neutrons/cm^2 ($E > 1$ Mev) at 135 ± 5°C.

The tensile axis was oriented for maximum resolved shear stress on the $(\bar{1}01)[111]$ slip system, the primary slip system. The slip geometry, illustrated in Fig. 6.34, is such that during deformation the initial circular cross section becomes elliptical. The direction, $\vec{A}$ (Fig. 6.34), of the major axis of the ellipse is $[\bar{1}2\bar{1}]$; it lies in the slip plane and is perpendicular to the slip direction. Furthermore, pure edge primary slip dislocation lines lie in this direction. The direction along the minor axis of the ellipse is designated direction $\vec{B}$ (Fig. 6.34); it is mutually perpendicular to $\vec{A}$ and the axis of the sample.

---

*Oak Ridge Graduate Fellow from the University of Tennessee under appointment from Oak Ridge Associated Universities.

[52]R. E. Reed and M. S. Wechsler, "Plastic Deformation in Niobium Single Crystals," Radiation Metallurgy Section Solid State Division Progr. Rept. Aug., 1965, ORNL-3878, p. 36.

[53]J. M. Williams, W. E. Brundage, B. C. Kelley, and M S. Wechsler, "The Position Five Facility in the Bulk Shielding Reactor," Radiation Metallurgy Section Solid State Division Progr. Rept. Aug., 1965, ORNL-3878, p. 68.

[redacted]

ORNL-DWG 65-7614R

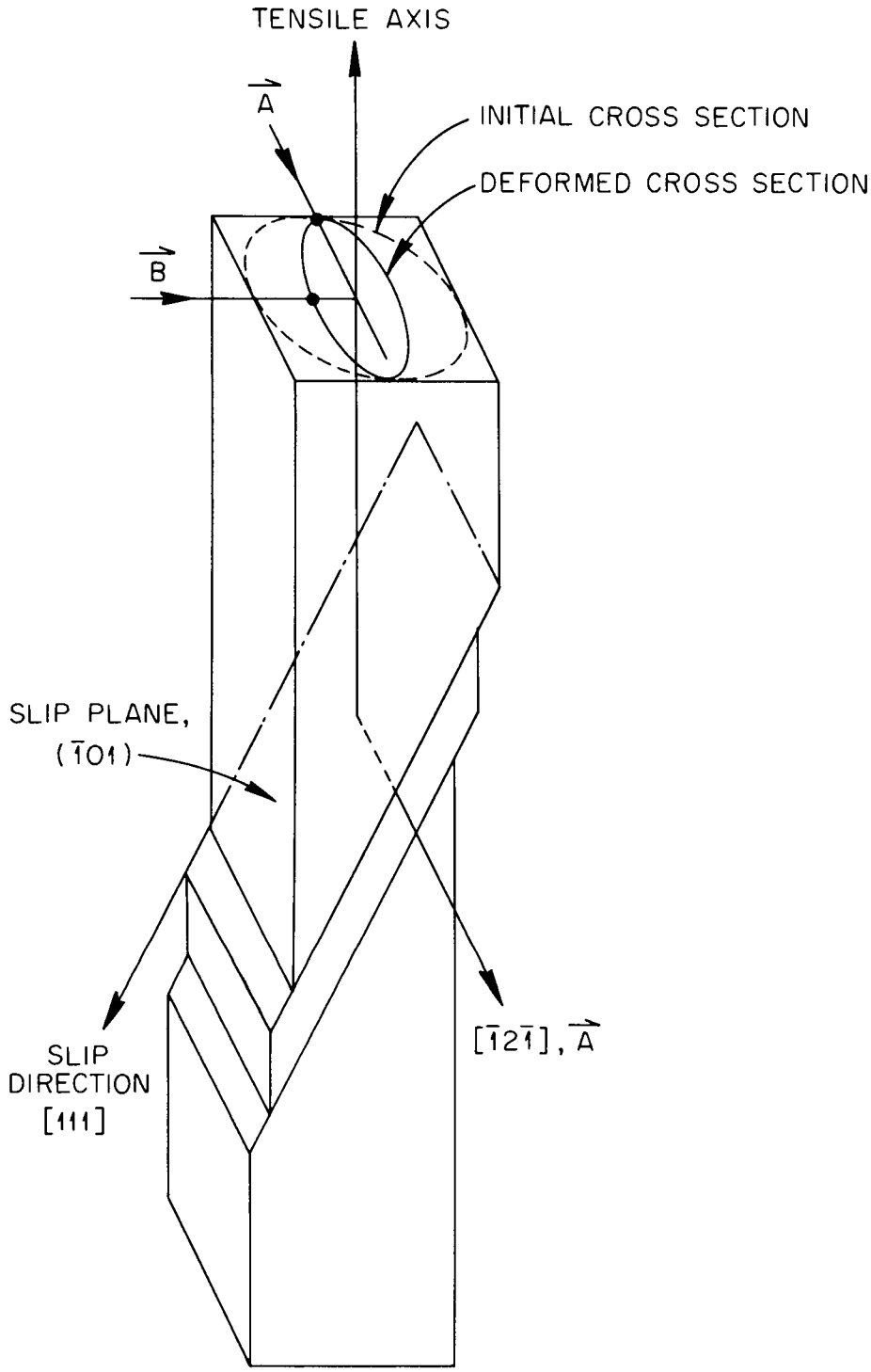

Fig. 6.34. Slip Geometry for Single Crystal Niobium Tensile Samples.

[redacted]

Extension of unirradiated samples resulted initially in the appearance of homogeneous wavy slip on portions of the surface near the $\vec{B}$ direction; long, straight slip lines in the [111] direction on portions of the surface near the $\vec{A}$ direction; and rotation of the tensile axis toward the [111] direction. For extensions in excess of 40 percent, slip on the secondary (101) [$\bar{1}$11] slip system is evidenced by the appearance of a second group of straight slip lines intersecting those formed earlier and by the deviation of the tensile-axis rotation from the path toward the [111] direction as detected by the Laue technique.[52]

Slip line observations have been made on an irradiated sample following a 10 percent extension. The neutron irradiation caused a marked change from the homogeneous deformation observed in the unirradiated samples. A significant amount of the deformation is confined to coarse bands of primary slip more or less uniformly distributed along the gage length. Figure 6.35 shows the bands characteristic of irradiated crystals as viewed in all orientations from $\vec{A}$ to $\vec{B}$. The confining of primary slip to coarsely spaced bands suggests that irradiated niobium exhibits channeling as observed by Mastel, et al.[54] in molybdenum. The bands would then be the result of deformation channeled into slip planes swept clean of radiation debris.

Near the $\vec{A}$ direction one observes an axial line with faint substructure on its right. The importance of these two features on the deformation has not been fully evaluated. Borrmann anomalous x-ray transmission studies on this material indicate the presence of low angle boundaries.[55] It is assumed that the slight orientation effects of the observed line and substructure contribute little to the deformation behavior of the crystal. On following the bands in Fig. 6.35 around the surface of the sample from $\vec{A}$ to $\vec{B}$, one notices thin slip lines branching off the primary bands as direction $\vec{B}$ is approached. Another locally more severely deformed region near

---

[54]B. Mastel, H. E. Kissinger, J. J. Laidler, and T. K. Bierlein, "Dislocation Channeling in Neutron-Irradiated Molybdenum," J. Appl. Phys. 34, 3637 (1963).

[55]R. E. Reed, H. D. Guberman, and T. O. Baldwin, this report.

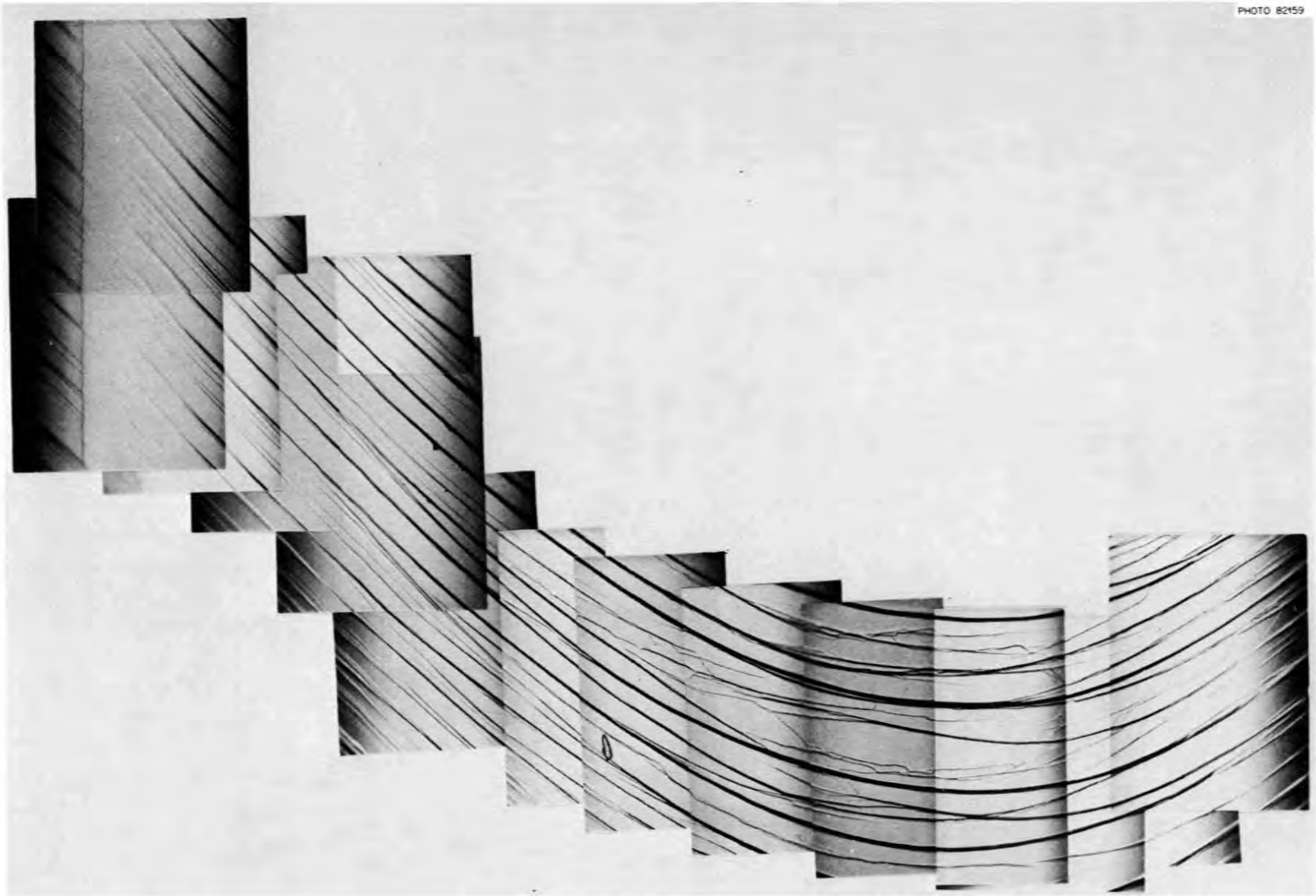

Fig. 6.35. Montage Showing Slip Lines in Irradiated Single Crystal Niobium After 10% Extension. Sample viewed in all orientations from direction $\vec{A}$ to direction $\vec{B}$.

[redacted]

B, shown in Fig. 6.36, contains an appreciable amount of slip between the coarse bands. Calculations were made of the angles which favorably oriented {110}, {112}, and {123} cross slip planes (planes containing the primary slip direction, [111]) made with the horizontal (the $[\bar{1}2\bar{1}]$ direction, $\vec{A}$) in Fig. 6.36. Table 6.7 gives the Schmid factors for these slip systems and the initial angles which the traces of the slip planes, viewed along $\vec{B}$, made with the horizontal direction, $\vec{A}$. Each angle for the straight slip line segments in Fig. 6.36 was found to agree approximately with one of those given in Table 6.7. For 10% extension of the irradiated sample there is no evidence in the microstructure of slip on the secondary (101) $[\bar{1}11]$ system but only slip in the [111] direction on cross slip planes. The inhomogeneous slip in the irradiated sample aids in the characterization of the wavy slip near direction $\vec{B}$ of the unirradiated crystals.

Table 6.7. Schmid Factors for Primary and Cross Slip Systems and Angles Which Slip Traces on Surface Perpendicular to $\vec{B}$ Make with Direction $\vec{A}$.

Slip System	Schmid Factor	Angle (degrees)
$(\bar{1}01)[111]$, primary	0.500	0
$(\bar{1}10)[111]$	0.250	67.8
$(0\bar{1}1)[111]$	0.250	112.2
$(\bar{2}11)[111]$	0.433	39.2
$(\bar{1}\bar{1}2)[111]$	0.433	140.8
$(2\bar{3}1)[111]$	0.094	82.3
$(1\bar{3}2)[111]$	0.094	97.7
$(\bar{3}21)[111]$	0.378	50.8
$(\bar{1}\bar{2}3)[111]$	0.378	129.2
$(\bar{3}12)[111]$	0.472	26.1
$(\bar{2}\bar{1}3)[111]$	0.472	153.9

[redacted]

Fig. 6.36. Slip Lines in Irradiated Single Crystal Niobium After 10% Extension.

[redacted]

Dislocation Dynamics in Niobium Single Crystals by Stress Relaxation Techniques

R. P. Tucker* S. M. Ohr
M. S. Wechsler

A program directed toward understanding the role of dislocation dynamics on the deformation behavior of niobium single crystals is under way. Two techniques - etch pitting and stress relaxation - are presently being used. Stress relaxation studies[56] on Ferrovac-E iron and Fe-3.2 wt % Si samples have suggested changes in the analysis of the stress dependence of dislocation velocity. The niobium study seeks to help evaluate the generality of the proposed analysis.

Since Johnston and Gilman[57] measured the velocity of dislocations in LiF and found the velocity to be stress dependent, numerous studies have been conducted to characterize this dependence in various crystals. The work of Stein and Low[58] on silicon-iron indicated that the dislocation velocity was dependent on the 35th power of stress according to Eq.(4) where σ_o is the stress corresponding to unit velocity.

$$v = \left(\frac{\sigma}{\sigma_o} \right)^m \tag{4}$$

Noble and Hull[59] described a stress relaxation technique which permits the evaluation of m, the index of the stress dependence of the velocity.

---

*Oak Ridge Graduate Fellow from the University of Tennessee under appointment from Oak Ridge Associated Universities.

[56]S. M. Ohr, "A Study of Radiation Hardening in Iron by Stress Relaxation Techniques," Radiation Metallurgy Section Solid State Division Progr. Rept. Aug., 1965, ORNL-3878, p. 16.

[57]W. G. Johnston and J. J. Gilman, "Dislocation Velocity, Dislocation Densities, and Plastic Flow in LiF Crystals," J. Appl. Phys. 30, 129 (1959).

[58]D. F. Stein and J. R. Low, Jr., "Mobility of Edge Dislocations in Silicon-Iron Crystals," J. Appl. Phys. 31, 362 (1960).

[59]F. W. Noble and D. Hull, "Stress Dependence of Dislocation Velocity from Stress Relaxation Experiments," Acta Met. 12, 1089 (1964).

[redacted]

The stress relaxation technique consists of pulling a tensile sample to a desired amount of strain, halting the crosshead at the required strain, and recording continously the decay of applied stress with time. After the interruption of the crosshead motion the sample continues to plastically deform as the dislocations gradually come to rest. With the crosshead stopped the total strain rate $\dot{\epsilon}$ which is the sum of the elastic, $\dot{\epsilon}_e$, and plastic, $\dot{\epsilon}_p$, contributions is zero.

$$\dot{\epsilon} = 0 = \dot{\epsilon}_e + \dot{\epsilon}_p$$

Thus during the relaxation the elastic and plastic strain rates are equal. From Hooke's law and dislocation theory the strain rates may be expressed as

$$0 = \dot{\epsilon}_e + \dot{\epsilon}_p = \frac{1}{E}\frac{d\sigma}{dt} + 0.5b\rho v \qquad (5)$$

where E is the combined elastic modulus of the machine and sample, 0.5 is an orientation factor for tensile strain, b is the Burgers vector, and ρ is the mobile dislocation density. Based on the stress relaxation data for iron, it was proposed that the velocity of the dislocations may be expressed as

$$v = \mu(\sigma - \sigma_t)^m \qquad (6)$$

where μ is the dislocation mobility (i.e. velocity under unit effective stress) and σ_t, the threshold stress, is the asymptotic value of stress approached during the relaxation. Combining Eqs. (5) and (6) one obtains the following relationship between the plastic strain rate and the relaxation rate, $d\sigma/dt$

$$\dot{\epsilon}_p/0.5b = \rho v = -\frac{1}{0.5bE}(d\sigma/dt) = \rho\mu\,(\sigma - \sigma_t)^m \qquad (7)$$

Based on equation (7) a log-log plot of ρv versus $(\sigma - \sigma_t)$ should yield a straight line with slope m and intercept $\rho\mu$. It was found that in iron and silicon-iron treatment of the data according to equation (7) resulted in separation into two straight lines with slopes of

$$m_1 = 7.0 \pm 0.6$$

$$m_2 = 2.5 \pm 0.3$$

which were independent of material and irradiation treatment. However, σ_t, the treshold stress is material sensitive and was found to be the quantity most strongly affected by irradiation.

Single crystal niobium tensile samples were prepared from single pass, electron-beam, vertical zoned rods by centerless grinding a 0.75 in. long gage section with a 0.065 in. diameter. Twenty mils were chemically polished from the gage diameter such that Laue back-reflection x-ray patterns showed no evidence of cold work in the sample. Samples wrapped in 20-mil thick cadmium foil were irradiated to a dose of 3.9×10^{17} neutrons/cm^2 (E > 1 Mev) at 135 ± 5°C in the Position Five Facility in the Bulk Shielding Reactor.[60,61] Sample extension was at a strain rate of 1.75×10^{-4} sec^{-1} on a table model Instron machine using split grips.

Stress relaxation tests have been carried out on unirradiated niobium single crystals initially oriented favorably for slip on the $(\bar{1}01)[111]$ system after extensions of 10, 20, 30, and 40 percent. The various pre-relaxation strains were obtained by repeated extension of a single sample. The sample exhibited an upper yield point which did not return in the time between extensions for the sample held at room temperature. In each test the stress relaxation was followed until the load closely

---

[60]R. E. Reed and M. S. Wechsler, "Plastic Deformation in Niobium Single Crystals," Quarterly Progress Report: Irradiation Effects on Reactor Structural Materials, May, June, July, BNWL-128, Aug., 1965, p. 10.35.

[61]J. M. Williams, W. E. Brundage, B. C. Kelley, and M. S. Wechsler, "The Position Five Facility in the Bulk Shielding Reactor," Quarterly Progress Report: Irradiation Effects on Reactor Structural Materials, May, June, July, 1965, BNWL-128, Aug., 1965, p. 10.68.

approached its asympotic value. Preliminary results from these tests are (1) total stress relaxation decreases from 2.3 to 1.9 kg/mm^2 as the extension increases from 10 to 40 percent and (2) for pre-relaxation extensions of 10, 20, 30, and 40 percent, the threshold stresses, σ_t, are 3.27, 4.55, 5.59, and 6.41 kg/m^2 respectively. Stress relaxation has been followed after 10 percent extension in an irradiated sample and was found to be about 2.8 kg/mm^2. The load-time curve for the irradiated sample showed load fluctuations caused in part by lack of temperature control during the test. The fluctuations prevented an accurate determination of the threshold stress; however, the value 4.35 kg/mm^2 was used in the further analysis.

The data for the 10 percent extensions in both unirradiated and irradiated samples were analyzed according to equation (7). It was found that, as in the case of iron, the relaxation in niobium can be separated into two contributions. The tentative values of m_1 were about 5 and 7 in unirradiated and irradiated samples; whereas, the values of m_2 were approximately 2 and 1.5, respectively. The variation in m values is attributable in part to uncertainty in the values of threshold stress and suggest the need of additional experimental work in which the temperature during relaxation is more carefully controlled before the niobium data can be used to critically evaluate the analysis.

Objections to the empirical relationships for stress dependence of velocity given in equations (4) and (6) are that the power dependence is much greater than for other physical quantities obeying power laws and the relations do not predict a limiting dislocation velocity as the stress is increased to high values. To meet the latter of these objections Gilman[63] suggested the following form for the stress dependence

---

[63]J. J. Gilman, "The Plastic Resistance of Crystals," Australian J. Phys., vol. 13, p. 327, 1960.

[redacted]

$$v = v_o \, e^{-D/\tau} \tag{8}$$

where v_o is a limiting velocity near the velocity of sound, D is a drag stress, and τ is the appropriate shear component of stress.

From a stress relaxation test one can obtain the quantity ρv and, if it is assumed that ρ is constant during the relaxation, use can be made of equation (8) to analyze the data. The validity of the constant ρ assumption is questionable. The data for the unirradiated and irradiated niobium crystals have been plotted according to equation (8) and for early relaxation times the data are in excellent agreement with the predicted linear relationship as shown in Fig. 6.37. For long relaxation time the unirradiated sample data deviate from the linear relationship. This deviation may be associated with lack of constancy of dislocation density. Additional tests are required before a choice can be made between the above and other possible methods of analysis.

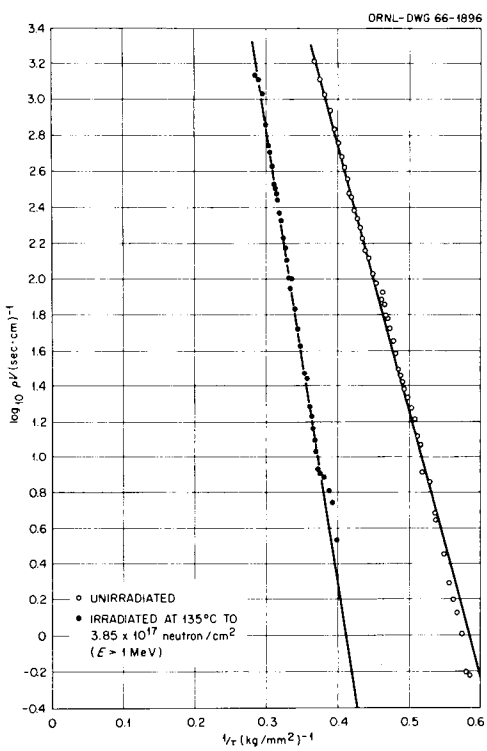

Fig. 6.37. Variation of Dislocation Velocity with Reciprocal of Applied Stress in Single Crystal Niobium after 10% Extension.

[redacted]

[redacted]

Thermal-Neutron Irradiation of Hastelloy-N Tensile Samples

H. E. McCoy* B. C. Kelley
J. R. Weir* M. S. Wechsler

The grain-boundary radiation-embrittlement of austenitic stainless steels[64,65,66] and nickel-base alloys[67] under high temperature and low strain rate conditions is thought to be due largely to the production of helium. The principal source of the helium at low doses is from the thermal neutron reaction $^{10}B(n,\alpha)^{7}Li$, although at high doses the helium arising from fast neutron ractions may also play a part.

In order to separate the thermal-neutron fast-neutron effects in the nickel-base alloy Hastelloy-N, an irradiation is now under way in the Thermal Neutron Irradiation Facility in the BSR. The facility consists of a D_2O-tank adjacent to the reactor core, penetrated by vertical tubes into which experiment capsules may be placed. In the tube being used for this experiment, the thermal neutron flux was measured using bare gold foils with the reactor at 0.5 kw and the cadmium ratio was determined using cadmium-covered gold foils at a power level of 5 kw. The results indicate a maximum thermal flux of about 2×10^{12} neutrons/cm^2 sec at the power level of 1 mw used for the materials irradiation and a cadmium ratio of several hundred.

---

*Metals and Ceramics Division, Oak Ridge National Laboratory.

[64]W. R. Martin, J. R. Weir, and R. E. McDonald, "Irradiation Embrittlement of Low-Boron Type 304 Stainless Steel," Nature, vol. 208, pp. 73-4, 1965.

[65]W. R. Martin and J. R Weir, "Influence of Grain Size on the Irradiation Embrittlement of Stainless Steel at Elevated Temperatures," to be published in J. Nuclear Materials.

[66]W. R. Martin and J. R.Weir, "The Effect of Postirradiation Heat Treatment on the Elevated Temperature Embrittlement of Irradiated Stainless Steel," Nature, vol. 202, p. 997, 1964.

[67]W. R. Martin and J. R. Weir, "Effect of Elevated Temperature Irradiation on the Strength and Ductility of the Nickel-Base Alloy, Hastelloy-N," ORNL-TM-1005, Feb. 1965.

[redacted]

[redacted]

The experiment capsule contains 136 round tensile samples of various grain sizes containing two concentration levels of boron. Also included are cobalt, nickel, and neptunium flux monitors. Thermocouples attached to the samples indicate irradiation temperatures close to 50°C. A total of 200 hours of exposure is planned. At this time, the irradiation is somewhat over half completed.

[redacted]

[redacted]

Previous reports in this series are:

ORNL-TM-920	Period Ending June 30, 1964
ORNL-TM-960	Period Ending September 30, 1964
ORNL-TM-1000	Period Ending December 31, 1964
ORNL-TM-1100	Period Ending March 31, 1965
ORNL-TM-1200	Period Ending June 30, 1965
ORNL-TM-1270	Period Ending September 30, 1965
ORNL-TM-1400	Period Ending December 31, 1965

[redacted]

[redacted]

Internal Distribution

1–3. Central Research Library
4–5. ORNL – Y-12 Technical Library
Document Reference Section
6–15. Laboratory Records
16. Laboratory Records, RC
17. ORNL Patent Office
18. G. M. Adamson, Jr.
19. J. C. Banter
20. J. H. Barrett
21. S. E. Beall
22. R. J. Beaver
23. M. Bender
24. R. G. Berggren
25. J. O. Betterton, Jr.
26. D. S. Billington
27. A. L. Boch
28. B. S. Borie
29. G. E. Boyd
30. W. H. Bridges
31. R. B. Briggs
32. W. E. Brundage
33. R. M. Carroll
34. J. V. Cathcart
35. G. W. Clark
36. K. V. Cook
37. J. H. Crawford
38. J. E. Cunningham
39. J. H. DeVan
40. C. V. Dodd
41. D. A. Douglas, Jr.
42. J. I. Federer
43. B. E. Foster
44. A. P. Fraas
45. J. H Frye, Jr.
46. R. J. Gray
47. W. R. Grimes
48. H. D. Guberman
49. J. P. Hammond
50. W. O. Harms
51. R. L. Heestand
52–53. M. R. Hill
54. N. E. Hinkle
55. D. O. Hobson
56. H. W. Hoffman
57. H. Inouye
58. T. N. Jones
59. G. W. Keilholtz
60. B. C. Kelley
61. J. A. Lane
62. C. F. Leitten, Jr.
63. A. P. Litman
64. A. L. Lotts
65. R. N. Lyon
66. H. G. MacPherson
67. R. E. MacPherson
68. M. M. Martin
69. W. R. Martin
70. D. I. Matkin
71. R. W. McClung
72. H. E. McCoy, Jr.
73. H. C. McCurdy
74. R. E. McDonald
75. D. L. McElroy
76. C. J. McHargue
77. F. R. McQuilkin
78. A. J. Miller
79. E. C. Miller
80. J. G. Morgan
81. F. H. Neill
82. S. M. Ohr
83. M. F. Osborne
84. P. Patriarca
85. F. H. Patterson
86. A. M. Perry
87. S. Peterson
88. M. L. Picklesimer
89. R. E. Reed
90. P. L. Rittenhouse
91. W. C. Robinson
92. M. W. Rosenthal
93. G. Samuels
94. A. W. Savolainen
95. J. L. Scott
96. O. Sisman
97. G. M. Slaughter
98. G. P. Smith, Jr.
99. N. K. Smith
100. S. D. Snyder
101. I. Spiewak
102. J. T. Stanley
103. W. J. Stelzman
104. J. O. Stiegler
105. D. B. Trauger
106. R. P. Tucker

[redacted]

[redacted]

107. J. T. Venard
108. G. M. Watson
109. M. S. Wechsler
110. A. M. Weinberg
111. J. R. Weir, Jr.
112. W. J. Werner
113. G. D. Whitman
114. J. M. Williams
115. R. O. Williams
116. J. C. Wilson
117. H. L. Yakel, Jr.
118. F. W. Young, Jr.
119. C. S. Yust

External Distribution

120–122. F. W. Albaugh, Battelle, PNL
123. R. J. Allio, Westinghouse Atomic Power Division
124. R. D. Baker, Los Alamos Scientific Laboratory
125. L. Brewer, University of California, Berkeley
126. V. P. Calkins, GE, NMPO
127. W. Cashin, Knolls Atomic Power Laboratory
128. S. Christopher, Combustion Engineering, Inc.
129–130. D. F. Cope, AEC, Oak Ridge Operations
131. G. K. Dicker, Division of Reactor Development, AEC, Washington
132. E. A. Evans, GE, Vallecitos
133. W. C. Francis, Phillips Petroleum Company
134. R. G. Grove, Mound Laboratory
135. D. H. Gurinsky, BNL
136. A. N. Holden, GE, APED
137–139. J. S. Kane, University of California, Livermore
140. J. H. Kittel, ANL
141. E. J. Kreih, Westinghouse, Bettis Atomic Power Laboratory
142. W. L. Larsen, Iowa State University, Ames Laboratory
143. J. J. Lombardo, NASA, Lewis Research Center
144. J. H. MacMillan, Babcock and Wilcox Company
145. R. E. Pahler, Division of Reactor Development, AEC, Washington
146. S. Paprocki, BMI
147. D. Ragone, GA
148. Division of Research and Development, AEC, ORO
149. H. Kato, U.S. Department of the Interior, Bureau of Mines
150. R. Van Tyne, Illinois Institute of Technology Research Institute
151. F. C. Schwenk, Division of Reactor Development, AEC, Washington
152–153. J. M. Simmons, Division of Reactor Development, AEC, Washington
154. L. E. Steele, Naval Research Laboratory
155. R. H. Steele, Division of Reactor Development, AEC, Washington
156. W. F. Sheely, Division of Research, AEC, Washington
157. A. Strasser, United Nuclear Corporation
158. W. R. Voigt, Division of Reactor Development, AEC, Washington

[redacted]

159. C. E. Weber, Atomics International
160. G. W. Wensch, Division of Reactor Development, AEC, Washington
161. M. J. Whitman, Division of Reactor Development, AEC, Washington
162–176. Division of Technical Information Extension